NUMERICAL STUDY OF SEA ICE DYNAMICS AND WAVE-ICE INTERACTIONS IN THE MARGINAL ICE ZONE

by

Jean-Pierre Auclair

Submitted in partial fulfillment of the requirements
for the degree of Doctor of Philosophy

at

Dalhousie University
Halifax, Nova Scotia
April 2021

To all who inspired, supported and motivated me along the way,
and in memory of two pillars of Canadian science among them
Louis Fortier and Neil Gall

TABLE OF CONTENTS

LIST OF FIGURES

ABSTRACT

The Marginal Ice Zone (MIZ) is a highly dynamic region between the open ocean and the inner ice pack. The ice over this region is subjected to waves, introducing new forces but also changing the ice from a cohesive material to a mobile collection of floes. Until recently, the challenges posed by in-situ ice measurements in the MIZ prevented a detailed characterization of changes in the ice cover. The rapidly changing conditions over short distances have also prevented detailed numerical simulations. Recent developments in observational and computational capabilities allow further investigations of the physical processes for ice formation and wave-ice interactions in the MIZ. Many features of the MIZ remain to be explained and quantified, particularly rapid ice movement near the ice edge and ice thickening under wave pressure. In order to investigate these and support future field and numerical studies, a model of the MIZ is developed with a new numerical method better suited for high resolution. Simulations of waves causing ice compaction and the ice edge jet are then performed to detail the expected impacts of waves on sea ice. The potential of numerical improvements in sea ice models to obtain greater efficiency and accuracy at high resolutions is successfully demonstrated. The addition of the wave radiative stress allows the generation of realistic thickness profiles, provided that the sea ice strength is modified to represent the difference between pack ice and thinner ice. With the same modifications, obliquely incident waves on the ice edge produced an ice edge jet with a range of characteristics depending on wave parameters and modeled interactions. The magnitude of wave attenuation in sea ice and the ice strength are found to be very important factors in the simulations. Consideration of wave effects on ice thickness and drift speed are also shown to have potential to increase both open water and ice formation.

LIST OF ABBREVIATIONS AND SYMBOLS USED

Abbreviations	Description
AJNK	Analytical Jacobian - Newton-Krylov method
CAA	Canadian Arctic Archipelago
CFL	Courant–Friedrichs–Lewy condition
EVP	Elastic-Viscous-Plastic ice
FGMRES	Flexible Generalized Minimal Residual method
GSL	Gulf of Saint-Lawrence
LIM	Louvain-La-Neuve sea Ice Model
MIZ	Marginal Ice Zone
SOR	Successive Over-Relaxation
VP	Viscous-Plastic ice
aEVP	adaptive Elastic-Viscous-Plastic ice

Roman symbol	Description	Units
A	Ice concentration	
$\mathbf{A}(\mathbf{u})$	Picard matrix of the ice momentum equations	$\mathrm{N\,s/m^3}$
C_{da}	Atmospheric drag coefficient	
C_{dw}	Oceanic drag coefficient	
$E(f,\theta)$	Wave energy spectrum	$\mathrm{m^2/Hz}$
$\mathbf{F}(\mathbf{u})$	Vector of momentum equation functions for all velocities	$\mathrm{N/m^2}$
H_d	Sea surface height	m
$\mathbf{J}(\mathbf{u})$	Jacobian matrix of $\mathbf{F}(\mathbf{u})$	$\mathrm{N\,s/m^3}$
$N(f,\theta)$	Wave action spectrum	$\mathrm{m^2}$
P	Ice pressure	$\mathrm{N/m}$
P_p	Ice compressive strength	$\mathrm{N/m}$
P_{Hibler}	Ice compressive strength defined in *Hibler III* (1979)	$\mathrm{N/m}$
P_{Hybrid}	Hybrid ice compressive strength	$\mathrm{N/m}$
P^*	Ice strength coefficient	$\mathrm{N/m^2}$
S	Wave source terms	$\mathrm{m^2/Hz^2}$
c_g	Wave group velocity	$\mathrm{m/s}$
d	Water depth	m
e	Ellipticity of the sea ice yield curve	
f	Wave frequency	Hz
f_C	Coriolis parameter	$\mathrm{rad/s}$
g	Acceleration due to gravity	$\mathrm{m^2/s}$
h	Ice thickness	m
k	Waveumber	$\mathrm{m^{-1}}$
$\mathbf{k}$	Vertical unit vector	
t	Time	s
u	One-dimensional ice velocity	$\mathrm{m/s}$
u_a	One-dimensional wind velocity	$\mathrm{m/s}$
$\mathbf{u}$	Vector of all sea ice velocities	$\mathrm{m/s}$
$\mathbf{u}_{2D}$	Two-dimensional ice velocity	$\mathrm{m/s}$

Greek symbol	Description	Units
Δ	Ice deformation term	s^{-1}
$\alpha(f)$	Wave attenuation coefficient per unit distance	m^{-1}
$\beta(f)$	Wave attenuation coefficient per unit time	s^{-1}
γ	Ice strength factor	m^{-1}
γ_{nl}	Convergence criterion for Newton's method	
ζ	Bulk ice viscosity	$\mathrm{N\,s/m}$
η	Shear ice viscosity	$\mathrm{N\,s/m}$
θ	Wave propagation angle	degrees
ρ	Ice density	$\mathrm{kg/m^3}$
ρ_a	Air density	$\mathrm{kg/m^3}$
ρ_w	Water density	$\mathrm{kg/m^3}$
σ	One-dimensional ice stress term	N
$\boldsymbol{\sigma}$	Internal ice stress term	N
τ_a	One-dimensional atmospheric drag on ice	$\mathrm{N/m^2}$
$\boldsymbol{\tau}_a$	Atmospheric drag on ice	$\mathrm{N/m^2}$
$\boldsymbol{\tau}_b$	Basal stress on ice	$\mathrm{N/m^2}$
τ_r	Ramp-up time scale	hours
τ_s	Sinusoid time scale	days
τ_w	One-dimensional water drag on ice	$\mathrm{N/m^2}$
$\boldsymbol{\tau}_w$	Water drag on ice	$\mathrm{N/m^2}$
τ_{wv}	One-dimensional wave stress on ice	$\mathrm{N/m^2}$
$\boldsymbol{\tau}_{wv}$	Wave stress on ice	$\mathrm{N/m^2}$
$\tilde{\tau}_{wv}(f)$	Wave stress per unit frequency	$\mathrm{N/m^2Hz}$
ω	Wave angular frequency	$\mathrm{rad/s}$

ACKNOWLEDGEMENTS

This PhD is an edifice built through the collaboration of many. First among them is my research supervisor, Hal Ritchie, who accepted my request to embark on this project from out of the blue, connected me with too many people to name and supported me through the many opportunities and challenges that arose. I could not have hoped for a better enabler to foster my growth from student to scientist, or a better proof-reader to catch what my tired eyes would not see anymore. Beyond showing me what I have come to consider an ideal science career, you have also showed me what it can mean to be a great scientist, mentor and person altogether. The other great influence of my degree is my academic supervisor, Jinyu Sheng, who has been unfailing through all of my graduate studies in his drive for excellence, high aspirations and relentless pursuit of science. No person I know can get people to deliver their full potential more than Jinyu, through high standards and direct feedback but, above all, the example he sets by himself of motivation and productivity.

Along with my supervisors, the main pillars of my PhD, stand my committee members, past and present, the buttresses that kept me and my project standing. Their inquisitive minds, thoughtful feedback and capacity to keep my interests in mind when even I was not able to were instrumental to achieving completion. Special thanks go to my two current members, who both joined at critical moments. Years ago, at a time when everything was shaking, the providential addition of Dany Dumont to my committee literally turned this project around. Through the years, his passion for the MIZ extended to everyone involved and guided the future. Great enthusiasm for research, outreach and the community all at once and a special kind of uniting leadership made this collaboration a pleasure that I hope to keep going for years to come. Last only in timing, Dan Kelley was the clincher that finally brought about the completion of my degree by bringing a clarity that only one with his experience could have. Although his time on the committee was short, it was critical and highlighted his considerate, perspicacious and altogether wise nature.

A PhD is far too large a project to be the product of only a few people. The many friends and family members who shared with me the many joys, distractions, doubts and pains that inevitably are part of the process played an essential role in enabling me to reach the end. I am too weary of forgetting someone to list names but, if I ranted to you at some point in the last 8 years, if we cheered to a milestone, or even if we just did something else entirely so I could think of something else for a while, you contributed more than you probably know. Thank you!

Finally, I would like to thank the Marine Environmental Observation Prediction and Response Network (MEOPAR), Natural Sciences and Engineering Research Council of Canada (NSERC), the Ocean Frontier Institute (OFI) and Environment and Climate Change Canada (ECCC) for their financial support.

CHAPTER 1

INTRODUCTION

Sea ice plays an important role in the marine biological (*Post et al.*, 2013; *Arrigo et al.*, 2008) and physical (*Francis and Vavrus*, 2012) environment at high latitudes. Evidence of the significant effects of decreasing sea ice on temperature and weather is also mounting (*Screen and Simmonds*, 2010; *Seierstad and Bader*, 2009). Environmental conditions, particularly sea ice cover, are rapidly changing in the Arctic (*Meier et al.*, 2007). Combined with the development of activities dependent on open waters such as shipping, mining and oil extraction in the Arctic Ocean, this heightens the need for a better understanding of sea ice and improved, higher resolution forecasting.

Several numerical models have been developed to study and forecast sea ice. The two most widely used models are the Community Ice CodE (CICE) maintained at the Los Alamos National Lab (*Hunke et al.*, 2015) and the Louvain-la-Neuve sea Ice Model (LIM) developed at the Université catholique de Louvain (*Vancoppenolle et al.*, 2009). To simulate sea ice, the momentum, mass conservation and thermodynamic equations are solved sequentially, each evolving the sea ice to conserve energy, mass and heat individually rather than achieving a coherent balance (*Notz et al.*, 2016). Dynamics concentrate on drift and deformation, while thermodynamics govern freeze-up and melt, both impacting the conservation of sea ice. Sea ice models are commonly coupled with the ocean and atmosphere models where sea ice acts as a mediator for air-sea heat and momentum exchanges by determining the open water fraction and the magnitude of the fluxes going through (*Hibler III and Bryan*, 1987; *Dupont et al.*, 2015). These models provide the basis for the sea ice forecast. To facilitate their integration in global modeling systems, most sea ice models are built on an Eularian framework, tracking the time evolution of sea ice properties on a grid. This keeps their structure similar to the ocean and atmosphere models with which they are coupled. Because of the focus on seasonal variations and climate, sea ice models are also built for large spatial scales and long time scales. However, sea ice is a moving material with a history of small-scale, anisotropic structures and thus would lend itself well conceptually to Lagrangian models (*Rampal et al.*, 2016).

Sea ice models routinely use observations, particularly ice concentration from satellites, as guides (*Smith et al.*, 2013). Observations can also be particularly useful for the performance assessment of ice models (*Kwok et al.*, 2008). Greater ice edge movements than predicted by ice models with winds and current forcing have been observed West of Greenland and around Antarctica. These are regions where surface gravity waves are expected to be providing a significant part of the forcing, competing with winds and surface ocean currents. Waves can also be responsible for preventing the northward drift of Antarctic sea ice (*Stopa et al.*, 2018). Waves have long been considered as absent from ice covered waters, at least for the purpose of modeling. However, they can be a major factor in dynamics, making ice more mobile by breaking it and supplying kinetic energy near the ice edge (*Squire*, 2020). How to represent the impact of waves on ice, rather than the other way around, is an ongoing research question that has received renewed interest recently, not only for its relevance in high-resolution modeling but also its implication on the climate.

Studying wave-ice interactions requires accessing the Marginal Ice Zone (MIZ), the region where waves propagate from open waters into sea ice. It is a dangerous environment, limiting our ability for direct observations. The scarcity of observations and the complexity of the interactions between waves, ice and currents have prevented the MIZ dynamics from being well understood. Multiple possible descriptions of the MIZ or processes within this region have been suggested. In-situ observations are most often only along a single transect perpendicular to the ice edge and thus the physics of the MIZ also tends to be defined in this one-dimensional space. Many theories exist for wave attenuation by sea ice (e.g. *Wadhams* (1973); *Liu et al.* (1991); *Kohout and Meylan* (2008); *Sutherland et al.* (2019)). Wave energy gradients such as those created by attenuation have been linked to a force applied on the ice through the wave radiation stress defined by *Longuet-Higgins*

(1977) and tested by *Sutherland and Dumont* (2018). However, wave attenuation and the wave radiation stress have yet to be combined into a dynamical system able to reproduce the evolution of conditions in the MIZ. In order to achieve this combination and evaluate the effects of these processes and their interactions in the MIZ, a high-resolution, fast and simple wave-ice numerical model of the MIZ, defined in the one-dimensional space typical of MIZ studies, would be an ideal tool. Such a model would require both sea ice and wave dynamics and two-way wave-ice interactions in the form of wave attenuation and radiation stress on ice, all supported by efficient and accurate numerics. Obtaining this type of model is the goal of this thesis. It would not only enable comparisons with existing observations but could also help guide future observation campaigns by providing predictions to be tested. Thanks to its simplicity, such a model would also be an ideal test bed for model development before scaling up to operational sea ice models.

The development of this one-dimensional model of the MIZ is motivated by and building on a collection of scientific works presented in the literature review performed in section 1.1, covering ocean-ice-atmosphere interactions (1.1.1), wave-ice interactions specifically (1.1.2), sea ice dynamics (1.1.3) and the mathematical framework used to model sea ice (1.1.4). The objectives of this thesis and their corresponding chapters are then detailed in section 1.2, each corresponding to milestones for the model and related scientific questions.

1.1 Literature review

1.1.1 Ocean-Ice-Atmosphere Interactions

Sea ice interacts with both the ocean and atmosphere. Indeed, the main motivation to study, model and forecast sea ice is its effect on the atmosphere, for both weather and climate. Beyond that, sea ice itself also has a major impact on water use, particularly for navigation. A sufficient understanding of sea ice and its interactions is necessary to predict its own evolution as well as its effects as a mediator and intermediate for fluxes between the ocean and atmosphere at high latitudes.

Ocean-Ice-Atmosphere interactions can be considered over two different scales. On the large scale (tens to hundreds of kilometers or more), wind and water drag are the major source and sink of momentum for the ice, respectively (*Bouchat and Tremblay*, 2014). Over time, the ocean and atmosphere also drive the melting and freezing of sea ice by providing and removing heat. Over shorter temporal and spatial scales and near the edge of the ice pack, in the MIZ, a different regime takes place where waves dominate, providing more momentum than the winds or currents and also changing the mechanical properties of the ice by inducing breakup. In open waters, the formation of frazil and its accumulation into consolidated ice is also governed by winds, waves and currents. Sea ice dynamics over the MIZ are much more difficult to describe or quantify than the wide-ranging, slow processes, however. Although the MIZ represents a relatively small fraction of total ice-covered area, the integrated effect of processes changing ice distributions or characteristics can in turn impact the ocean-ice-atmosphere interactions, a role likely to become even more important in the context of temperature increases at high latitudes and diminishing ice area and thickness.

The presence of sea ice mediates the sensible and latent heat fluxes as well as humidity fluxes between the atmosphere and ocean. The determining factor is the area of open water since direct air-sea fluxes are much greater than fluxes through the ice, the magnitude of which are determined by the characteristics of the ice such as thickness and snow cover (*Maykut*, 1986). In the winter time, when the atmosphere and ice surface are generally colder than the ocean, air flowing over open waters removes heat and moisture which can lead to ice creation as well as an increase in cloud cover and downwind precipitation in a situation similar to lake effect snow (*Pellerin et al.*, 2004). The atmosphere can respond very rapidly to the ice opening up and enabling these air-sea fluxes, making the inclusion of dynamic sea ice noticeably beneficial to winter weather forecasts, as shown by *Pellerin et al.* (2004).

Changes in the sea ice coverage can be broadly categorized in three different forms: leads, polynyas and offshore ice edge movement. The dynamic forcing responsible for these can vary. Leads are cracks in the ice, often occurring in response to internal forces applied at large scales (*Girard et al.*, 2009). Polynyas, larger areas of open waters, develop because of the interaction of external forcing with topography (*Morales Maqueda et al.*, 2004). Finally, offshore ice edge movements stem from a balance of dynamical forcing and ice resistance (*Liu et al.*, 1993). In all of these cases, ice formation in open waters acts to limit the open water extent (*Lebedev*, 1968). This equilibrium between ice advection and formation has been succinctly described by *Pease* (1987) and applied to the Saint Lawrence polynya in the Bering Sea. Besides the magnitude of the driving external forcing and the air temperature, the depth over which frazil accumulates once formed has proven to be an important factor (*Biggs et al.*, 2000; *Biggs and Willmott*, 2004). However, frazil has been observed in the water column over a range of depths greater than ice thickness (*Drucker et al.*, 2003) and the characterization of the dependence of this depth range as a function of waves and currents is a challenge (*Walkington et al.*, 2007).

Small changes in ice cover can induce large changes in temperature in the atmospheric boundary layer. *Lüpkes et al.* (2008) used two one-dimensional models, a nonhydrostatic atmospheric model and a heat diffusion snow and ice model to investigate the importance of sea ice. Within this setup, an ice cover decrease from 100% to 99% could cause a change in the temperature $10\mathrm{m}$ above the mean sea level of up to $3.5\ \mathrm{K}$ and a decrease to 95% coverage could increase temperature by up to $18\ \mathrm{K}$ in the most extreme conditions (winter, clear sky at night) for moderate wind speeds ($4\ \mathrm{m/s}$), as shown in Fig. 1.1(b). Wind speeds control the mixing of the temperature signals by defining boundary layer properties but a significant ice concentration driven temperature difference is observed in all cases, acting mostly through warming up the snow surface temperature and decreasing the strongly negative, or downwards, heat flux in the ice (Fig. 1.1(c-d)).

Beyond the local impact on weather, on larger spatial and temporal scales, the recent decrease in sea ice cover has been linked to a destabilization of the northern polar atmospheric circulation, leading to colder Pacific and North American winters, the so called polar jets bringing particularly cold air to the lower latitudes (*Jaiser et al.*, 2013; *Kim et al.*, 2014). *Liu et al.* (2012) also showed a link between the decrease of sea ice cover, increased air-sea interactions and increased winter precipitation in the mid-latitudes. *Hibler III* (1979) also highlighted that, on larger scales, the creation, movement and subsequent melt of ice cause another form of heat transport. Ice freezing and melting are a source and sink of latent heat for the ocean and atmosphere. Differences in local freezing and melting, which are supported by ice transport, imply heat transport in the opposite direction: from the melting

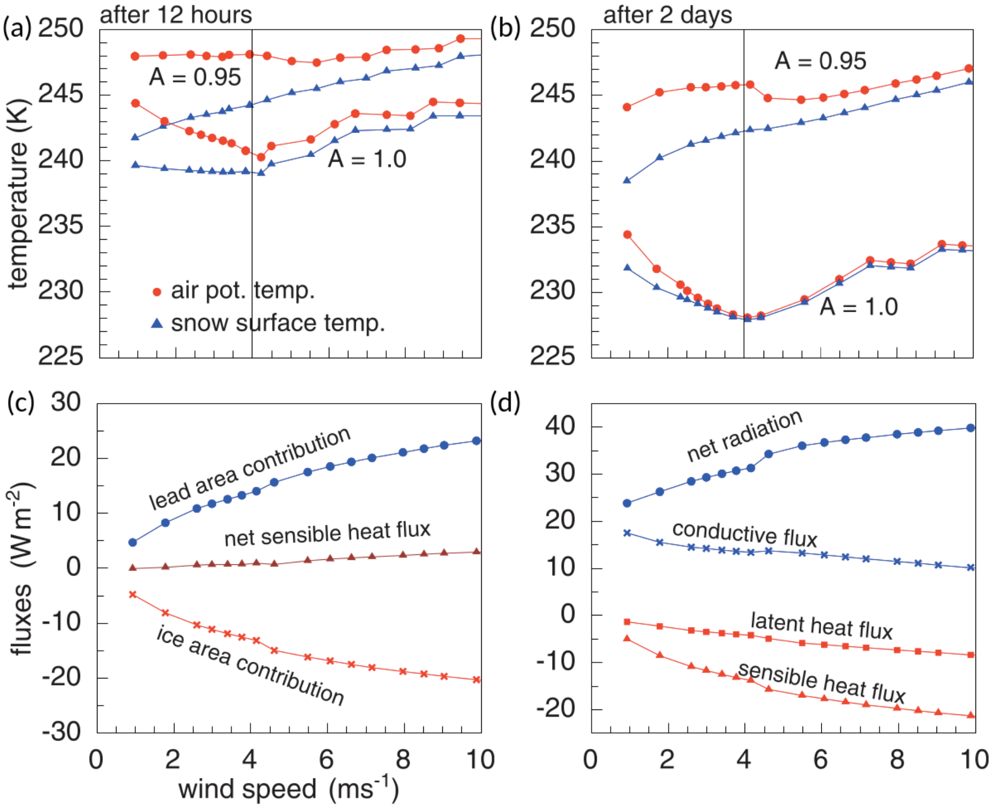

Figure 1.1: Air temperature at 10 m above the mean sea level and snow surface temperatures over ice after 12 hours (a) and 2 days (b). (c) Components of the atmospheric heat flux over 95% ice covered waters with ocean and ice contributions. (d) Heat fluxes at the ice/snow boundary. Downwards fluxes are negative. (Reproduced from *Lüpkes et al.* (2008))

area to the freezing area. This may be more intuitively thought of as a “cold transport” by forming ice on the North Slope and moving it to the main outflow region in the Greenland Sea in the Arctic or, within the Gulf of St. Lawrence, along the north shore all the way to Cabot Strait. Better simulation of changes in ice concentration, formation and volume, would improve our ability to represent this transport. On top of this heat transfer, sea ice also affects surface water density through brine rejection upon freezing and the release of freshwater when melting. These two phenomena combined play a role in water mass formation and evolution (*Saucier et al.*, 2003). Brine trapped in the ice also influences its heat capacity and through that changes the timing for spring melting (*Zhang et al.*, 2004).

Sea ice also changes the momentum transfer between the atmosphere and ocean. In the general case, ice provides a different interface for momentum transfer, changing drag coefficients and the velocity differences. Sea ice is a cohesive material and it tends to concentrate gradients in wind stresses around linear kinematic features (LKFs). This creates more localized areas of stronger shear. This concentration of deformations was observed by *McPhee et al.* (2005) using RADARSAT feature tracking to obtain velocity fields and deformations. Through this amplification of shear, sea ice can induce Ekman pumping locally in the upper ocean, bringing warmer, saltier waters from greater depths towards the surface, as was observed locally using CTDs by *McPhee et al.* (2005) and modeled by *Häkkinen* (1986). Since LKFs also create open waters, they expose this warmer water to the atmosphere and create particularly strong local air-sea fluxes.

The interactions between the oceans and the atmosphere described above are central to our weather and climate. In higher latitudes, the mediating role of sea ice implies that small changes in ice cover or characteristics can lead to large changes in conditions. Between open waters and compacted pack ice, the MIZ is the area where sea ice varies the most. This variability is bound to increase with decreasing total ice cover and thinning ice, further amplifying the need to take it into account in our descriptions of the Earth system. For this, a framework to test our physical understanding of the MIZ is necessary. Such an understanding would allow the integration of the MIZ and its impacts in the weather and climate systems.

1.1.2 Wave-Ice Interactions

Surface gravity waves and sea ice are both important to forecast for humanity's surface-focused use of water. Both forecasts can be obtained fairly accurately at low resolution independently of one another, with waves using forcing data sets from coupled atmosphere-ice-ocean models (e.g. *Bernier et al.* (2016); *Dupont et al.* (2015)). Efforts to forecast waves and ice coupled together have been limited. Indeed, current operational sea ice models do not use parameterizations for wave effects. Nevertheless, the interactions of waves and sea ice have been studied for decades (*Squire*, 2020). Originally, process studies of the MIZ focused on the first order processes at play (e.g. *Røed and O'Brien* (1983); *Johannessen et al.* (1983); *McPhee et al.* (1987)), usually in the atmosphere-ocean-ice system, considering waves to be a secondary effect of the wind. However, the shift towards regional high resolution modeling along with warming temperatures meaning smaller ice area, thinner ice and larger waves have made wave-ice interactions a topic of great interest recently. In order to model the MIZ, two distinct challenges must be addressed. First, the modeling the MIZ combines the existing complexities inherent to modeling waves and ice individually, but it also requires a representation for the interactions themselves for which there is a wide choice of parameterizations. This is particularly problematic since most descriptions are derived from empirical or theoretical relationships dependant on specific conditions. Secondly, the area in which waves and ice interact tends to be small compared to the resolution of many modeling systems, a band near the ice edge up to tens of kilometers wide at most, requiring either substantial computational resources or custom made solutions. With the rise of regional models of increasing resolutions and the desire to produce more precise forecasts, however, coupled models are now being developed (*Budgell*, 2005; *Williams et al.*, 2013b, 2017b). Different approaches are being pursued, with varying degrees of complexity and efficiency depending on whether the focus is on research or operations.

Significant efforts in the ocean modeling community are currently concentrated towards introducing and balancing forcing terms to obtain an equilibrium which reproduces observed spatial variation of variables such as wave energy, ice thickness and floe size along a transect in ice. Because they are easier to observe, the two main interactions studied in the MIZ in the past have been the attenuation of waves by sea ice and the breaking of ice into smaller floes by waves (*Squire*, 1993; *Langhorne et al.*, 1998; *Dumont et al.*, 2011; *Williams et al.*, 2013a). However, the floe size is rarely a variable in ice models which instead focus on ice concentration and thickness. In comparison, wave energy is much more prevalent, being the main variable needed to forecast the significant wave height and it is thus at the core of wave models. In wave modeling (*Tolman*, 2009), wave energy is defined as a spectrum ($E(f,\theta)$) dependent on frequency (f) and direction (θ) and transformed to the wave action spectrum ($N(f,\theta) = E(f,\theta)/\omega$), where $\omega = 2\pi f$ is the angular frequency, as wave action is conserved in the presence of currents. Although wave energy should be defined in Joules, or $\mathrm{J}/(\mathrm{Hz}\cdot\mathrm{rad})$ for the spectral version, it is often converted to m^2 and m^2/Hz by normalizing by the water density (ρ_w, kg/m^3) and the acceleration due to gravity (g, m/s^2), to allow easy conversion to and from wave height (H_s, m) through $E = H_s/16$ (*Bouws et al.*, 1998). This quantity is advected and affected by a series of source terms representing wind input (S_{in}), wave dissipation in open waters

(S_{ds}), wave attenuation by ice (S_{ice}), non-linear wave interactions (S_{nl}) and other processes (collectively, S, m):

$$\frac{\partial N}{\partial t} + \nabla_x \cdot \dot{x} N + \frac{\partial}{\partial k} \dot{k} N + \frac{\partial}{\partial \theta} \dot{\theta} N = \frac{S}{\omega}. \tag{1.1}$$

where $\dot{x}$, used for spatial advection, is the combination of the group velocity ($c_g = \frac{\partial \omega}{\partial k}$) and current velocity while spectral advection is done through the $\dot{k}$ and $\dot{\theta}$ terms. Generally, for simulations of waves in open water, the angular frequency ($\omega = 2\pi f$) is linked to the wavenumber (k, m^{-1}) by the following wave dispersion relation:

$$\omega^2 = gk \tanh(kd) \tag{1.2}$$

as a function of gravity (g) and water depth (d). When waves enter sea ice, the consideration of additional phenomena requires different versions of the dispersion relation, changing depending on ice properties. More importantly, wave energy gets attenuated by sea ice and decreases exponentially with distance. *Robin* (1963) reported the attenuation of waves by the bending of ice floes of more than half a wavelength and little loss of wave energy when floes were less than one sixth of the wavelength. Through the wave dispersion relation (Eq. 1.2), the preferential attenuation of small wavelengths can also be associated with high frequencies. This frequency dependence causes a narrowing of the energy spectrum in ice and, indeed, waves in ice have been observed in “groups” governed by the constructive and destructive interference of the longer frequencies (*Thomson et al.*, 2019). The frequency dependence can also be seen as a decrease in penetration distance of the energy with increasing frequency or an attenuation coefficient per unit distance ($\alpha(f)$, m^{-1}) that increases with frequency. Under uniform conditions and neglecting currents, the wave energy spectrum of a plane wave in ice can thus be described by:

$$E(f, x, \theta) = E(f, 0, \theta) e^{-\alpha(f) x / \cos(\theta)} \tag{1.3}$$

where x is the distance from the ice edge and θ, the direction of the wave, is defined such that $\theta = 0$ corresponds to the direction perpendicular to the ice edge. A complete directional spectrum can be reconstructed by adding multiple directions back together. More generally, the wave attenuation coefficient (α) also depends on ice characteristics such as thickness and floe size (*Boutin et al.*, 2018).

Because of the variety of conditions in the ice, multiple theories have been developed to explain wave attenuation, each with a different physical basis. A combination of processes, such as basal friction in thin ice and floe flexion in thicker ice, is most likely to best explain the attenuation (*Perrie and Hu*, 1996; *Ardhuin et al.*, 2018; *Sutherland and Rabault*, 2016). However, most of the attenuation theories concentrate on a single process. Building on the observations of *Robin* (1963), *Wadhams* (1973) proposed a steady state creep mechanism for the attenuation of swell by sea ice. At shorter wavelengths, *Wadhams et al.* (1988) explained the decrease in energy as waves scattering off the edge of ice floes. Inspired by observations of large waves far into the ice pack by the *R/V Polarstern*, *Liu and Mollo-Christensen* (1988) developed a comprehensive description of the most important processes in wave-ice interactions. This was then further developed by *Liu et al.* (1991) as a conceptual model for wave propagation under ice flexion and pack compression. *Kohout and Meylan* (2008) simulated the scattering of waves at both edges of individual ice floes over a transect using a phase resolving wave model multiple times in order to obtain averaged scattering attenuation coefficients. Scattering can also be generalized to apply not only to edges but also to irregularities in the ice such as cracks and pressure ridges with varying amplitudes (*Bennetts and Squire*, 2012a,b). The attenuation of wave energy can be explained by a variety of other phenomena as well, from wave-induced floe collisions (*Herman*, 2018) to viscous ice and water motions (*Sutherland et al.*, 2019) and turbulence under the ice (*Voermans et al.*, 2019), as well as creep during flexion, break-up, overwash, non-linear scattering and potentially more.

Waves also impact sea ice. Wavelength can influence the floe size both during growth by limiting the size of pancake ice (*Shen et al.*, 2001) and by determining the typical scale of breaking in an established ice cover (*Langhorne et al.*, 1998). This can be used to predict the extent of wave-induced break-up from the ice edge inward as well as the floe size along the direction of propagation, as was presented by *Dumont et al.* (2011) using a one-dimensional wave propagation model where attenuation by sea ice is the only source (sink) of wave energy. In this model, three processes were considered in order: advection-attenuation of wave energy was first calculated, then the breaking of ice floes caused by flexural strain followed by a new calculation of wave attenuation coefficients by floe scattering. In a scheme similar to time stepping, these steps were repeated until an equilibrium solution is obtained. Looking at partially landfast ice with winds coming from the land, *Wadhams* (1983) proposed that waves applying a force on the ice, the wave radiation pressure described by *Longuet-Higgins and Stewart* (1964) and *Longuet-Higgins* (1977), were responsible for the organization of ice in bands. In such circumstances, waves can be a strong driver for divergence and the emergence of small scale patterns in the ice. Using the wave radiation stress theory, the decay of wave energy is linked to a transfer of momentum from the waves to the ice in the direction perpendicular to the direction of wave propagation as described in *Sutherland and Dumont* (2018) for the case of offshore waves being attenuated as they propagate in the MIZ. This force can be equivalent to wind stress over a distance of up to 50km (*Stopa et al.*, 2018) and can incite movements such as a jet along the ice edge (*Smith and Bird*, 1991) or eddies (*Dai et al.*, 2019).

Using observations of wave energy in the MIZ, *Sutherland and Dumont* (2018) balanced the calculated incoming wave radiation stress with a Mohr-Coulomb ice strength, as used by *Uzuner and Kennedy* (1976), along one dimension perpendicular to the ice edge while assuming a steady state. This balance enabled a prediction of sea ice thickness along a transect that compares well with observations, as shown in Fig. 1.2. Such a mechanism of wave induced thickening of the ice by rafting is further supported by observation of layering in pack ice cores from wave exposed regions, laboratory experiments and phase and floe resolving wave-ice model simulations (*Dai et al.*, 2004). The sharp ice thickness increase at the ice edge predicted and observed is different from what would be obtained using only winds and currents which apply spatially uniform stresses, as is done in typical ice models, although it is possible to reproduce something similar with modifications to the ice strength (*Leppäranta and Hibler III*, 1985).

Because of the inherently complex nature of waves and ice conditions over the MIZ and challenging observing conditions, simplifications of MIZ processes are commonplace. Ice forecast models ignore waves entirely and wave models can, by their nature, only consider the wave attenuation without any response or movement from the ice beyond updating forcing fields. Most proposed explanations for wave attenuation consider only a single source of attenuation or are based on empirical relationships from a relatively small

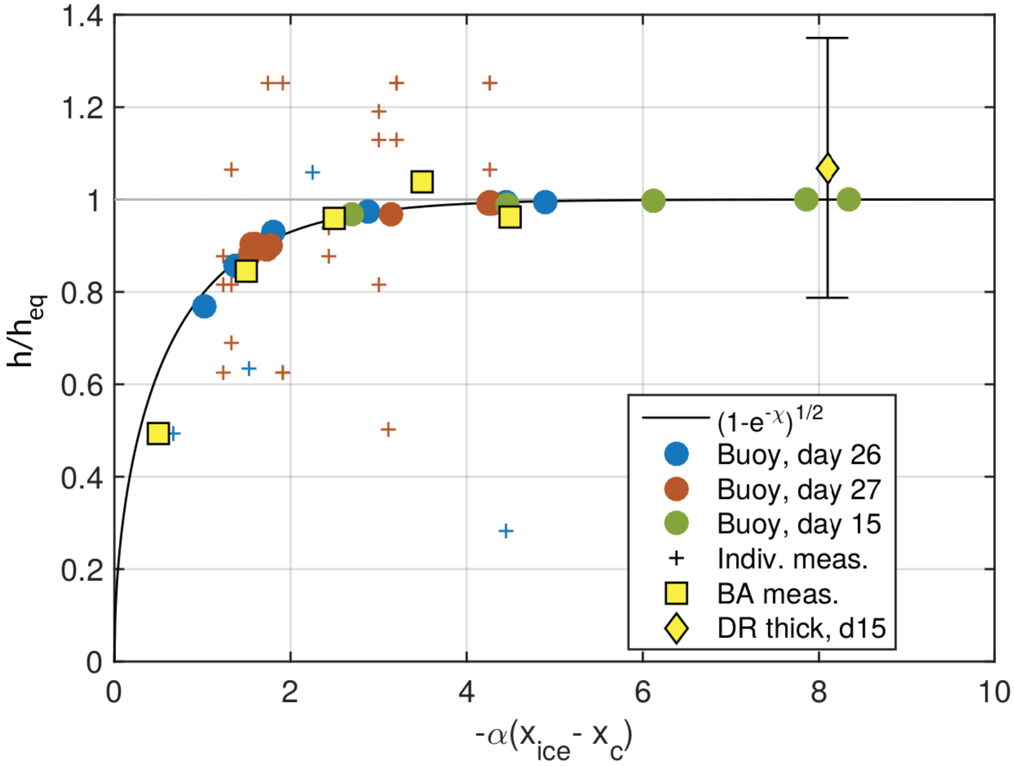

Figure 1.2: Ice thickness as a function of ice fetch. Ice thickness has been normalized by the equilibrium ice thickness and distance from the ice edge is normalized by the exponential decay scale. The black line shows the theoretical ice thickness profile for an exponential decay of wave energy in deep water (Eq. 1.3). The coloured circles are the thickness estimated using the Mohr-Coulomb stress model; the yellow squares are bin averages of those measurements. The yellow diamond is the ice thickness in BicWin 2016, estimated using the dispersion relation and the attached error bars indicate the potential error due to uncertainties in the water depth. (Reproduced with permission from *Sutherland and Dumont* (2018))

number of observations. Studies of wave-ice interactions often reduce the problem to the one dimension perpendicular to the the ice edge and, even along this one dimension, it is rare to consider the time-dependent evolution of both waves and ice, or either, instead of steady-state solutions. In this context, coupling wave and ice dynamics through wave attenuation and the wave radiation stress would bring a novel perspective in the study of MIZ dynamics.

1.1.3 Sea Ice Dynamics

On average, sea ice movement is dictated by a balance between sources and sinks of momentum mediated by the ice internal stresses. Locally, internal ice stresses and atmospheric forcing are responsible for most of the sea ice movement while the ocean acts mostly as a momentum sink, as shown in Fig. 1.3 (*Bouchat and Tremblay*, 2014). Sea ice movement is strongly dependent on wind forcing (*Perrie and Hu*, 1997) and, without obstacles, ice can move rapidly under strong winds (*Saucier et al.*, 2003). At the edge of the ice pack, where ice is exposed to the open ocean, waves can also be a major local source of momentum (*Perrie and Hu*, 1996). Areas of low sea ice concentrations are particularly responsive to changes in the forcing due to lower cohesion and the added force applied by locally generated wind waves. Diverging conditions can create this high mobility in packed ice by first lowering ice concentration and then allowing wave growth to happen within the ice (*Wadhams*, 1983). Upon encountering the shoreline, sea ice movement must stop. This resistance by the coast creates an area of convergence, causing the ice to thicken through ridging and rafting at the expense of the total ice area.

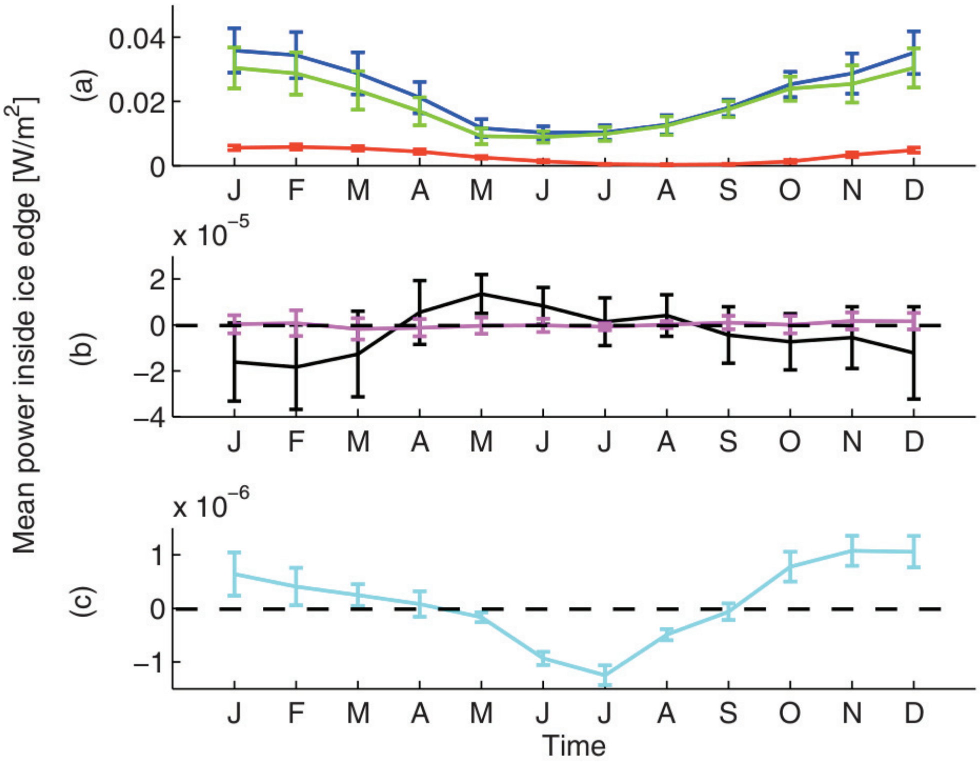

Figure 1.3: 25-years average and standard deviation of power contributions to the sea ice kinetic energy balance coming from (a) surface wind stress (blue), absolute value of water drag (green) and internal stress (red), (b) gravity (black), kinetic energy changes (magenta) and (c) change in inertia (cyan). (Reproduced from *Bouchat and Tremblay* (2014))

In the Arctic, dominant winds towards the northern side of Greenland and the Canadian Arctic Archipelago (CAA) push the ice until it thickens sufficiently and its internal strength can resist the pressure, leading to some of the thickest Arctic sea ice near the coast (*Kwok et al.*, 2008). This resistance deviates part of the incoming ice towards the Beaufort Sea, where the ice follows the Beaufort Gyre. The exact manner in which simulated ice does so is influenced by the choice of ice strength and drag parameterizations for both winds and currents (*Chikhar et al.*, 2019). The wind forcing and sea level gradients determine the fraction of the ice that goes through the CAA and Davis Strait (*Lu et al.*, 2014; *Dumont et al.*, 2009). On the other side of Greenland, Fram Strait is the main ice export channel for the Arctic. There, the width of the ice band flowing South often changes drastically under the influence of waves from the Greenland Sea (*Dumont et al.*, 2011). In the Gulf of St. Lawrence (GSL), ice is particularly present in two regions: the Strait of Belle-Isle, where it is a continuation of the ice propagating south along the coast of Labrador in the Winter (*Zhang et al.*, 2004), and in the shallower waters of the GSL near New Brunswick and Prince Edward Island (*Saucier et al.*, 2003; *Smith et al.*, 2013; *Urrego-Blanco and Sheng*, 2014). Ice also tends to accumulate on the south shore of the St. Lawrence Estuary (SLE) as it is pushed by north-westerly dominant winds and the associated waves.

Alongside the thermodynamics that dictate growth and melt, the movement of sea ice is a key driver in its yearly changes. During the development of one of the foundational first generation sea ice models, *Hibler III* (1979) observed an increase in production by $\sim$150% and a reduction in average thickness by 30% compared to static ice when enabling ice dynamics. On a multi-year time-scale, dynamics also set the stage for the coming years, as described by *Hutchings and Rigor* (2012). Greater ice displacement in the Arctic can increase the relative coverage of thin, new ice which is more likely to melt in the following summer, a relationship that can be used to inform seasonal ice forecasts (*Williams et al.*, 2016). The same process also acts more regionally, the advection of thin, first-year ice in the Beaufort sea from the Chukchi sea has lead to the creation of an anomalous polynia in 2006 and a record minimum sea ice extent in the Beaufort for 2007, for example (*Hutchings and Rigor*, 2012).

Much of our ability to observe the drift and concentration of sea ice comes from satellite imagery (ex.: RADARSAT) through feature tracking. It is also used as a means of ground-truthing models. By evaluating the correlation between time series of sea ice velocity fields between model simulation and satellite observations, *Girard et al.* (2009) concluded that modern sea ice models simulate sea ice drift reasonably well, although modelled velocities tend to be larger and more variable than observed. However, further analysis of the statistics of the velocity fields and deformations has shown noticeable disagreement between simulations and observations (*Lindsay et al.*, 2003; *Kwok et al.*, 2008). Model results tend to spread deformations, or velocity gradients, over large areas and deformations distributions have broader peaks compatible with large areas of more uniform deformations. Analysis of observations shows that a relatively small number of events account for the majority of the deformations and that larger deformations occur in summer, due to the lower ice strength (*Xie et al.*, 2017). Indeed, sea ice tends to fail in a very localized manner with the ice breaking along linear kinematic features (LKFs) such as leads in divergence and shear or ridges in compression. This should lead to sharp low deformation peaks and more frequent extremes in distributions. Even when compared at scales much larger than the grid size, modeled deformations distributions show much fewer extreme values than distributions obtained from the satellite data.

LKFs can become more localized and large deformations more frequent with increased accuracy of the velocity field, which itself depends on both model resolution and numerical scheme (*Lemieux and Tremblay*, 2009; *Lemieux et al.*, 2010; *Bouchat and Tremblay*, 2014). For example, performing more iterations of a solver to better approximate a solution to the momentum equation can improve the distribution (Fig. 1.4 b) and localization (1.4 c and d) of shear by sharpening velocity gradients (*Lemieux and Tremblay*, 2009; *Bouchat and Tremblay*, 2014). By comparing different numerical solvers, *Losch and Danilov* (2012) also showed that sea ice viscosities increase with solution accuracy, something beneficial as a significant shear strength is necessary in sea ice to obtain realistic movement near shore (*Kreyscher et al.*, 2000). Models otherwise develop anomalously high drift velocities along the shore, particularly for thick ice along coastlines, such as happens naturally north of Greenland and west of the Canadian Arctic Archipelago. The dynamics for sea ice could thus have a greater dependence on model accuracy than for other media. Differences in velocities and deformations may also be attributed to drag or ice strength parameterizations (*Chikhar et al.*, 2019). More fundamentally, *Girard et al.* (2009) showed that the distributions of deformations differ between model and observations over a range of scales, suggesting that the problem might be more deeply rooted, in the definition of the ice internal mechanics themselves.

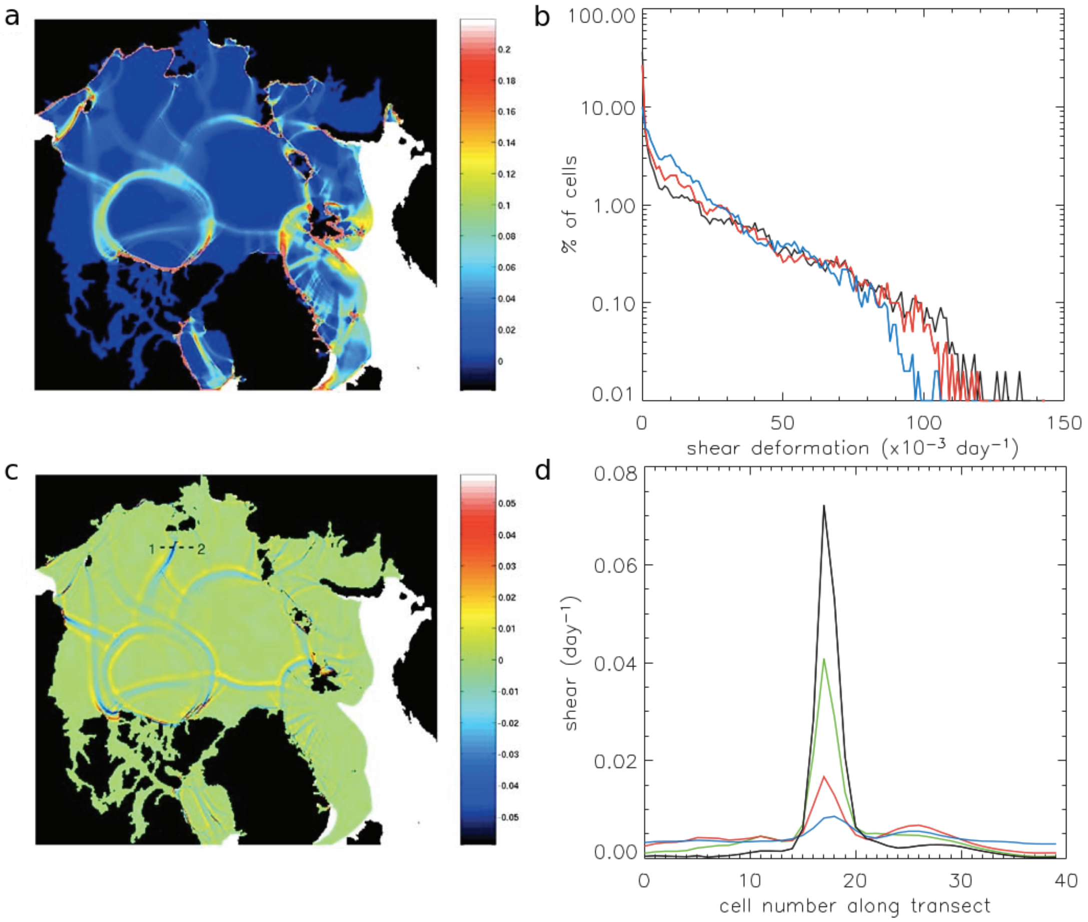

Figure 1.4: (a) Shear deformation field on 6 January 1997 0000 UT, (b) shear distribution (capped at 0.2 day^{-1} for clarity) in the central Arctic, (c) shear difference field for a partially converged linear solver (40 iterations) and (d) shear accross the LKF transect between 1 and 2 in (c) for 10 (blue), 40 (red), 100 (green) and 10500 (black) iterations of a linear momentum equation solver. (Reproduced with permission from (*Lemieux and Tremblay*, 2009))

The discrepancy between modeled and observed deformation distributions in turn leads to errors for many physical processes that can be of great relevance to ice forecasts and Earth system modeling. The strength of sea ice, or its ability to resist deformations, is directly related to thickness and concentration (*Flato and Hibler III*, 1995), the two fundamental variables for sea ice modeling, and to deformation rates. Ice deformations also lead to an increase in open water either by opening up the pack in divergence and shear or reducing ice area through convergence. The open waters thus created then accentuate the melt of sea ice in the summer by exposing the darker ocean beneath to solar radiation while favouring ice formation in winter by increasing heat fluxes out of the ocean. The additional formation of thin ice results in a highly skewed thickness distribution for dynamic ice. Lower ice concentrations can also facilitate the flushing of ice towards lower latitudes both in the Arctic and in the GSL by making it more fluid. Although it was proposed to introduce tension in order to model landfast ice (*König Beatty and Holland*, 2010), tension can have negative consequences such as diminishing flow by impeding divergence in the pack in the Fram Strait outflow where ice accelerates southward as it is melting (*Kreyscher et al.*, 2000). Instead, *Lemieux et al.* (2015) introduced a new parameterization for grounding. In numerical models, compression causes thickening of the ice locally as the averaged out consequence of ridging (*Rothrock*, 1975a,b) and a strong resistance in compression is needed in order to prevent excessive thickening (*Lipscomb et al.*, 2007). In reality however, ridges are very distinct and of particular importance for navigational purposes, identifying areas to be avoided even by ice breakers who will favour going through ice as weak as possible. Furthermore, internal ice pressure, which is calculated from deformations, is an increasingly sought after variable for ice forecasts since it will influence the ability of ships to push ice aside and navigate within the pack.

At the core of the issue of realistic sea ice modeling is the relationship between strains, or deformations, and stresses applied on sea ice, defined by its rheology, to adequately represent ice as a material in a modeling framework best suited to fluids. The viscous-plastic (VP) rheology (*Hibler III*, 1977, 1979, 1980) and particularly its elasto-viscous-plastic (EVP) variant (*Hunke and Dukowicz*, 1997) remain the most widely used rheologies. However, work on improvements (ex.: *Hutchings et al.* (2004); *Chikhar et al.* (2019)) and completely different sea ice rheologies is ongoing to obtain a better representation of the large scale behavior of the ice. Focusing on the interplay between shear and divergence to create open waters, *Tremblay and Mysak* (1997) and *Sedlacek et al.* (2007) introduced a granular description of sea ice. Here, ice is treated as a collection of ice floes with friction between them and dilatation under shear to support the opening of leads. Considering floe size is rare but could be important, particularly in the case of smaller floes which, even if pressed together to form a complete ice cover, would be weaker in compression compared to the typical strengths used for sea ice since rafting would be facilitated. This has been used in descriptions of river ice (*Uzuner and Kennedy*, 1976) and may well apply to the MIZ as well (*Sutherland and Dumont*, 2018). Recognizing the importance of floes and LKFs for sea ice, *Schreyer et al.* (2006) proposed an elastic-decohesive representation of ice which enables a representation of subgrid leads in models. The elasto-brittle rheology (*Girard et al.*, 2011) also aimed at better characterization of failures, with a specific emphasis on reproducing the statistics of shear and divergence to obtain the proper scaling of ice deformation. *Tsamados et al.* (2013) developed an elastic anisotropic plastic rheology framework to reproduce the anisotropy present in observed sea ice features by accounting for it at the subgrid scale in the model. Although these newer rheologies introduced valuable improvements in models, they also present additional challenges in terms of implementation. For instance, the tracking of additional ice variables to represent the weakness of the ice in both the elastic-decohesive and elasto-brittle rheologies is best done in Lagrangian models, but sea ice models are currently mostly Eulerian. All rheologies also neglect thermodynamic or phase variables, such as ice temperature or brine content that could also be relevant (*Hunke et al.*, 2011).

Accurately describing sea ice dynamics can have far ranging consequences but remains challenging. Most notably, many relevant components are often omitted, such as waves interactions or grounding. Secondly, the exact way to describe the behavior of sea ice as a non-Newtonian fluid continuum is still up for debate, with many possible rheologies being proposed and fundamental factors such as floe size or the cohesion of the material still missing from most of them. In this context, ice models are a major tool to test hypothesis through process studies. They can also serve to highlight worthy research topics necessary to moving beyond the current successes in reproducing average conditions towards replicating specific situations better and addressing compensating errors. Investigating the details of ice dynamics at small scales in an idealized, simplified context instead of large-scale, complex situations could lead to a better integration of the current physical processes at play, to a greater understanding of errors and to possible improvements applicable to all sea ice models.

1.1.4 Numerical Modeling of Viscous-Plastic Sea Ice Dynamics

Numerical models of sea ice have been in development for decades (*Hibler III*, 1979), and their focus has slowly spread from large-scale, polar systems to include more regional applications (*Smith et al.*, 2013) as well as being part of global climate simulations (*Kushner et al.*, 2018). Because of the large difference between the vertical $O(\mathrm{m})$ and horizontal $O(100\ \mathrm{m})$ scales, the dynamics of sea ice are usually treated as a 2D problem with thickness and concentrations being tracked as state variables that also depend on thermodynamics. The most widespread form of the 2D momentum equation for sea ice is:

$$\rho h \frac{\partial \mathbf{u}_{2D}}{\partial t} = -\rho h f_C \mathbf{k} \times \mathbf{u}_{2D} + \boldsymbol{\tau}_a - \boldsymbol{\tau}_w + \nabla \cdot \boldsymbol{\sigma} - \rho h g \nabla H_d, \tag{1.4}$$

where ρ is the sea ice density, h is the mean ice thickness, $\mathbf{u}_{2D}$ is the horizontal velocity vector of sea ice, f_C is the Coriolis parameter, $\mathbf{k}$ is a unit vector perpendicular to the horizontal plane, τ_a and τ_w are the wind and water stresses, σ represents the internal ice stresses, g is the acceleration due to gravity and H_d is the sea surface height. This definition of the momentum equation ignores advection of momentum as well as snow cover. Over time and depending on the situation to be considered, other stresses can be added, such as wave radiation stress, τ_{wv} (*Sutherland and Dumont*, 2018), or basal stress τ_b (*Lemieux et al.*, 2015).

The main challenge in accurately solving the dynamics of sea ice as defined in Eq. 1.4 in a numerical model comes from the rheology term ($\nabla \cdot \boldsymbol{\sigma}$). The modeled behavior of such a complex material as sea ice is commonly approximated using VP rheology (*Hibler III*, 1979). Despite its age, this rheology is still widely used in the sea ice modeling community thanks to its relative simplicity and its ability to produce realistic results under a wide range of conditions (*Kreyscher et al.*, 2000). The VP rheology contains viscosity coefficients that depend non-linearly on strain rates and represent sea ice either as a very viscous Newtonian fluid under low deformations or as a plastic material that deform proportionally to the force applied once a critical stress value is reached (*Coon et al.*, 1974).

The strong dependence of stresses on deformations makes the momentum balance for sea ice under the VP rheology a stiff equation. Rapid changes in the magnitude of the viscosity coefficients used in the sea ice rheology can indeed occur under normal forcing, such as going from a diverging to a converging ice pack. To maintain numerical stability with an explicit integration scheme, a time step of the order of a second is required for simulations at a 100 km resolution (*Ip et al.*, 1991). Because of this, *Hibler III* (1979) solved the sea ice momentum equation with a VP rheology using an implicit approach. This departure from the explicit time-stepping methods typical in numerical modeling is a particularly costly part of sea ice simulations (*Lemieux et al.*, 2008, 2010; *Kushner et al.*, 2018). Sacrifices are often made in accuracy, either through lower model resolution or less accurate solution criteria, in order to maintain time efficiency (*Lemieux and Tremblay*, 2009).

Originally, Eq. 1.4 was solved using a Picard iteration with the Successive Over-Relaxation (SOR) method to solve the linearized system of equations(*Hibler III*, 1979). *Zhang and Hibler III* (1997) later introduced the line SOR method (LSOR) to improve the convergence rate when solving the linearized system of equations. The Picard non-linear solver requires many iterations (referred to as pseudo-time steps by *Zhang and Hibler III* (1997) and as outer loop iterations by *Lemieux et al.* (2008)) to converge to an accurate solution of the sea ice momentum equation with a VP rheology. The accuracy of the solution can have a significant effect on the ice velocity field as shown in Fig. 1.5. To reduce the computational cost and thus make higher accuracies more attainable, *Lemieux et al.* (2008) implemented the preconditioned Flexible Generalized Minimum RESidual (FGMRES, (*Saad*, 1993)) with SOR as a preconditioner to solve the linear system inside outer loops. Then, *Lemieux et al.* (2010) introduced a Jacobian-free version of Newton's method (*Knoll and Keyes*, 2004) to solve the full non-linear equation, resulting in a further decrease of required time by a factor of three or more, with increasing gains as the desired accuracy of the solution increases. More recently, *Losch et al.* (2014) have implemented a parallel JFNK for the sea ice component of the MIT-GCM and demonstrated a good scaling of JFNK for domain decompositions up to 1000 CPUs. Further improvement to the accuracy of the Jacobian-Free approximation (*Seinen and Khouider*, 2017) have also been made, followed by the evaluation of a method using the analytical Jacobian (*Mehlmann and Richter*, 2017).

In parallel to the development of implicit methods presented above, *Hunke and Dukowicz* (1997) introduced an artificial elastic term in the equations to reduce the stiffness of the

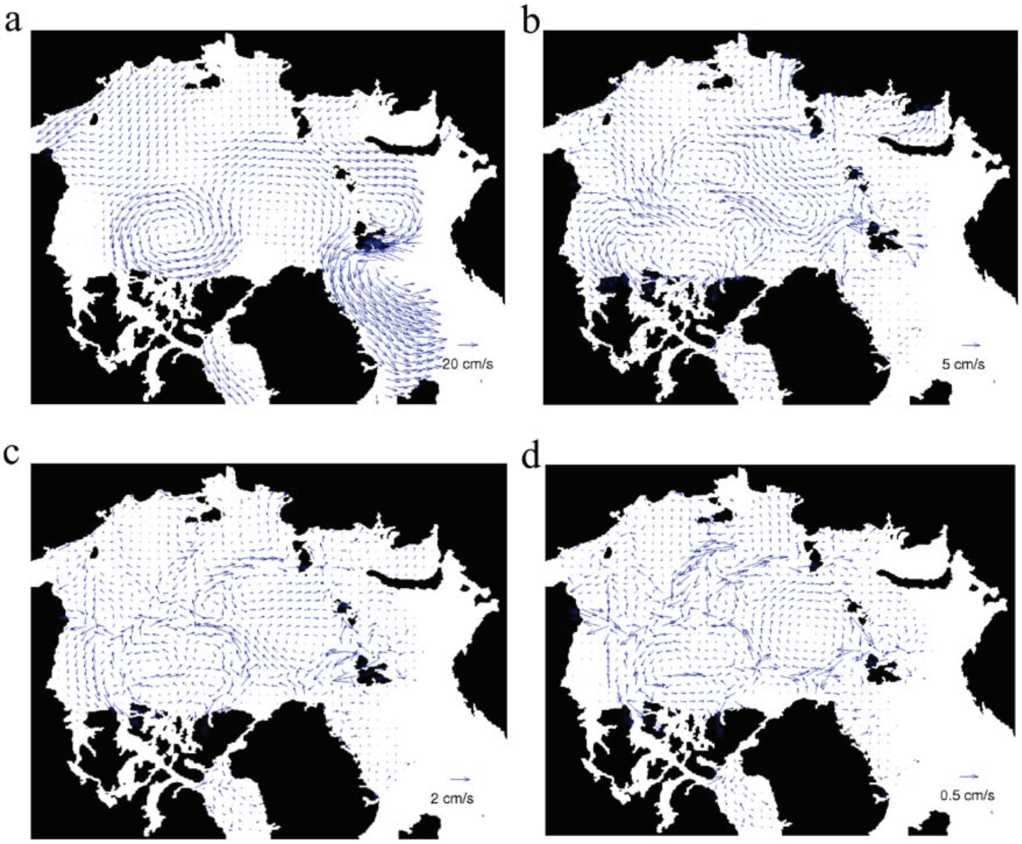

Figure 1.5: (a) Fully converged (10500 linear solver iterations) ice drift velocity field over the Arctic on 6 January 1997 0000 UT and errors when using 2 (b), 10 (c) and 40 (d) iterations. (Reproduced with permission from (*Lemieux and Tremblay*, 2009))

equation and allow an explicit integration with larger time steps. This Elastic-VP method (EVP, see also (*Hunke*, 2001)) has since been widely adopted by the sea ice modeling community. With this method, the additional elastic term allows elastic waves to distribute the stresses in sea ice until the other terms in the momentum equation can be in balance, in a process called sub-cycling. Implicit VP and explicit EVP methods should yield similar solutions since the elastic term of the EVP formulation should vanish once enough subcycles have been performed. However, *Losch et al.* (2010) have found the choice of numerical method between VP and EVP to have more impact than changes in other aspects of the model. There is evidence of residual elastic waves in solutions obtained using the EVP method in many studies (*König Beatty and Holland*, 2010; *Losch and Danilov*, 2012; *Lemieux et al.*, 2012; *Bouillon et al.*, 2013). *Losch and Danilov* (2012) also found EVP solutions to have smaller viscosity, especially near boundaries or in solid ice where the elastic time-scale is not fully resolved and the elastic waves not entirely damped. *Lemieux et al.* (2012) introduced a modification to the EVP model intended to ensure a converged solution would match one from a VP model. This approach was subsequently implemented and validated in the Louvain-la-Neuve sea Ice Model (LIM) by *Bouillon et al.* (2013). *Kimmritz et al.* (2015) confirmed the convergence of the new solver to its desired solution in 1D before upgrading both its efficiency and stability with the adaptive-EVP (aEVP) solver (*Kimmritz et al.*, 2016).

Numerical modeling of any systems has its specific kind of difficulty. In the case of sea ice, defining a rheology to represent sea ice, a fragmented solid, as a fluid is made all the more challenging by the interplay with model accuracy and numerical schemes. Furthermore, multiple forcing terms remain to be fully defined and implemented in a model with proper interactions between components to achieve realistic simulations. The changing climate leading to thinner, more mobile ice as well as the drive towards higher resolution simulations further increase the need for development in sea ice modeling.

1.2 Thesis objectives and structure

This research was motivated by two of the main topics in sea ice modeling. With increasing sea ice model resolutions, there is a need for computationally efficient and stable numerical methods. Additionally, observation and modeling capabilities have reached a point where a greater understanding of the MIZ dynamics is achievable. The two-way coupling of wave and ice models by combining wave propagation and attenuation with wave radiation stress, ice advection and compaction, in a time-dependent way, can enable modeling and forecast of the MIZ. Such a model opens up the analysis of transient states as well as steady-state solutions, widening the range of observations that can be used to further develop the theory of wave-ice interactions through testing the interplay of different formulations against observations and by making predictions that can then be tested. To achieve this, the main objectives of the thesis are the following:

1. To increase the reliability, efficiency and accuracy of sea ice momentum equation solvers by implementing an Analytical Jacobian Newton-Krylov (AJNK) solver.
2. To dynamically reproduce the spatial variability of sea ice thickness in the MIZ

through the balance between the wave radiation stress and ice strength.

3. To study how wave attenuation, wave radiation stress, ice thickness and rheology influence ice velocities near the ice edge.
4. To investigate the effects of waves on ice edge movement, air-sea interactions, heat fluxes and ice formation.

A one-dimensional model was chosen in this thesis work because of the one-dimensional approach taken in the literature to describe wave-ice interactions and the complexity of the numerics in sea ice models. In keeping with the objectives outlined above, the thesis is structured as follows: In chapter 2, the potential for improvements in accuracy and efficiency of models when solving the sea ice momentum equation by using the analytical Jacobian within a Newton-Krylov implicit solver (referred to as the AJNK solver) are examined. In chapter 3, wave-ice interactions are simulated through wave attenuation and wave radiation stress, establishing two-way coupling between the waves and ice components. This dynamic model of the MIZ is used to investigate how ice strength, wave attenuation and wave radiation stress can combine to reproduce the typical shape of sea ice thickness profiles observed in the MIZ. Then, in chapter 4, the system thus created, schematized in Fig. 1.6, is tested for its ability to create a sea ice jet at the ice edge and predictions of the velocity along a transect are made to be compared to future observations. Finally, in chapter 5, the model is used to predict ice drift velocities and combined with simple thermodynamics to showcase the possible impact of waves on ice edge location in polynyas.

Chapter 2 is based on work published as *Auclair et al.* (2017) and reproduced here with permission while chapters 3 and 4 are based on article drafts. As such, some background information in these chapters may be similar to that found in section 1.1 or between chapters.

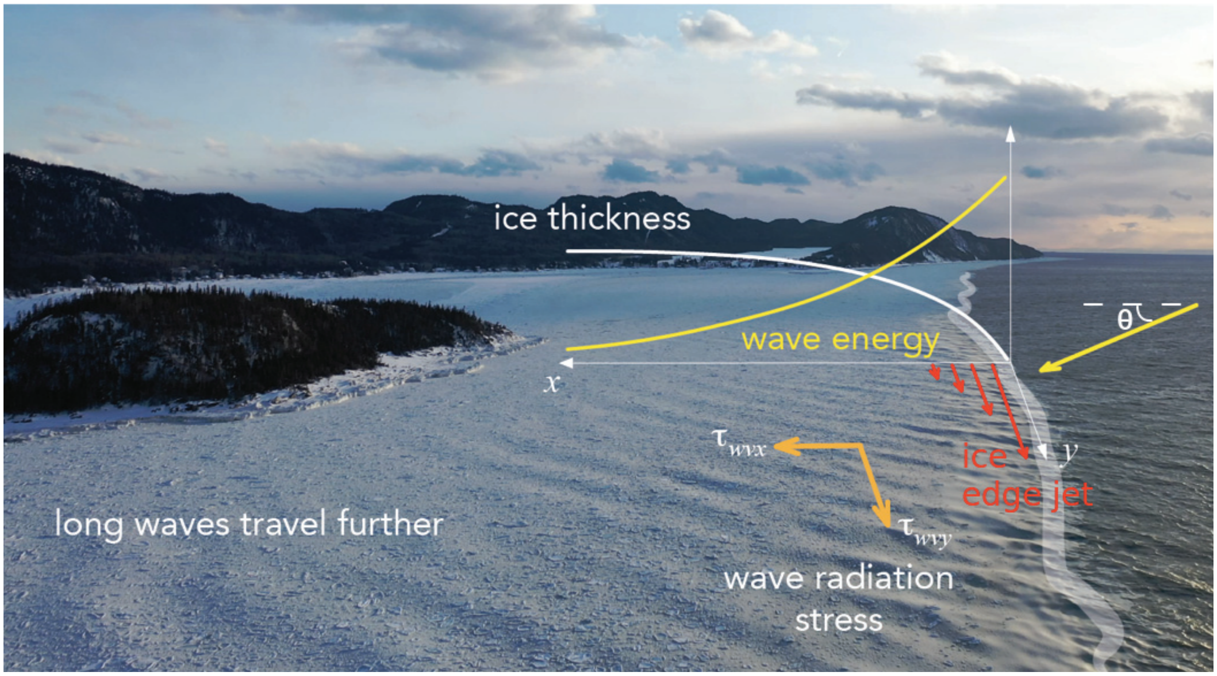

Figure 1.6: Schematic of processes to be considered in a one-dimensional time-dependent MIZ model. This picture was taken by an unmanned aerial vehicle in the coastal area surrounding the Bic national Park, Rimouski, in the St. Lawrence Estuary. Photo credit: Dany Dumont (2019).

CHAPTER 2

IMPLEMENTATION OF NEWTON'S METHOD WITH AN ANALYTICAL JACOBIAN TO SOLVE THE 1D SEA ICE MOMENTUM EQUATION [1]

The main challenge in solving the dynamics of sea ice comes from its rheology which describes the relationship between stress and strain. The modeled behavior of such a complex material as sea ice on the considered scales can be approximated using the viscous-plastic (VP) rheology (*Hibler III*, 1979). Using viscosity coefficients that depend nonlinearly on strain rates, this rheology represents sea ice either as a very viscous Newtonian fluid under low deformations or as a plastic material once critical stress values have been reached (*Coon et al.*, 1974). Other rheologies have also been proposed, however they have not been widely adopted. This is explained by the fact that there is still not one rheology which can clearly provide the best representation of sea ice mechanics. Furthermore, these alternative rheologies typically present additional challenges in terms of implementation such as requiring the tracking of additional ice variables. Hence, the VP rheology is still commonly used in the sea ice modeling community thanks to its relative simplicity and its ability to produce realistic results under a wide range of conditions (*Kreyscher et al.*, 2000). This chapter will focus on the VP rheology for the same reasons.

The momentum equation for sea ice under the VP rheology is a stiff equation. This is due to the possibility of rapid changes in the magnitude of the viscosity coefficients

---

[1] This chapter is based on work published as *Auclair et al.* (2017).

used in the sea ice rheology under normal forcing, such as going from a diverging to a converging ice pack. The strong gradients in the coefficients can deteriorate the numerical convergence of the applied numerical schemes. Another challenge arises from how most sea ice models treat the ice strength explicitly when solving the momentum equation, allowing unrealistic ice stress gradients to develop when using a large time step. This splitting in time causes noise in the numerical solution and can even lead to numerical instability. To address this, *Lemieux et al.* (2014) refined the integration scheme in VP sea ice models, using an IMplicit-EXplicit (IMEX) scheme to update the explicitly treated ice concentration and thickness within the iterations of the implicit momentum solver. The removal of this splitting in time of the equations to be solved enabled the use of larger time steps by reducing the numerical noise created otherwise. From a physical point of view, this is related to the propagation of a plastic wave in rigid regions of sea ice identified in models using the VP rheology by *Williams et al.* (2017a). Appropriately resolving the plastic waves, which propagate at much faster speeds than that of the ice itself, imposes an even stricter constraint on possible time steps in VP models.

In this chapter, we investigate the potential of using the analytical Jacobian within a Newton-Krylov solver (the Analytical Jacobian Newton Krylov method: AJNK) and as the preconditioning matrix to solve the one-dimensional (1D) sea ice momentum equation. The JFNK method (similar to the approach of (*Lemieux et al.*, 2010, 2012; *Losch et al.*, 2014)) is the baseline used for comparison in this study. It is expected that using the analytical Jacobian would improve the order of convergence of the non-linear solver compared to the Jacobian-Free method (*Eisenstat and Walker*, 1994). Solving the 1D sea ice momentum equation is a stringent test for robustness and convergence of the Newton solver (see *Lemieux et al.* (2014)). The work presented here is therefore a valuable step for the development of an AJNK solver for two-dimensional (2D) applications. Possible gains in numerical efficiency, as tested here, can be important to improve model skill by removing noise or sharpening velocity gradients or to reduce the computational effort to obtain a given accuracy.

This chapter is structured as follows. In section 2.1, the governing equations of sea ice dynamics in 1D are described. Section 2.2 contains a description of the numerical scheme used to implement the solver, including the discretization of the equations, Newton's method, the derivation of the analytical Jacobian and the preconditioners. The experiments performed to test the new AJNK solver against the reference JFNK solver are described in section 2.3 and the results are detailed in section 2.4, with a distinction being made between local (subsection 2.4.1) and global (subsection 2.4.2) convergence. Discussion of the results and the conclusion are provided in section 2.5.

2.1 1D sea ice momentum equations

In the 1D model used for this study, the water under the ice is considered to be at rest. The advection of ice momentum is also neglected as done in most sea ice models (e.g., *Zhang and Hibler III* (1997), *Hunke* (2001)). Together with the reduction in dimensionality, this allows Eq. 1.4 to be simplified into:

$$\rho h \frac{\partial u}{\partial t} = \tau_a - \tau_w + \frac{\partial \sigma}{\partial x}, \tag{2.1}$$

where u is the 1D sea ice velocity and we redefine the internal stress $\sigma = \sigma_{xx}$. Both of these are now scalars, along with the air and water stresses, τ_a and τ_w. A full derivation of the 1D sea ice momentum equation is presented in *Lipscomb et al.* (2007).

Quadratic drag formulas are used in the model (*McPhee*, 1975). The ice speed is neglected in the air drag formulation as it is much slower than wind speed. With the ocean being kept at rest, the water velocity is also absent from the water drag. This yields the following drag relationships:

$$\tau_a = \rho_a C_{da} |u_a| u_a \tag{2.2}$$

$$\tau_w = \rho_w C_{dw} \sqrt{u^2 + \varepsilon_1} u \tag{2.3}$$

where ρ_a, ρ_w, C_{da} and C_{dw} are the densities and drag coefficients of air and water, respectively, u_a is the surface wind and ε_1 is a small number (10^{-10} $\mathrm{m}^2/\mathrm{s}^2$) introduced to avoid dividing by 0 in our implementation of the Jacobian.

In 1D, since all other components vanish, the divergence of the stress tensor as defined in *Hibler III* (1979) can be reduced to:

$$\frac{\partial \sigma}{\partial x} = \frac{\partial}{\partial x}\left[(\eta + \zeta)\frac{\partial u}{\partial x} - \frac{P}{2}\right]. \tag{2.4}$$

where

$$\zeta = \frac{P_p}{2\Delta} \tag{2.5}$$

and

$$\eta = \zeta \mathrm{e}^{-2} \tag{2.6}$$

are the bulk and shear viscosities, P_p is the ice strength, P is a pressure term function of both ice thickness and strain rates and e is the ellipticity of the sea ice yield curve (*Hibler III*, 1979). Similarly, in 1D, Δ can be simplified to

$$\Delta = \left[\left(1 + \mathrm{e}^{-2}\right)\left(\left(\frac{\partial u}{\partial x}\right)^2 + \varepsilon_2\right)\right]^{\frac{1}{2}}, \tag{2.7}$$

where $\varepsilon_2 = 10^{-22}\,\mathrm{s}^{-2}$ is introduced in order to prevent Δ from becoming 0 when in the denominator in computations of ζ and the Jacobian.

The ice strength, P_p, is expressed as

$$P_p = P^* h \exp[-C(1 - A)], \tag{2.8}$$

where P^* and C are the strength and concentration parameters ($P^* = 27500\,\mathrm{Nm}^{-2}$, $C = 20$) and A is the sea ice concentration.

Following *Lemieux and Tremblay* (2009), ζ is capped to a maximum value which characterizes the viscous regime. To maintain a continuous derivative, this is done using a hyperbolic tangent:

$$\zeta = \frac{P_p}{2\Delta_{min}} \tanh\left(\frac{\Delta_{min}}{\Delta}\right) \tag{2.9}$$

with $\Delta_{min} = 2\mathrm{x}10^{-9}\,\mathrm{s}^{-1}$ in accordance with the ζ_{max} definition in (*Hibler III*, 1979).

Finally, in order to prevent the development of ice drift in the absence of forcing (*Kreyscher et al.*, 2000), we use a replacement closure to define P as

$$P = 2\zeta\Delta. \tag{2.10}$$

2.2 Numerical Scheme

2.2.1 Discretization

We use a backward Euler scheme for the momentum equation. The continuity equations of the ice thickness and the ice concentration are solved explicitly with a Forward Euler scheme. The governing equations are thus solved in a two step process, with the momentum balance being first solved iteratively for the new ice velocities, which are then used to advect the ice thickness and concentration according to the continuity equations. The time-discretized momentum equation in 1D is written as

$$\rho h^{n-1}\frac{(u^n - u^{n-1})}{\Delta t} = \tau_a^n - \tau_w^n + \frac{\partial \sigma^n}{\partial x}, \tag{2.11}$$

where the superscript n denotes the current time level, and $n-1$ is the previous, known, time level. We use a one-thickness category model. Once the velocity u^n has been found, the continuity equations for both concentration and thickness are solved explicitly:

$$\frac{(h^n - h^{n-1})}{\Delta t} + \frac{\partial}{\partial x}(u^n h^{n-1}) = 0, \tag{2.12}$$

$$\frac{(A^n - A^{n-1})}{\Delta t} + \frac{\partial}{\partial x}(u^n A^{n-1}) = 0. \tag{2.13}$$

Spatially, the model uses a 1D version of the Arakawa C-grid *Arakawa and Lamb* (1977), with tracers defined at the center of grid cells and velocities defined at the vertices (Fig. 2.1a). Homogeneous Dirichlet boundary conditions are applied ($u = 0$) at both edges of the model domain. Spatial derivatives are discretized using a second-order centered difference scheme. For a number of tracer points nx, the discretization of the momentum equation creates a system of $nx + 1$ equations.

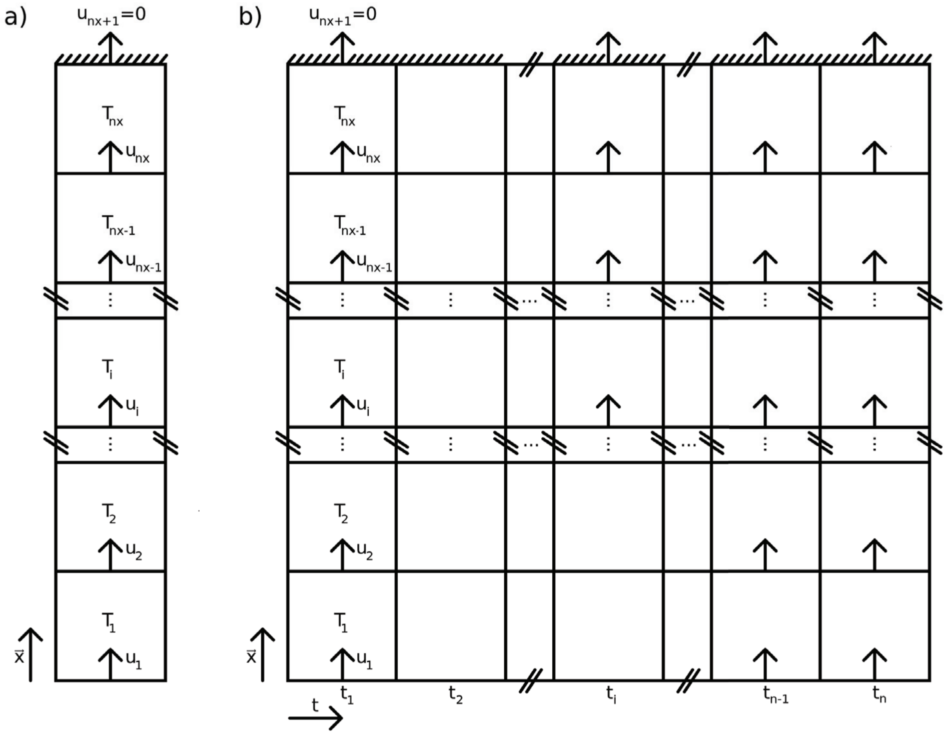

Figure 2.1: Diagram illustrating a) the model domain for nx tracer points (T_1 to T_{nx}) and the associated $nx + 1$ velocities (u_1 to u_{nx+1}) with the ice being pushed towards the closed top boundary (shoreline) and b) the way output is presented for multiple time steps side-to-side and time increasing from left to right.

2.2.2 Newton's method

Starting with the velocity solution from the previous time level, $(\mathbf{u}^{n-1})$, as an initial iterate, we are looking for a solution to the problem $\mathbf{F}(\mathbf{u^n}) = 0$, where $\mathbf{F}(\mathbf{u^n})$ is the difference between the right-hand and left-hand sides of Eq. 2.11 evaluated at each of the $nx + 1$ velocity points of the model. We now drop the superscript n, knowing that we want to find the solution $\mathbf{u} = \mathbf{u}^n$ through a series of iterates $\mathbf{u}^1, \mathbf{u}^2, \mathbf{u}^3, ..., \mathbf{u}^k, ...$ with the index k=1,2,3,... referring to the iterate number. We evaluate the quality of the solution at a given iteration by calculating $||\mathbf{F}(\mathbf{u^k})||$, where $|| \cdot ||$ denotes the L2-norm. This is referred to as the nonlinear residual of a given iteration.

Newton's method is based on a first order multivariate Taylor expansion of the function $\mathbf{F}(\mathbf{u})$ around a point, here taken to be $\mathbf{u}^{k-1}$, as

$$\mathbf{F}(\mathbf{u}^k) = \mathbf{F}(\mathbf{u}^{k-1} + \delta\mathbf{u}^k) \approx \mathbf{F}(\mathbf{u}^{k-1}) + \mathbf{J}(\mathbf{u}^{k-1})\delta\mathbf{u}^k. \tag{2.14}$$

where $\delta\mathbf{u}^k$ is the correction to be added to $\mathbf{u}^{k-1}$ to obtain $\mathbf{u}^k$ and $\mathbf{J} \equiv \mathbf{F}^{'}$ is the Jacobian matrix of the function $\mathbf{F}(\mathbf{u})$. The Jacobian is a $nx + 1 \times nx + 1$ matrix with elements defined as $\mathrm{J}_{i,j} = \partial \mathrm{F}_i(\mathbf{u})/\partial u_j$, where i and j go from 1 to $nx + 1$.

Given Eq. 2.14, looking for a velocity $\mathbf{u^k}$ such that $\mathbf{F}(\mathbf{u^k}) = 0$ is equivalent to looking for $\delta\mathbf{u}^k$ such that

$$\mathbf{F}(\mathbf{u}^{k-1}) + \mathbf{J}(\mathbf{u}^{k-1})\delta\mathbf{u}^k = 0, \tag{2.15}$$

up to a certain accuracy. This linear system of equations is solved using the preconditioned FGMRES (*Saad*, 1993) method. By defining a loose convergence criterion for FGMRES similarly to *Lemieux et al.* (2014), we obtain an inexact Newton method, which offers advantages in both robustness and numerical efficiency (*Eisenstat and Walker*, 1996). Once $\delta\mathbf{u^k}$ has been found, we use a linesearch approach to obtain $\mathbf{u^k} = \mathbf{u^{k-1}} + \lambda\delta\mathbf{u^k}$ where $\lambda = \left[1, \frac{1}{2}, \frac{1}{4}, \frac{1}{8}\right]$ is successively reduced until $||\mathbf{F}(\mathbf{u^k})|| < ||\mathbf{F}(\mathbf{u^{k-1}})||$ or until $\lambda = \frac{1}{8}$, ensuring that the largest possible step is taken that still yields an improvement, or, should no improvement be found, only a minimal step is taken (*Knoll and Keyes*, 2004). Once $\mathbf{u^k}$ has been chosen, the norm $||\mathbf{F}(\mathbf{u^k})||$ is compared to the initial norm $||\mathbf{F}(\mathbf{u^0})||$. The nonlinear problem is considered to be solved as soon as

$$||\mathbf{F}(\mathbf{u^k})|| < \gamma_{nl}||\mathbf{F}(\mathbf{u^0})|| \tag{2.16}$$

where γ_{nl} is the convergence criterion for Newton's method, the required improvement factor for the norm of the residual of Eq. 2.11, chosen to be 10^{-6} for this study. The nonlinear solver fails to converge if this criterion is not met within 150 Newton iterations.

2.2.3 Forming the Jacobian

In order to solve Eq. 2.15 with a Krylov method, it is necessary to compute the Jacobian-vector product, but not necessarily the Jacobian itself (*Knoll and Keyes*, 2004). The simplest manner in which to obtain this product is an application of a first-order forward finite difference, to the product of the Jacobian, $\mathbf{J}(\mathbf{u})$, with a vector $\mathbf{v}$:

$$\mathbf{J}(\mathbf{u}^{k-1})\mathbf{v} \sim \frac{\mathbf{F}(\mathbf{u}^{k-1}+\epsilon\mathbf{v})-\mathbf{F}(\mathbf{u}^{k-1})}{\epsilon}, \tag{2.17}$$

where ϵ is a small quantity taken here to be 10^{-7}. We refer to using Eq. 2.17 as the Jacobian-free product calculation. The Jacobian Free Newton-Krylov (JFNK) method is then defined as solving Eq. 2.15 using Newton's method with Eq. 2.17 to approximate the product. It is relevant to note that the value of ϵ can have an impact on the convergence of a JFNK method (*Losch et al.*, 2014; *Godoy and Liu*, 2012). Values both larger and smaller may change the convergence of the method by changing the result of the approximation, in degrees that depend on computer accuracy as well as the situation being modeled. The value chosen here has proven to be optimal in a test subset of the experiments performed in this study.

The main focus of this paper, is to instead derive the Jacobian analytically from the discretized version of $\mathbf{F}$, and then calculate the product. We refer to the use of this product as the Analytical Jacobian Newton-Krylov (AJNK) method. An element of the Jacobian is defined by

$$\mathrm{J}_{i,j} = \frac{\partial \mathrm{F}_i(\mathbf{u})}{\partial u_j} = \frac{\rho h_i}{\Delta t}\delta_{i,j} + \frac{\partial}{\partial u_j}\left(\tau_{w,i} - \left.\frac{\partial \boldsymbol{\sigma}}{\partial x}\right|_i\right), \tag{2.18}$$

where $\delta_{i,j}$ is the Kronecker delta, equal to one only if $i = j$, zero otherwise and $\mathbf{u}$ and $\boldsymbol{\sigma}$ are the vector of velocities and internal ice stress at every model grid point. The first term on the left-hand side comes from the time derivative of F_i. The wind stress τ_a has been dropped from Eq. 2.18 because it does not depend on the ice velocity but both water drag and internal stresses are kept.

From Eq. 2.3, we see that the water drag only depends on u_i. The water drag term in Eq. 2.18 is thus non-zero only if $i = j$. It can be expanded into

$$\frac{\partial \tau_{w,i}}{\partial u_i} = \rho_w C_{dw} \left[\left(u_i^2 + \varepsilon_1\right)^{-\frac{1}{2}} u_i^2 + \left(u_i^2 + \varepsilon_1\right)^{\frac{1}{2}} \right] \tag{2.19}$$

In the internal stress terms, velocity appears in gradient calculations. Since we are interested in the gradient at a given tracer point (to be denoted T_i, located to the right of the velocity point u_i), it can be approximated as

$$\left.\frac{\partial \mathbf{u}}{\partial x}\right|_{T_i} = \frac{u_{i+1} - u_i}{\Delta x}, \tag{2.20}$$

from which we obtain

$$\left.\frac{\partial}{\partial u_j} \frac{\partial \mathbf{u}}{\partial x}\right|_{T_i} = \frac{\delta_{i+1,j} - \delta_{i,j}}{\Delta x}. \tag{2.21}$$

Using Eq. 2.21 in combination with Eq. 2.7, we obtain the derivative of Δ:

$$\begin{aligned} \frac{\partial \Delta_i}{\partial u_j} &= \left(1 + \mathrm{e}^{-2}\right)^{\frac{1}{2}} \left(\left(\frac{\partial \mathbf{u}}{\partial x} \right)^2 + \varepsilon_2 \right)^{-\frac{1}{2}} \left. \frac{\partial \mathbf{u}}{\partial x} \frac{\partial}{\partial u_j} \frac{\partial \mathbf{u}}{\partial x} \right|_{T_i} \\ &= \frac{1 + \mathrm{e}^{-2}}{\Delta_i} \left. \frac{\partial \mathbf{u}}{\partial x} \right|_{T_i} \frac{\delta_{i+1,j} - \delta_{i,j}}{\Delta x}. \end{aligned} \tag{2.22}$$

This, with Eq. 2.9, gives the derivative of the bulk viscosity as

$$\begin{aligned} \frac{\partial \zeta_i}{\partial u_j} &= \frac{P_p}{2} \left(1 - \tanh^2 \left(\frac{\Delta_{min}}{\Delta_i} \right) \right) \frac{-1}{\Delta_i^2} \frac{\partial \Delta_i}{\partial u_j} \\ &= \left(\frac{2}{P_p} \Delta_{min}^2 \zeta_i^2 - \frac{P_p}{2} \right) \frac{1}{\Delta_i^2} \frac{\partial \Delta_i}{\partial u_j}. \end{aligned} \tag{2.23}$$

which is refactored to make use of already computed variables. Using the derivatives from Eqs. 2.22 and 2.23, the derivative of internal stresses can then be obtained. The derivative of the first part of the rheology term is:

$$
\begin{aligned}
\frac{\partial}{\partial u_j}\frac{\partial}{\partial x}\left[(\eta+\zeta)\frac{\partial \mathbf{u}}{\partial x}\right]_{u_i} &= \frac{\partial}{\partial u_j}\frac{1}{\Delta x}\left[(\eta_i+\zeta_i)\left.\frac{\partial \mathbf{u}}{\partial x}\right|_{T_i} - (\eta_{i-1}+\zeta_{i-1})\left.\frac{\partial \mathbf{u}}{\partial x}\right|_{T_{i-1}}\right] \\
&= \frac{1+e^2}{\Delta x^2}\left[\frac{\partial \zeta_i}{\partial u_j}(u_{i+1}-u_i)+\zeta_i(\delta_{i+1,j}-\delta_{i,j})\right. \\
&- \left.\frac{\partial \zeta_{i-1}}{\partial u_j}(u_i-u_{i-1})-\zeta_{i-1}(\delta_{i,j}-\delta_{i-1,j})\right]. \qquad (2.24)
\end{aligned}
$$

From Eq. 2.10, derivative of the pressure term is:

$$
\begin{aligned}
\frac{\partial}{\partial u_j}\left[-\frac{\partial}{\partial x}\frac{\mathbf{P}}{2}\right]_{u_i} &= -\frac{\partial}{\partial u_j}\frac{\partial}{\partial x}\Delta\zeta\Big|_{u_i} \qquad (2.25) \\
&= -\frac{1}{\Delta x}\left[\Delta_i\frac{\partial \zeta_i}{\partial u_j}+\zeta_i\frac{\partial \Delta_i}{\partial u_j}-\Delta_{i-1}\frac{\partial \zeta_{i-1}}{\partial u_j}-\zeta_{i-1}\frac{\partial \Delta_{i-1}}{\partial u_j}\right]
\end{aligned}
$$

By combining Eqs. (2.18, 2.19, 2.24 and 2.25, the analytical Jacobian can be calculated and its product with a vector is then a matter of simple linear algebra.

2.2.4 Preconditioning

Preconditioning is applied in order to transform the linear system of equations into an equivalent one with the same solution but for which the convergence properties of a given solver are improved. FGMRES is based on right preconditioning and allows the preconditioning operator to vary from one Krylov iteration to the next *Saad* (1993). Here, the preconditioning operator is based on performing 10 iterations of a SOR solver. Given a vector $\mathbf{q}$ formed during the Krylov process, the preconditioning operator, $\mathbf{P}_0^{-1}$, applied to it leads to $\mathbf{r} = \mathbf{P}_0^{-1}\mathbf{q}$. $\mathbf{P}_0^{-1}$ should not be viewed as the inverse of a matrix. A good preconditioning operator is one that approximates the inverse of the system matrix $\mathbf{J}$ but that is computationally efficient to apply.

In our approach, SOR is applied to the system

$$\mathbf{Mt} = \mathbf{q}, \qquad (2.26)$$

where $\mathbf{M}$, as described below, is a matrix derived from the system matrix $\mathbf{J}$ and $\mathbf{t}$ would be the exact solution. Since SOR is interrupted before converging completely to $\mathbf{t}$, the approximate solution $\mathbf{r}$ is obtained instead.

Here, two different matrices $\mathbf{M}$ are used for the preconditioning operators. Since it has been derived, we are able to make use of the Jacobian, $\mathbf{J}(\mathbf{u}^{k-1})$, itself. We also expand the residual, $\mathbf{F}(\mathbf{u}^{k-1})$, as

$$\mathbf{F}(\mathbf{u}^{k-1}) = \mathbf{A}(\mathbf{u}^{k-1})\mathbf{u}^{k-1} - \mathbf{b} \tag{2.27}$$

where the matrix $\mathbf{A}$ represents terms with an explicit dependence on velocity at the current time step and the vector $\mathbf{b}$ contains the forcing terms independent of the ice velocity or dependent on previous, known values. The matrix $\mathbf{A}$ is the Picard matrix. Note that the Picard matrix is an approximation of the Jacobian since $\mathbf{J}$ can be written as

$$\mathbf{J}(\mathbf{u}^{k-1}) = \mathbf{A}'(\mathbf{u}^{k-1})\mathbf{u}^{k-1} + \mathbf{A}(\mathbf{u}^{k-1}) \tag{2.28}$$

where the primes denote differentiation of the matrix $\mathbf{A}$ with regard to velocity.

We refer to using $\mathbf{M} = \mathbf{A}$ for the preconditioning operator as the Picard preconditioner while we use the expression Jacobian preconditioner when using $\mathbf{M} = \mathbf{J}$.

By combining these two preconditioners with either the JFNK or AJNK methods, we obtain four methods to solve the momentum equation which we identify by the method first, followed by the preconditioner: JFNK-P, JFNK-J, AJNK-P and AJNK-J.

2.3 Numerical experiments

For all experiments, the 1D model domain is 2000 km long with closed boundaries ($u_1 = u_{nx+1} = 0$ as shown in Fig. 2.1) and the integration time is 6 days. The experiments include a range of resolutions, time steps and initial conditions. To encompass the distinct challenges created by high and low resolutions, the model was run with resolutions of 1, 2, 5, 10, 20 and 40 km. Time steps of 0.5, 1, 1.5, 3, 5, 10, 20, 30 and 60 minutes were considered. We exclude those combinations of spatial and time resolutions from our consideration that do not meet the CFL (Courant-Friedrichs-Lewy) criterion. Assuming a maximum ice velocity of $1\ \mathrm{m/s}$, which can be observed in realistic simulations, this means that time steps greater than 20 minutes for the $1\ \mathrm{km}$ resolution or of an hour for the $2\ \mathrm{km}$ resolution are excluded. Cells that correspond to these combinations are left blank in the upcoming figures.

A set of three different initial conditions were used for experiments. The simplest one represents loose pack ice covering the model domain, with concentrations (A) of 0.7 and ice thickness (h) of 1 meter (referred to as 'Leads' experiments). Experiments were also initialized with solid ice coverage ($A = 1$, $h = 1$ m, referred to as 'Solid' experiments) and an ice slab ($A = 1$, $h = 1\ \mathrm{m}$ in the center of the domain, and A =0, $h = 0\ \mathrm{m}$ for 200 km at both ends of the domain, referred to as 'Slab' experiments).

Since the ocean is considered to be at rest in this model, the only forcing to be varied is the wind forcing. To generate the wind forcing, three different temporal and spatial patterns were used. Temporally, the wind was chosen to be either constant at a value $|\mathbf{u}_0| = 10\ \mathrm{m/s}$ for the entire model simulation, gradually increasing as $\mathbf{u}_a(t) = (1 - e^{-t/\tau_r})\mathbf{u}_0$, where τ_r is set to six hours, or varying as $\mathbf{u}_a(t) = \mathbf{u}_0 \sin(2\pi t/\tau_s)$, where τ_s is set to three days. These three different wind forcings evolutions are referred to as "Constant", "Ramp-up" and "Oscillating", respectively.

Spatially, the wind was chosen to be either "Uniform", or modulated by a sinusoid amplitude of the form $\mathbf{u}_a(t, x) = \pm\mathbf{u}_a(t)\sin(2\pi x/L)$ where L is the length of the model domain. A positive value is used to create a "Convergent" wind over the center of the domain, while keeping the winds varying smoothly and at a value of 0 at the boundary. A negative value creates a similar "Divergent" wind field over the center of the model domain. The wind spatial and temporal patters are combined to create the possible wind fields (see Fig. 2.2).

Experiments were performed for every combination of forcing, initial condition, resolutions and solvers. This allows to test the model under conditions ranging from the simpler case of uniform, constant winds with partial ice cover to the more complex spatially and temporally varying conditions.

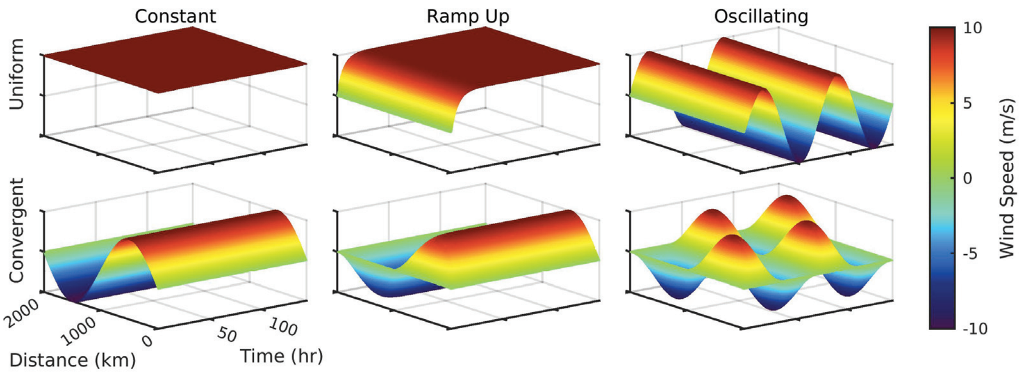

Figure 2.2: Spatial and temporal variations of the wind forcings. Vertically: constant (top), ramping up (middle), oscillating (bottom). Horizontally: uniform (left), convergent (right). Note: divergent winds are omitted, being a mirror image of the convergent ones about the spatial center of the model domain.

2.4 Results

In several simulations, it is possible for the Newton solver to fail to converge to a solution. Since the last iterate of one time level is used as the first of the next, a failed convergence can compromise the convergence of the following iterate. A series of failed convergences can create a disconnect between the forcing and velocity fields and contaminate the rest of the run. The possibility of this kind of failure is specific to 1D simulations and their necessarily idealized winds. Such a series of bad initial iterates could lead to an inflation of the computational statistics. Therefore, runs where more than 5% of the time levels were not solved successfully are not used in the analysis of numbers of iterations and neither are their equivalent for other nonlinear solver and preconditioner pairs. Because of this, figures containing average numbers of iterations may have blank cells where no result was kept as a consequence of this criterion. However, these model runs do contribute to the mean failure percentages presented in this section which are used to investigate the global convergence, or robustness, of the different solvers.

Specific example cases using the Leads initial conditions are used to highlight the reason behind trends noticed when looking at averages over all simulations. This choice of initial conditions allows the consideration of both times when the impact of the rheology is weak and when it is strong, before and after the ice gets compacted by the wind. Simulations performed using the Slab and Solid initial conditions are used in all aggregated results.

2.4.1 Local convergence

Once the approximate solution approaches the actual solution, Newton's method ensures quadratic convergence. For an inexact Newton-Krylov method, slower convergence is expected overall but it should remain fastest near the solution, in the local convergence phase. Since the solution of the previous time level is used as the initial iterate for the next one, a smaller time step generally means a better initial iterate and, relatively, more iterations of the solver spent in local, rapid convergence to the solution. Along with the quality of the initial iterate, the accuracy of the linear solution can also impact the convergence of Newton's method.

2.4.1.1 Impact of ice characteristics

The Jacobian preconditioner reduces the number of iterations required to reach the solution at the desired accuracy with Newton's method by about one third for the constant winds Leads case (see Fig. 2.3, top versus bottom rows). In this case, the change between methods used for the computation of the $\mathbf{Jv}$ product has little impact and columns of Fig. 2.3 are similar, but the increased precision granted by the Jacobian preconditioner to the linear solver in turn improves the convergence of Newton's method.

There is also a significant effect of the preconditioner on the number of FGMRES iterations required to solve the linear problem (see Fig. 2.4). Using the Jacobian preconditioner decreases the number of iterations required markedly beyond the first 30 hours of the simulation. This coincides with the accumulation of ice along the model boundary, an increase of ice concentration towards 100% and the rheology term becoming more important. Without the Jacobian preconditioner, the model eventually fails to properly solve the linear problem in the 50 allocated iterations for FGMRES. This explains the slower convergence of the Newton solver (Fig. 2.3, top row).

2.4.1.2 General solver efficiency

On grids with a spacing (Δx) of 5 km or above, when considering averages over all forcing and initial conditions combinations, using the Jacobian preconditioner and the AJNK method, either independently or together, reduces the number of Newton iterations

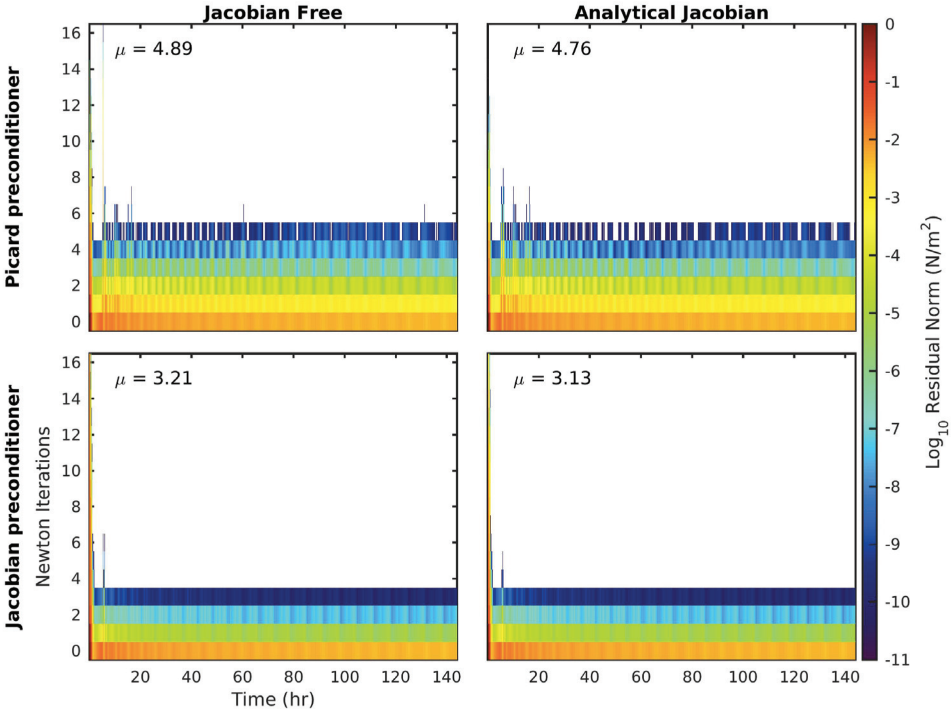

Figure 2.3: L2-norm of the nonlinear residual and average number of iterations to reach convergence, μ, when using constant uniform winds with Leads initial conditions, $\Delta x = 10\ \mathrm{km}$ and $\Delta t = 5\ \mathrm{min}$ and the JFNK-P (top left), AJNK-P (top right), JFNK-J (bottom left) and AJNK-J (bottom right) methods.

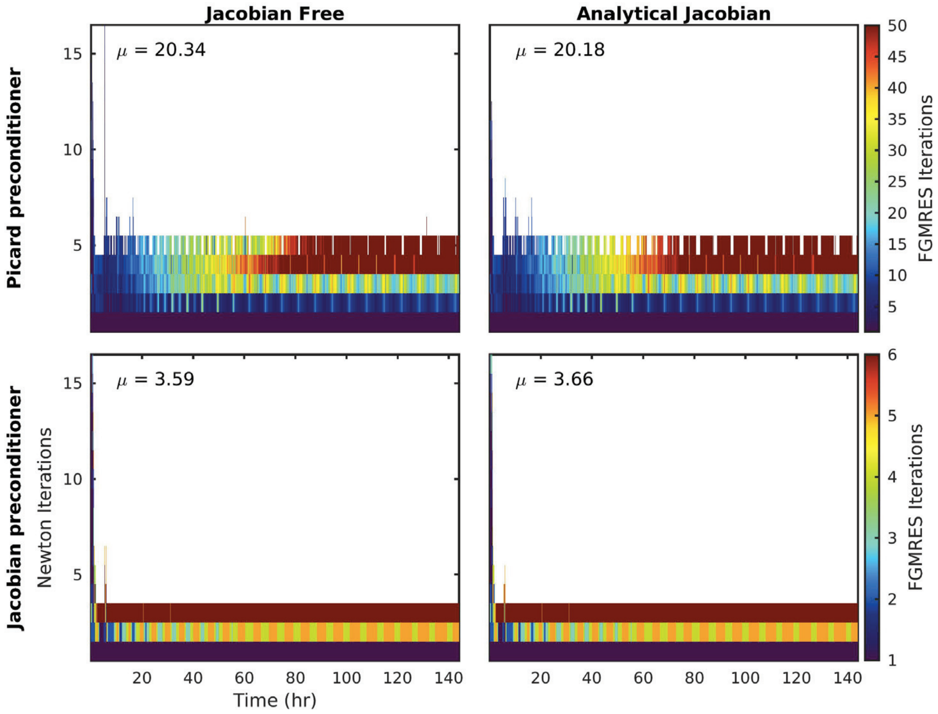

Figure 2.4: Number of FGMRES iterations and average number of iterations to reach convergence, μ, when using constant uniform winds with Leads initial conditions, $\Delta x = 10\ \mathrm{km}$ and $\Delta t = 5\mathrm{min}$ and using the JFNK-P (top left), AJNK-P (top right), JFNK-J (bottom left) and AJNK-J (bottom right). Note the use of different color bars.

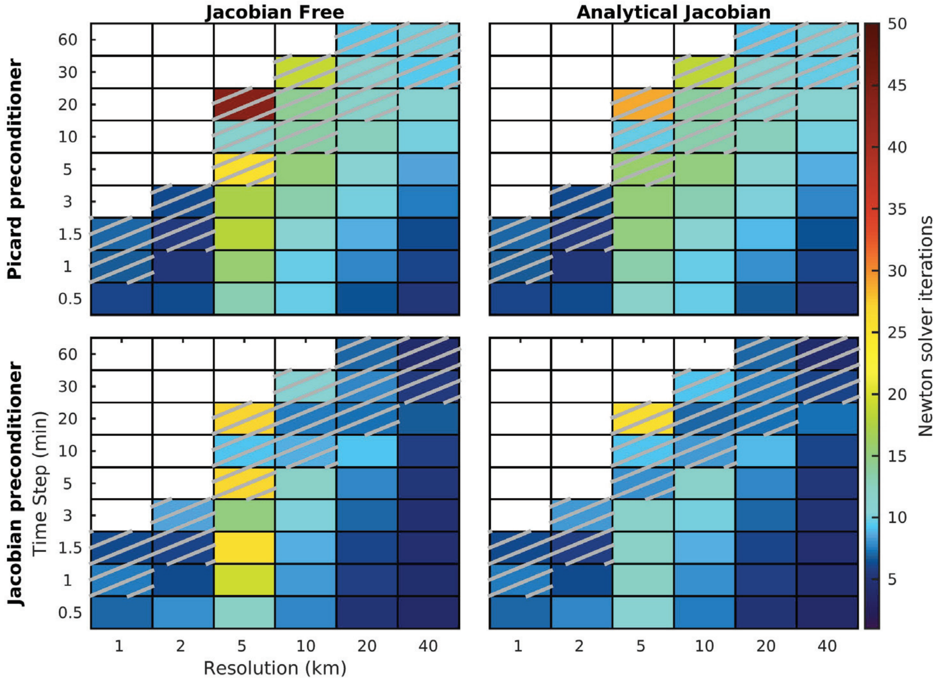

Figure 2.5: Average number of Newton iterations required to achieve convergence using the JFNK-P (top left), AJNK-P (top right), JFNK-J (bottom left) and AJNK-J (bottom right). Hatching identifies the possibility of unresolved plastic wave in the ice.

required on average (Fig. 2.5), similarly to the Constant-Uniform Leads case shown above. However, at higher resolutions, the model requires less iterations when using the Picard preconditioner.

Certain cases were challenging for the model at 5 km and required a large number of iterations to solve. Many of these failed, as described above, at 1 and 2 km resolutions and were thus discarded from the convergence analysis presented here. The removal of these cases from the comparison explains the apparent sharp decrease in required number of iterations at resolutions of 1 and 2 km compared to 5 km in Fig. 2.5, not improved model performance.

Under certain conditions, it is possible for plastic waves to develop in sea ice models. In compact ice conditions, these waves can travel much more rapidly than the ice itself ($\sim 25\ \mathrm{m/s}$) (*Williams et al.*, 2017a). When using large time steps, these waves are badly represented and can cause a deterioration of the modeled fields. Combinations of resolutions and time steps which would fail a CFL test performed using the speed of a plastic wave instead of that of the ice itself are shown by hatching in Figs. 2.5, 2.6, 2.10 and 2.12. Coping with the increased numerical noise caused by the unresolved plastic waves presents an additional test for the solvers. Simulations with potential unresolved plastic waves were performed mostly to evaluate the robustness of the model when using larger time steps. With sufficiently small time steps, the plastic wave can be resolved without problems. It is also possible to avoid this problem by treating the ice strength implicitly (*Hutchings et al.*, 2004; *Lemieux et al.*, 2014). Evaluation of numerical efficiency is most relevant for combinations where the model is presented with a well resolved problem, outside the hatched area.

Using the analytical Jacobian as a preconditioner leads to an operator that is closer to $\mathbf{J}^{-1}$. This makes finding a solution to the linear problem much faster (see Fig. 2.6). The Jacobian preconditioner (Fig. 2.6, bottom row) improves the linear convergence of both methods, especially at high resolutions.

2.4.2 Global convergence

If the initial iterate $\mathbf{u}^0$ provided to Newton's method is too far from the solution for the solver to be in the local convergence phase, the iterative corrections may not improve the solution and the residual of the function may not decrease. This may be the case when encountering rapidly changing conditions, such as varying wind forcing or sea ice parameters.

2.4.2.1 Impact of the forcing change

In the oscillating case (Fig. 2.7), we observe that the number of iterations required before a reduction of the residual norm occurs increases with larger changes in the wind forcing. The solver initially fails to reduce the residual norm for a number of iterations, with peaks in number of iterations at hours 36, 72 and 108, corresponding to the half period of the wind oscillations and times of greatest changes in the winds. Compared to solvers using the Picard Preconditioner (top row), those using the Jacobian preconditioner (bottom row) performed poorly.

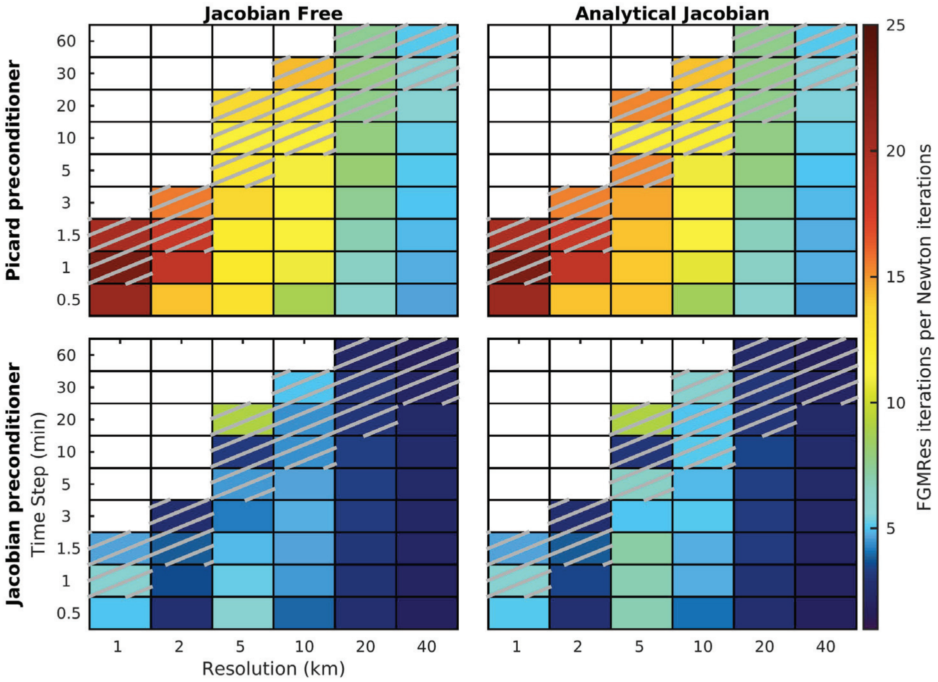

Figure 2.6: Average number of FGMRES iterations required to solve the linear problem using the JFNK-P (top left), AJNK-P (top right), JFNK-J (bottom left) and AJNK-J (bottom right). Hatching identifies the possibility of unresolved plastic wave in the ice.

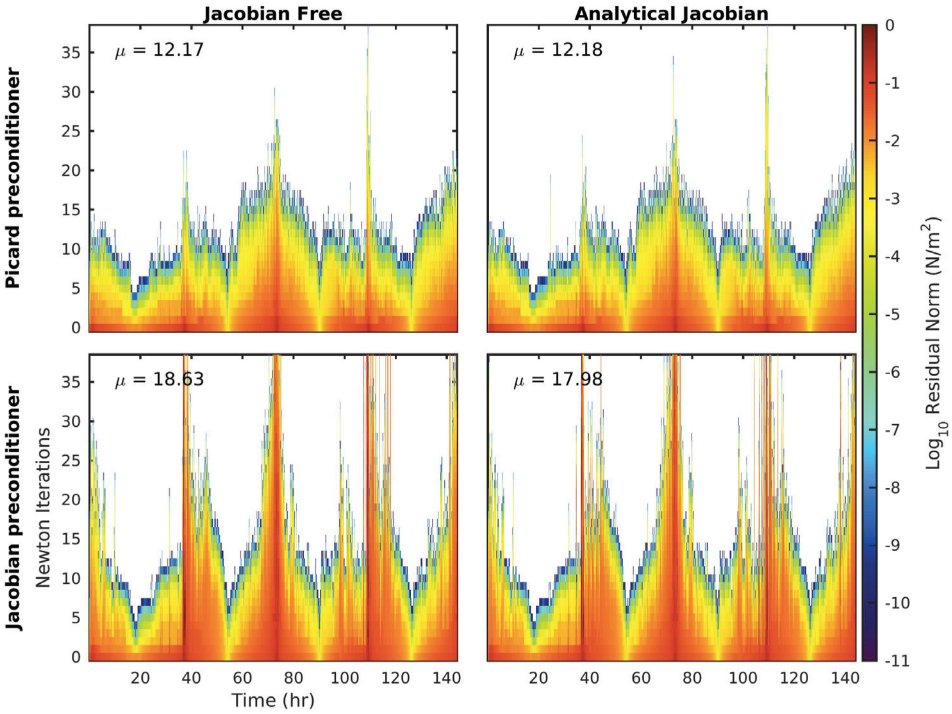

Figure 2.7: L2-norm of the nonlinear residual and average number of iterations to reach convergence, μ, when using oscillating uniform winds with Leads initial conditions, $\Delta x = 10\ \mathrm{km}$ and $\Delta t = 5\ \mathrm{min}$ and using the JFNK-P (top left), AJNK-P (top right), JFNK-J (bottom left) and AJNK-J (bottom right).

2.4.2.2 Impact of plastic waves

Aside from a rapidly changing forcing, the presence of plastic waves in the ice can also impair solver convergence. For example, in the simple case with Constant Uniform winds and Leads initial conditions, packing of the ice against a closed boundary causes noise to develop in the model after 100 hours, in the 100 km closest to the boundary where compression occurs. Even though it is unnoticeable in the velocity (Fig. 2.8, top left), the noise is visible as a marked wave-like feature in the bulk viscosity, ζ, (top right). The specific impact on ice velocities and thickness is dependent on the time step and resolution used in the model, with the oscillations creating artificial alternating periods of resistance and deformations in the ice instead of a smooth compression, however, this occurs in areas where the ice is deforming very slowly and thus impact on the accuracy of the simulations are minor. Numerically however, these oscillations require a higher order approximation to the Jacobian to be represented properly in the JFNK method, resulting in a poor approximation of the Jacobian-velocity product (bottom right). This, in turn, could lead to slower convergence of the solver to the desired solution accuracy and a more time consuming simulation. The analytical Jacobian-velocity product, by opposition, remains smooth (bottom left). It is important to note that both Jacobian-vector products presented here are calculated from the same experiment in which the time integration is performed using the AJNK solver and exact Jacobian preconditioner, so the discrepancy is due only in the way the approximation is calculated and not by drift between runs with different solvers.

The oscillations coincide with a slower convergence in the model runs performed using the Picard preconditioner (see Fig. 2.9, top row) compared to those using the Jacobian (bottom row). Provided that the amplitude of the oscillation and affected fraction of the domain remain small, there is less impact on runs performed with the Jacobian preconditioner. However, should the oscillation grow in amplitude or area, it will cause the model to eventually fail regardless of the method used.

As shown in this example case, the oscillation in ice parameters can often be invisible in the velocity fields, only becoming visible in divergence or viscosities (Fig. 2.8) which are more rarely looked at. Because of the smoothness of the velocity field, ice thickness and concentration are also not significantly affected. There can thus be cases where underlying

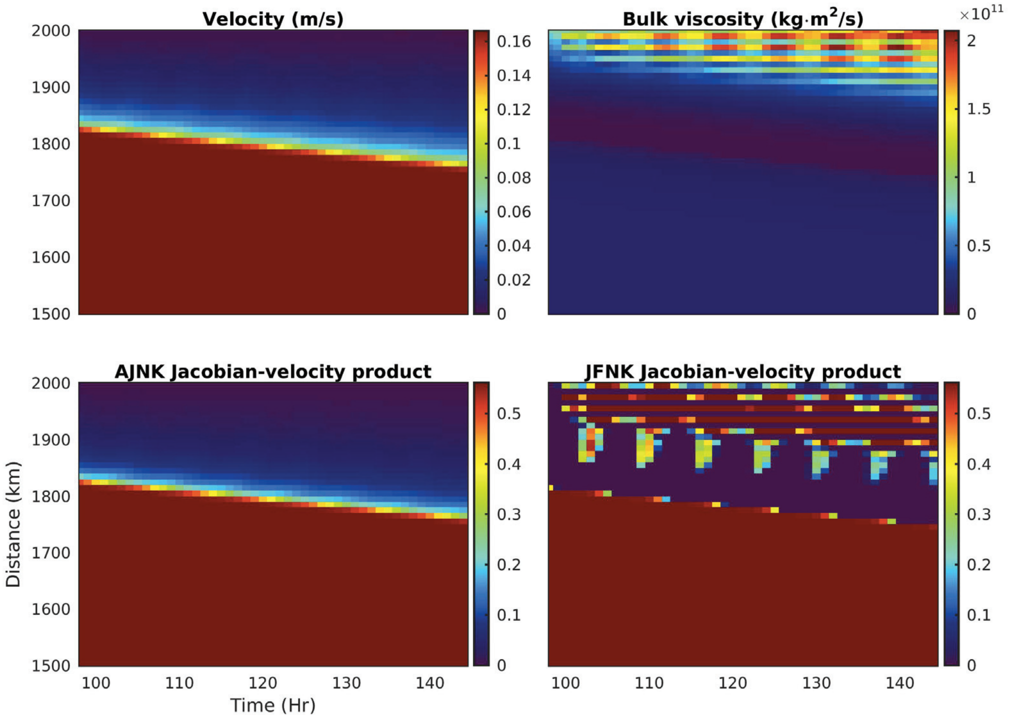

Figure 2.8: Velocity field (top left), bulk viscosity coefficient (top right), exact (bottom left) and approximated (bottom right) computation of the Jacobian-velocity product. All results, including both of the Jacobian-vector products, are from the same experiment with uniform, constant winds, 0.7 initial ice concentration, 10 minutes time step and 10 km resolution and time integration performed by the AJNK-J method.

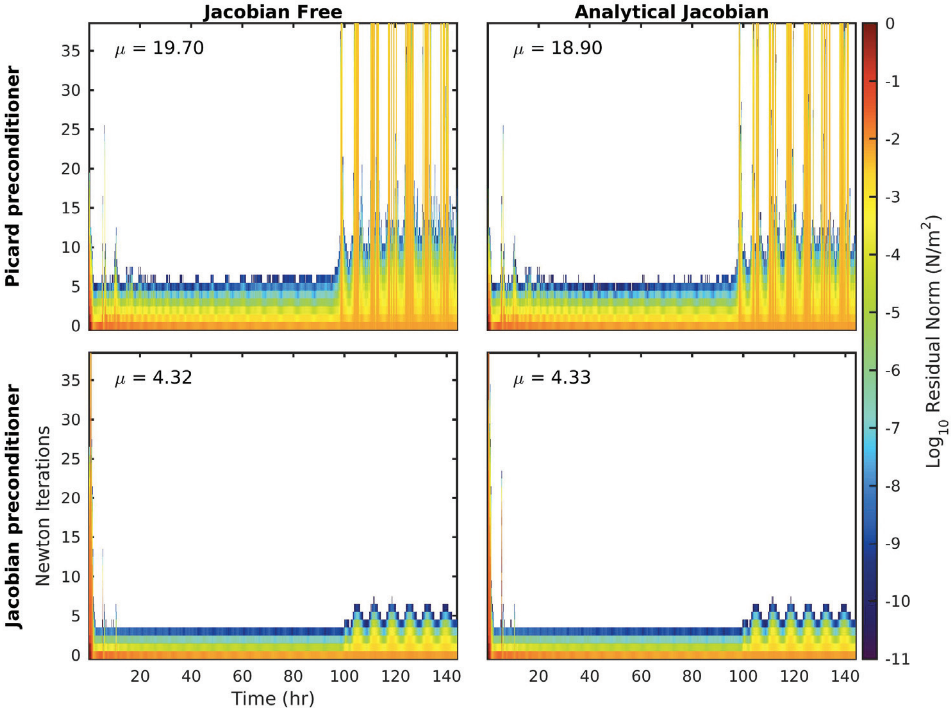

Figure 2.9: L2-norm of the nonlinear residual and average number of iterations to reach convergence, μ, when using constant uniform winds with Leads initial conditions, $\Delta x = 10\ \mathrm{km}$ and $\Delta t = 10\ \mathrm{min}$ and using the JFNK-P (top left), AJNK-P (top right), JFNK-J (bottom left) and AJNK-J (bottom right) methods.

physical parameters and solver efficiency may both be compromised without it necessarily being apparent under routine inspection of the results.

2.4.2.3 General solver stability

Certain initial iterates do not enable the Newton solver to enter the local convergence phase or to reduce the residual by the required amount before the maximum number of iterations (150) is reached. This is considered a failure to converge and the solution at that time step may not be an appropriate approximation of the exact solution. When averaged over combinations of initial conditions and wind forcings, the AJNK solver (Fig. 2.10, right column) generally fails less often than the JFNK solver (Fig. 2.10, left column) for a given preconditioner, especially at higher resolutions ($\Delta x \leq 2\ \mathrm{km}$). This is most visible while using the Picard preconditioner (top row) as it also reduces the number of failures compared to the Jacobian preconditioner (bottom row).

Certain combinations of forcing and initial conditions are more challenging for the model and require a large number of Newton iterations in order to reach the convergence criterion. For a given time step, the Newton solver fails increasingly in challenging cases as resolution is increased (Fig. 2.10). Given that failed runs are not considered in averages of iterations, this explains the apparent reduction in the number of iterations at higher (1-2 km) resolutions that was observed (Fig. 2.5): Cases that were challenging at low resolutions, those for which model runs were contributing large numbers of iterations to the average, instead failed at higher resolutions and were no longer considered when computing the average.

Newton's method is generally more likely to find a solution with the Picard preconditioner, even though using this preconditioner makes overall convergence slower. Additionally, if FGMRES fails, the linear solution it returns to be used in Newton's method may not be adequate for the Newton iteration to reduce the nonlinear residual which, in turn, can cause the nonlinear solver to fail as well. Averaging over all time steps, resolutions and spatial wind conditions, it can be seen that certain wind temporal patterns and initial conditions are also more likely to cause failures of the Newton solver (see Fig. 2.11).

With strong ice fields (the Solid or Slab cases), constant or oscillating winds may create

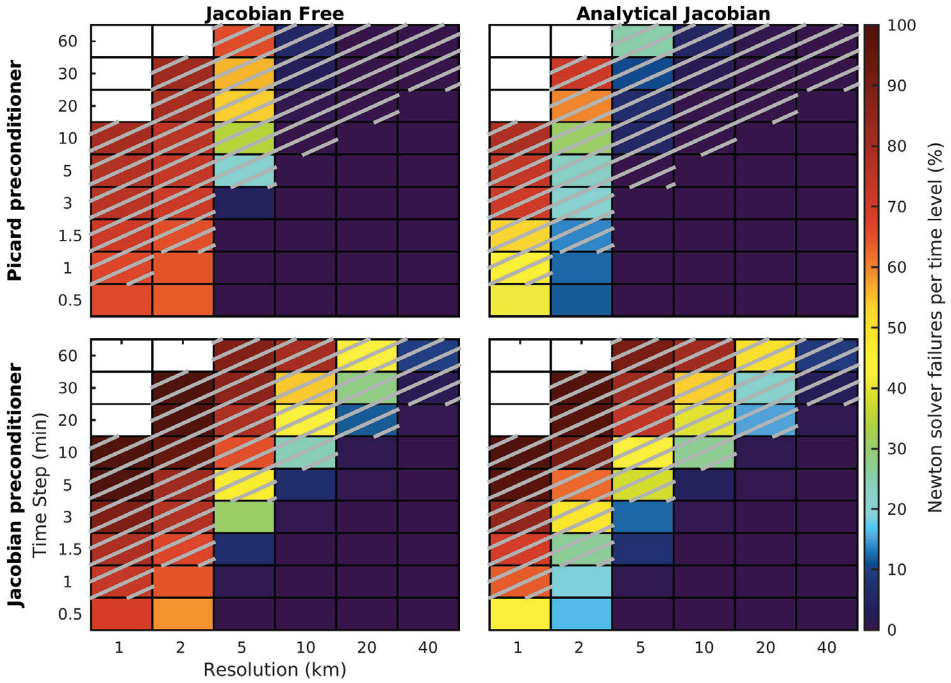

Figure 2.10: Average percentage over all considered cases of time levels failing to achieve convergence with the maximum number of iterations when using the JFNK-P (top left), AJNK-P (top right), JFNK-J (bottom left) and AJNK-J (bottom right) methods. Hatching identifies the possibility of unresolved plastic wave in the ice.

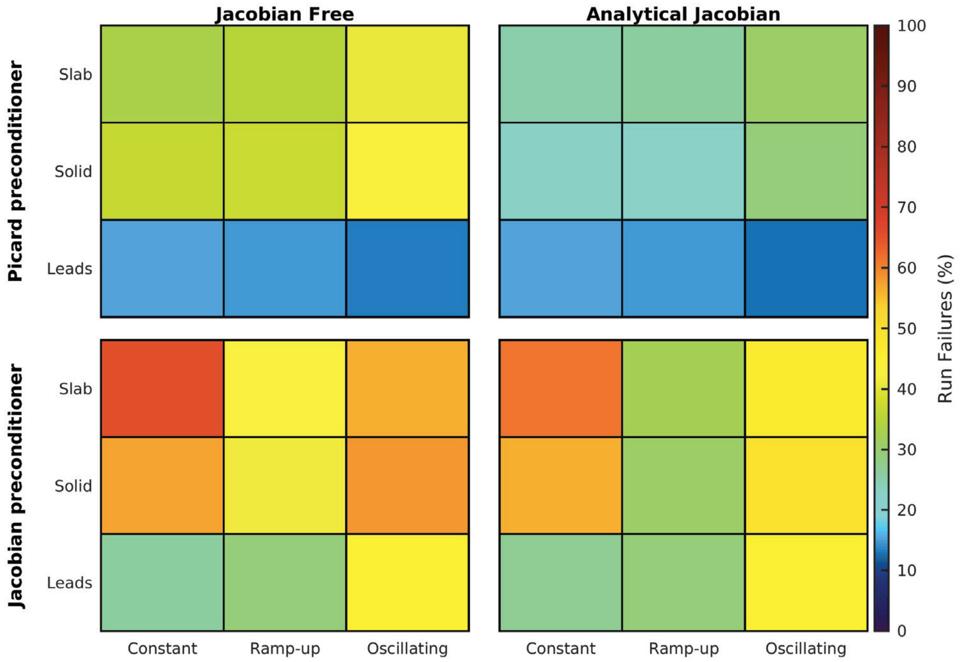

Figure 2.11: Percentage of cases with more than 5% Newton solver failures for each wind temporal variability and initial conditions pair, averaged over all combinations of time steps, resolutions and wind spatial variability.

either noisy conditions or large changes in the solution respectively, if the time step used is too large. When this happens, the initial iterate may be too far from the solution, leading to a failure of Newton's method.

However, weak ice in the 'Leads' reduces the importance of the rheology term because of the exponential dependence of ice strength on concentration described in Eq. 2.8. This makes the problems easier and solvers are, unsurprisingly, more reliable for all wind conditions. Similarly, slowly increasing the wind forcing at the beginning of the model run in the 'Ramp Up' time evolution of wind forcings eases up the mobilization of ice and reduces failure rates by reducing the discrepancy between the winds and the initially stationary ice.

2.5 Discussion and conclusion

In this chapter, the potential of further developing the use of Newton's method to solve the sea ice momentum equation as described in *Lemieux et al.* (2010) was demonstrated. The main contributions of this chapter are: 1 - the derivation of the analytical Jacobian of the sea ice momentum equation, 2 - a thorough comparison between the JFNK and the new AJNK solver used with different preconditioning matrices and 3 - the introduction of a hybrid preconditioner with the AJNK method which combines the robustness of the original JFNK solver and the numerical efficiency of the AJNK solver with a Jacobian preconditioner.

When provided with a sufficiently accurate initial iterate, Newton's method with an analytical Jacobian is more efficient than an implementation using an approximated Jacobian, which itself was more efficient than the Picard solver, the previously used implicit solver *Lemieux et al.* (2010). Indeed, the use of the analytical Jacobian allows faster convergence to the solution (Fig. 2.5) and requires fewer iterations of FGMRES in order to solve the linear problem it poses (Fig. 2.6) than the JFNK method with an approximation to the Jacobian as a preconditioner. The reduction in both Newton and FGMRES iterations is compounding and can offer significant reduction in computational costs. Furthermore, having the analytical Jacobian greatly simplifies computations of the Jacobian-vector product required by FGMRES compared to a finite difference approximation of the product such as Eq. 2.17. Although this has no impact on the number of iterations, it is a tangible reduction in numerical effort.

Of the two changes presented here, using the Jacobian preconditioner yields the greatest benefits in terms of model efficiency. It reduces the number of iterations for FGMRES by a factor of up to 5 at high resolutions. Although the effect of using the AJNK method on number of iterations for either Newton's method or FGMRES is much smaller, it is beneficial to use the AJNK-J method at high resolutions.

Because of the increased efficiency of the Jacobian preconditioner, FGMRES may solve the linear problem highly accurately on its final iteration. The increase in accuracy gives a solver that performs similarly to an exact Newton method. While this may seem to be advantageous at first, an exact implementation of the method can be less robust than an inexact version obtained by solving the linear problem less accurately (*Eisenstat and Walker*, 1996). Indeed we observe an increase in failures when using the Jacobian preconditioner for time steps which are close to the maximum time step allowed under an advective CFL condition (Fig. 2.10).

In view of this trade-off between efficiency and reliability, special consideration should be given to the choice of the method and the parameters. Increased efficiency offers gains in accuracy when under time constraints, such as when issuing forecasts. The computing time saved can be highly valuable and in turn opens up the possibility of decreasing time steps which improves model stability. In the cases considered here, the risks of solver failures are significant mainly for conditions (forcing, resolution and time step combinations) which should be avoided regardless of the solver used. Under these conditions, the solution, if obtained by the more robust solver, is indeed often corrupted by unresolved plastic waves or a disconnection with winds that are changing more rapidly than the model can capture. Thus, we believe that the benefits offered by more advanced methods outweigh the risks.

In order to combine the increased efficiency of the exact Jacobian with the robustness of the Picard preconditioner, a hybrid preconditioner was also implemented. This preconditioner uses the Picard matrix until the nonlinear residual has dropped below a value deemed to mark the beginning of the local convergence phase (here taken to be $\frac{2}{3}||\mathbf{F}(\mathbf{u}^0)||$, the same threshold as used in *Lemieux et al.* (2014)), then uses the analytical Jacobian as a preconditioner to benefit from the improved convergence rate.

As shown in Fig. 2.12, the hybrid preconditioner allows the AJNK method to benefit from both the reduced average number of iterations provided by the analytical Jacobian once in the local convergence phase (top row, compared to Figs. 2.5 and 2.6), even at high resolutions, as well as the increased reliability exhibited by solvers when using the Picard preconditioner (bottom row, compared to Figs. 2.10 and 2.11).

All of the work presented here has been done using a 1D model of sea ice dynamics. This was done to simplify both the derivation of the analytical Jacobian and the completion

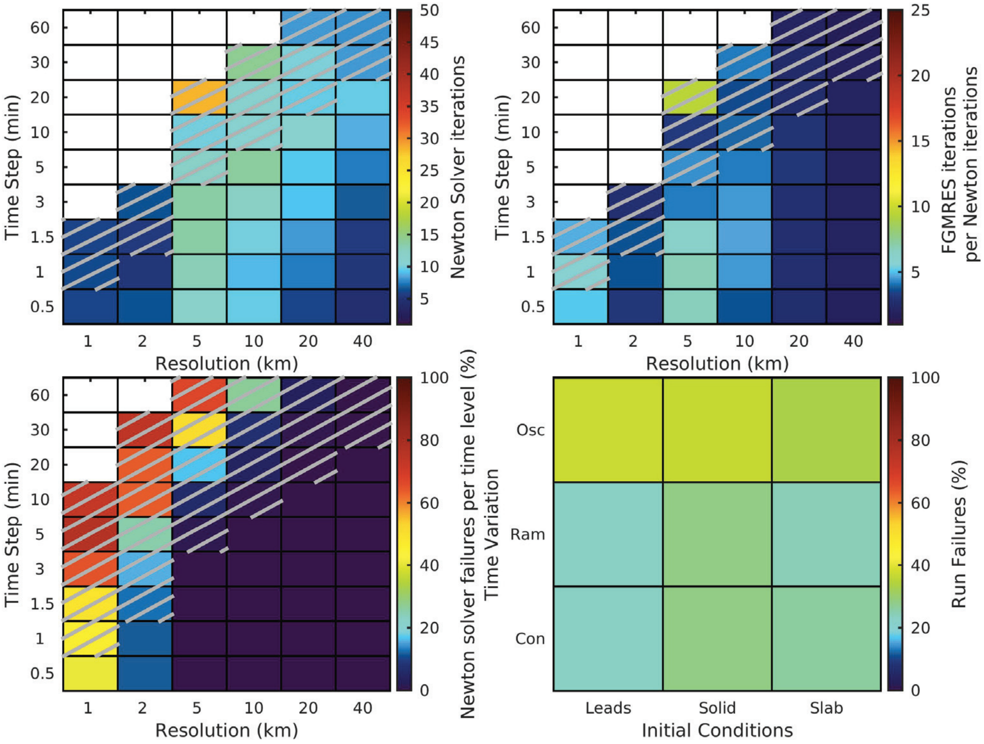

Figure 2.12: Average numeric results obtained using the analytical Jacobian Newton solver with hybrid preconditioner: Newton iterations required for convergence (top left), FGMRES iterations required for convergence (top right), percentage of Newton failures (bottom left). Hatching identifies the possibility of unresolved plastic wave in the ice. Percentage of runs with more than 5% Newton solver failures. (bottom right).

of the numerical simulations required for the experiments. It is possible to create higher order numerical schemes than were used here (such as the second-order accurate in time scheme of *Lemieux et al.* (2014)) but we kept lower order schemes for the same reason. Using higher order schemes may change the stability conditions or convergence, through a strengthening of gradients for example.

Creating a solver that combines reliability and efficiency remains a challenge with such a highly nonlinear problem as sea ice dynamics. Compared to the reference Picard preconditioner, the hybrid preconditioner offers improvements to the numerical efficiency with a minimal impact on the robustness. Exact computation of the Jacobian-vector product has improved solver robustness over the JFNK approach, however it remains an issue particularly at high resolution. Future work will address this problem.

This 1D model is a simplification of the entire dynamics of 2D models. However, it includes a significant portion of the rheology term which is numerically the most challenging. The results obtained here therefore provide guidance for the 2D models. It is to be noted that, because of the presence of shear, the problem of the splitting in time instability, or the plastic waves, is less important in 2D than in 1D. This is encouraging for an implementation of the method presented here in a full 2D model where the complexity of the problem would benefit from the increased efficiency of the AJNK method and analytical Jacobian or Hybrid preconditioners, whereas the main challenge of robustness should be less of a problem. The implementation of the AJNK in in a parallel 2D model based on latitude-longitude grids was not pursued in this thesis due to the technical complexity involved and because the focus of this thesis is on studying the MIZ where the available 1D format was sufficient. Complete implementation in a 2D model fit for operations remains highly desirable however.

CHAPTER 3

DYNAMICAL MODELING OF SEA ICE AND WAVE ENERGY FOR THE MARGINAL ICE ZONE

While the attenuation of surface gravity waves by sea ice can be simulated in some numerical wave models, the impact of waves on ice is not considered, however, in most ice models, and coupled models with all the interactions are fairly rare. However, large surface waves coming from the open ocean can affect the ice over vast distances (*Dumont et al.*, 2011). Waves can also provide a positive feedback to support the growth of polynyas (*Wadhams*, 1983). Waves can break-up large floes into smaller, more mobile, ones (e.g. *Dumont et al.* (2011), *Herman* (2018)), making the ice pack weaker when subjected to shear or compression. In this study, the one-dimensional sea ice model presented in chapter 2 is modified to incorporate waves and their interactions with ice.

Scattering and dissipation based parameterizations for the wave attenuation proposed by *Kohout and Meylan* (2008) and *Sutherland et al.* (2019), respectively, are implemented in the 1D model. As waves attenuate, the excess flow of momentum that they carry, also known has the radiation stress, varies in space, and time, and a force is applied to the ice (*Longuet-Higgins and Stewart*, 1964). *Sutherland and Dumont* (2018), using simultaneous in situ measurements of wave attenuation and ice thickness across the marginal ice zone in the St. Lawrence Estuary, Canada, were able to show that the radiation stress can be strong enough to thicken the ice through compression over distances that depend on the incident wave energy and the wave attenuation rate. In order to reproduce this wave driven ice compaction, the wave radiation stress along with different wave attenuation and ice strength formulations are used to investigate the possible impact of this new wave stress on ice. In section 3.1, the model used is described. Section 3.2 presents the case study on the variation of attenuation and ice strength while section 3.3 presents the results, which are then discussed in section 3.4.

3.1 Model description

The model used for this study is the one-dimensional (1D) sea ice model described in chapter 2, modified to add wave energy propagation and attenuation within the model as well as the force applied by the waves on sea ice (τ_{wvx} in Fig. 1.6). Both the wave and the sea ice components of the model operate with the same time step. This significantly decreases the possible time step of the model due to the high velocity of the waves, leading to a CFL restriction on the time step reducing it by a factor of 10 for a given resolution. This shared time step ensures that waves and ice evolve in unison. It also has the advantage of improving the quality of the initial guess provided to the implicit solver used for the sea ice velocities and helping convergence.

3.1.1 Sea Ice Component

In order to couple the sea ice component of the model, the wave radiation stress term (τ_{wv}) is added to the 1D momentum equation (Eq. 2.1):

$$\rho h \frac{\partial u}{\partial t} = \tau_a + \tau_{wv} - \tau_w + \frac{\partial \sigma}{\partial x}. \tag{3.1}$$

This new term represents the force exerted by the horizontal momentum absorbed or reflected when waves hit and propagate in sea ice. This can represent a significant forcing in the marginal ice zone, as demonstrated by *Sutherland and Dumont* (2018). As derived in *Sutherland and Dumont* (2018), for a given wave frequency f, the radiation stress per unit frequency exerted by a wave spectrum ($E_{wv}(f)$) on the ice perpendicularly to wave propagation ($\tilde{\tau}_{wv}(f)$) is defined as

$$\tilde{\tau}_{wv}(f) = -\rho_w g \frac{\partial}{\partial x} \left[E_{wv}(f) \left(2\frac{c_g(f)}{c_p(f)} - \frac{1}{2} \right) \right] \tag{3.2}$$

where c_p and c_g are the phase and group velocities of the waves (see section 3.1.2 for details), respectively, and ρ_w is the seawater density (*Sutherland and Dumont*, 2018).

Integrating Eq. 3.2 over all the frequencies gives the total wave radiative stress exerted on the ice:

$$\tau_{wv} = \int_0^\infty \tilde{\tau}_{wv}(f)\, df \tag{3.3}$$

or, for a discretized wave spectrum:

$$\tau_{wv} = \sum_{f_0}^{f_n} \tilde{\tau}_{wv} \Delta f \tag{3.4}$$

In addition to the added force due to waves, the MIZ also tends to have different ice characteristics. Here, sea ice is usually fragmented in small pieces (floes) that heave, tilt and surge in response to waves and ice thickens homogeneously as a result of floe rafting and brash convergence instead of breaking at localized ridging lines(*Sutherland and Dumont*, 2018). For such cases, a Mohr-Coulomb formulation developed for river ice jumbles (*Uzuner and Kennedy*, 1976) can provide an appropriate description of the marginal ice zone dynamics. *Sutherland and Dumont* (2018) obtained good agreement between ice thickness profiles calculated from the equilibrium between the Mohr-Coulomb ice strength and wave radiation stress and in situ measurement of ice thickness compressed by waves in a marginal ice zone of the St. Lawrence Estuary.

In the Mohr-Coulomb model, the horizontal force per unit length that is necessary to compress ice of thickness h, the ice compressive strength (P_p, hence P_{MC} for the Mohr-Coulomb formulation) represents the work against gravity and buoyancy required to increase the ice thickness through both ridging and rafting as opposed to the ice's material strength. Using this model, *Dai et al.* (2004) define the ice strength as:

$$P_{\mathrm{MC}} = K_r h^2, \tag{3.5}$$

with

$$K_r = \frac{\rho g}{2}\left(1 - \frac{\rho}{\rho_w}\right)(1-n)\left(\frac{1+\sin\phi}{1-\sin\phi}\right), \tag{3.6}$$

where n is the ice porosity and ϕ is the internal friction angle. It is notable here that the compressive strength has a quadratic dependence on h instead of a linear dependence in the ice strength as defined by *Hibler III* (1979), P_p in Eq. 2.8 (now referred to as P_{Hibler}), to represent compact ice conditions of the inner ice pack in large scale ice models. However, the quadratic model may predict unreasonably large compressive strength for thicker ice. In order to blend the two formulations in a way that allows our model to apply in a broad range of thickness values, a hybrid strength (P_{Hybrid}) with an additional dependence on thickness added to Eq. 2.8 is suggested, defined by:

$$P_{\text{Hybrid}} = P^{*} h \tanh{(\gamma h)} \exp[-C(1-A)], \tag{3.7}$$

where γ is an adjustable parameter that controls the transition between the two regimes. Figure 3.1 shows the thickness dependence of the two compressive strength formulations as well as the hybrid formulation with two values of γ, $1/2$ and $1/4$. For P_{Hibler}, a typical P^{*} value of 27.5 kPa was chosen for the curve, with the shaded area representing the range of values from the literature from 10.8 to 48.8 kPa. For P_{MC}, typical values of $n = 0.4$ and $\phi = 34^{o}$ were chosen for the curve and the shaded area represent the range from porous, easy to stack ice with $n = 0.5$ and $\phi = 26^{o}$ to denser ice with $n = 0.5$ and $\phi = 58^{o}$. The hybrid ice strength defined in Eq.3.7 was chosen so that it can represent both types of ice: broken ice best represented by the Mohr-Coulomb rheology at low thickness and the inner ice pack represented by the Viscous-Plastic rheology. At low thickness, the hybrid formulation is weaker for low thickness, with a strength that increases quadratically much like the Mohr-Coulomb rheology. As ice thickness increases, the extra $\tanh$ dependence approaches one and the ice strength becomes linear, approaching the P_{Hibler} values. Using this formulation, it is possible to represent the two failure types in sea ice.

3.1.2 Wave Component

Surface gravity waves, defined as a frequency dependent spectrum at the boundary, can be propagated inside the domain using a one-dimensional version of Eq. 1.1, with the wave action spectrum (N) reverted back to the energy spectrum (E) since the ocean is considered to be at rest. At each time step, the wave energy spectrum, E_{wv}, is evolved through advection and attenuation by the sea ice (S_{ice}):

$$\frac{\partial E_{wv}}{\partial t} + c_g \frac{\partial E_{wv}}{\partial x} = S_{\text{ice}} \tag{3.8}$$

Energy advection is done using the group velocity ($c_g = \frac{\partial \omega}{\partial k}$) calculated for each

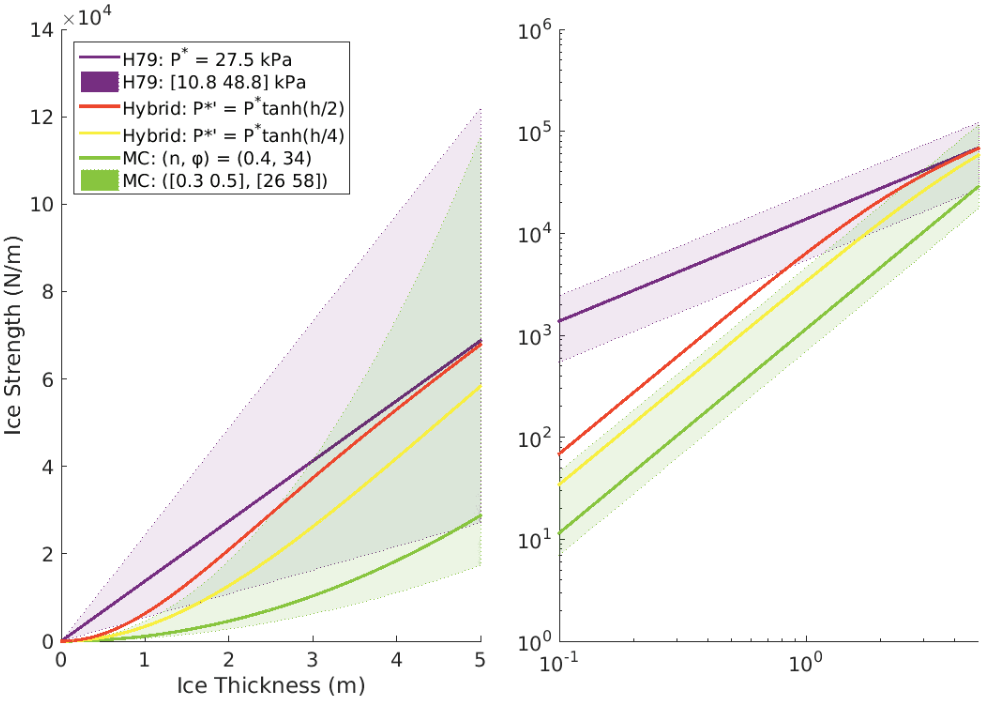

Figure 3.1: Compressive strength as a function of ice thickness in linear (left) and log (right) scales. P_{Hibler} (Eq. 2.8, purple), P_{MC} (Eq. 3.5, green) and P_{Hybrid} (Eq. 3.7, red and yellow) formulations. Shaded areas represent the range of possible values found in the literature.

frequency bin and location, using the ice thickness at that location. As we are considering the very edge of the ice, where floes tend be smaller than the peak wavelength, the mass loading wave dispersion relation (e.g. *Liu and Mollo-Christensen* (1988)) is used:

$$\omega^2 = gk \left[\frac{\rho}{\rho_w} kh + \coth(kd) \right]^{-1}. \tag{3.9}$$

Since the aim of the model is to study the ice interaction with specified spectra, the wave energy spectrum does not change in open waters.

3.1.2.1 Wave attenuation

Wave energy is attenuated by the presence of ice. The specific mechanism through which this happens remains to be identified and it is likely that multiple ones are at play. As described in section 1.1.2, this attenuation takes the form of an exponential decay with distance traveled in ice. This is represented through the ice interaction source term, S_{ice}, in the energy advection-attenuation balance:

$$\frac{DE_{wv}}{Dt} = S_{\text{ice}} = -\beta(A, h, f)E_{wv}. \tag{3.10}$$

where β is the temporal attenuation coefficient (s^{-1}). The spatial attenuation coefficient, (α, m^{-1}) can be related to β using:

$$\beta = \alpha c_g. \tag{3.11}$$

The attenuation coefficients depend on the attenuation models considered. In this study, we are contrasting two different models that are representative of the two main processes used to explain wave attenuation: wave scattering and wave dissipation. In the *Kohout and Meylan* (2008) model, simulations of wave scattering as they encounter ice floes were performed for a range of thicknesses and frequencies in order to evaluate the average attenuation per floe, a. This rate can be converted to an attenuation rate per unit distance using $\alpha = Aa/D$ where A is the concentration and D is the floe diameter. Since the 1D model used in this study does not directly simulate floe size and given the requirement for large floe sizes for the calculation of the attenuation coefficient, a fixed floe size of 10 m was used. This is then converted to the temporal attenuation rate, β, using Eq. 3.11 and used in Eq. 3.10.

In the model suggested by *Sutherland et al.* (2019), the ice is represented as a two-layer material, with a permeable lower layer of thickness ϵh where viscosity damps down the wave motion and an upper impermeable layer of thickness $(1-\epsilon)h$. Solving the fluid motion in the permeable layer and water underneath, the temporal attenuation coefficient for this two-layer model is defined as:

$$\beta = \frac{\nu\omega^2\Delta_0}{g\epsilon h}. \tag{3.12}$$

where Δ_0 represents the wave motion amplitude variation with depth and phase shift and

$$\nu = \frac{1}{2}\epsilon^2\omega h^2. \tag{3.13}$$

Combining the two, we obtain the temporal attenuation coefficient used in Eq. 3.10 as a function of frequency and thickness:

$$\beta = \frac{\epsilon\Delta_0 h\omega^3}{2g} \tag{3.14}$$

with two free parameters that need to be evaluated: ϵ, the fraction of ice that is permeable, and Δ_0, both of which are between 0 and 1.

In order to find a value of the parameter pair, the spatial attenuation function from the two-layer model:

$$\alpha = \frac{1}{2}\Delta_0\epsilon h k^2 \tag{3.15}$$

was fit to observations of wave attenuation coefficient (α) as a function of wave number from *Baudry et al.* (2021), shown in Fig. 3.2. This data was obtained over multiple days during the field study of *Sutherland and Dumont* (2018), using wave buoys deployed on the ice and underwater pressure sensors. In ice of 0.7 m thickness, a value of 0.5 was found for the free parameter pair $\Delta_0\epsilon$. Using the fitted values, the attenuation based on *Sutherland et al.* (2019) depends exclusively on sea ice thickness and wave characteristics.

The attenuation obtained from *Kohout and Meylan* (2008) is generally weaker than that calculated using the fitted coefficient from *Sutherland et al.* (2019), as shown in Fig. 3.3. The most important difference between the two attenuation schemes is at low frequencies

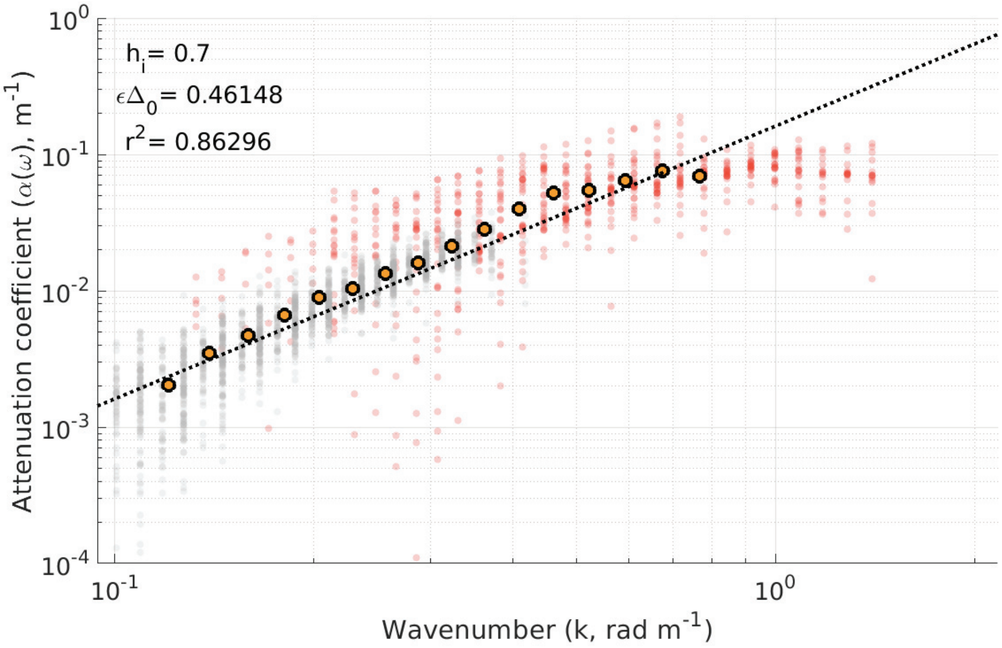

Figure 3.2: Wave attenuation coefficients (α) as a function of wavenumber for ice of 0.7 m thickness. Measurements were taken from buoys deployed on the ice (grey) and an underwater pressure sensor (red). Circles are bin averages of the measurements.

and small thicknesses, where smaller values from the *Kohout and Meylan* (2008) values allow the lower frequency waves to penetrate the ice further, until a greater thickness is encountered. By opposition, the difference in attenuation coefficients at high frequency and large thickness is less meaningful since, in a typical thickness profile increasing from the ice edge to the shore, high frequency waves will have been attenuated by thinner ice before encountering the thick ice.

3.1.3 Numerical Scheme

A backward Euler scheme analogous to the one in Eq. 2.11 is used for the sea ice momentum equation. Once the ice velocity solution is found, advection of ice thickness, concentration and wave energy along with the attenuation of wave energy attenuation are performed to complete the time-step. The continuity equations of the ice thickness and the ice concentration as well as the wave advection and attenuation equations are solved explicitly with a forward Euler scheme.

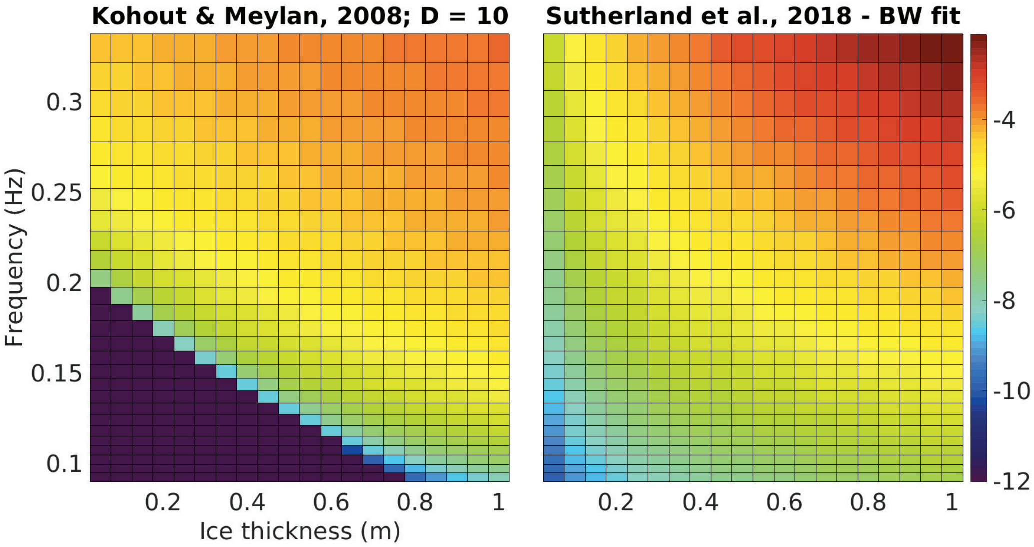

Figure 3.3: Wave attenuation ($log_{10}(\alpha)$, α in m^{-1}) as a function of wave frequency and ice thickness for the two wave attenuation formulations considered: The scattering based attenuation by *Kohout and Meylan* (2008) calculated for floes of 10m diameter (left) and the two-layer wave dissipation formulation by *Sutherland et al.* (2019) fitted as presented in Fig. 3.2 (right).

The time-discretized sea ice momentum equation in 1D is written as

$$\rho h^{n-1}\frac{(u^n - u^{n-1})}{\Delta t} = \tau_a^n + \tau_w^n - \tau_{wv}^n + \frac{\partial \sigma^n}{\partial x}, \tag{3.16}$$

where the superscript n denotes the current time level, and $n-1$ is the previous, known, time level. We use a one-thickness category model. Eq. 3.16 is solved using a Jacobian free version of Newton's method. At every iteration of Newton's method, the dispersion relation Eq. 3.9 for waves in sea ice is solved for every frequency and location. The wave energy is then advected and attenuated using Eq. 3.8 and the energy gradient is used to calculate the wave stress (Eq. 3.4) on the ice. With all the stresses, the ice velocity u^n is found by the implicit solver. The continuity equations for both concentration and thickness are then solved explicitly:

$$\frac{(h^n - h^{n-1})}{\Delta t} + \frac{\partial}{\partial x}(u^n h^{n-1}) = 0, \tag{3.17}$$

$$\frac{(A^n - A^{n-1})}{\Delta t} + \frac{\partial}{\partial x}(u^n A^{n-1}) = 0. \tag{3.18}$$

Spatially, the model uses a staggered grid where ice concentration, thickness and wave energy are collocated and both ice and wave velocities are defined in between tracer points, in a 1D version of the Arakawa C-grid *Arakawa and Lamb* (1977). The model has one closed boundary where homogeneous Dirichlet boundary conditions are applied ($u = 0$) towards which the wind and waves push the ice. The other boundary is open, with constant wave forcing and open waters. Spatial derivatives are discretized using a second-order centered difference scheme. For a number of tracer points nx, the discretization of the momentum equation creates a system of $nx + 1$ equations.

Waves and all the associated variables are defined in the model at ice tracer points. At every time level, wave properties are calculated from the newly advected ice properties. Because of the difference in time scale between advection and attenuation in the problem, the wave energy is advected first, then attenuated. Advection is performed using a Lax-Wendroff scheme (*Lax and Wendroff*, 1960) with Superbee flux limiter (*Sweby*, 1984). First, the energy difference between neighbouring grid cells is calculated. Using these differences, two parameters are calculated:

$$\theta_{\mathrm{LW}}(x,f) = \frac{E(x,f) - E(x-\Delta x,f)}{E(x+\Delta x,f) - E(x,f)} \tag{3.19}$$

and

$$\phi(x,f) = \begin{cases} 0 & \theta_{\mathrm{LW}}(x,f) \leq 0 \\ 2\theta_{\mathrm{LW}}(x,f) & 0 < \theta_{\mathrm{LW}}(x,f) \leq 0.5 \\ 1 & 0.5 < \theta_{\mathrm{LW}}(x,f) \leq 1 \\ \theta_{\mathrm{LW}}(x,f) & 1 < \theta_{\mathrm{LW}}(x,f). \end{cases} \tag{3.20}$$

Using these two parameters, the flux defined as:

$$F(x,f) = E(x,f) + \frac{\phi(x,f)}{2}\left(1 - c_g(x,f)\frac{\Delta t}{\Delta x}\right)\left(E(x+\Delta x,f) - E(x,f)\right). \tag{3.21}$$

With the fluxes calculated, the advected energy is calculated

$$E_{adv}^{n+1}(x, f) = E^n(x, f) - c_g(x, f)\frac{\Delta t}{\Delta x}(F(x, f) - F(x - \Delta x, f)). \tag{3.22}$$

The attenuation of waves due to the ice is calculated on the advected energy (E_{adv}^{n+1}) using either of the temporal attenuation coefficients defined in 3.1.2.1 in an analytic solution to the wave attenuation equation:

$$E^{n+1}(x, f) = E_{adv}^{n+1}(x, f)e^{-\beta(x,f)\Delta t}. \tag{3.23}$$

3.2 Case study

In order to test the model described above, simulations were performed using a 250 m resolution and 5 s time step, subjecting an initially uniform 70% concentration and 10 cm thick ice cover to 10 $\mathrm{m/s}$ winds. Fully developed waves initially at equilibrium with the winds are generated at the boundary using a corresponding JONWSAP spectrum (*Pierson and Moskowitz*, 1964). Parameters such as peak frequency (f_p) and significant wave height (H_s) are first calculated depending on the wind speed then the energy spectrum ($E(f)$) is generated (*Bouws et al.*, 1998). Fig. 3.4 shows such a spectrum as used for the case study presented below.

The reference, P_{Hibler}, ice strength was used along with two versions of the hybrid (P_{Hybrid}) formulations 3.7, with ratios γ of $1/2$ and $1/4$. Wave attenuation was calculated using either *Kohout and Meylan* (2008) or *Sutherland et al.* (2019), as described above. Results over the course of simulations are presented as in chapter 2 and as was described in Fig. 2.1b.

Attenuation in both parameterizations occurs mostly near the ice edge (Fig. 3.5). The main difference is stronger attenuation even in thin ice in the formulation by *Sutherland et al.* (2019). This strong local energy gradient applies a larger force at the ice edge following Eq. 3.2.

The sea ice thickness evolution shows the large impact of using the hybrid formulation

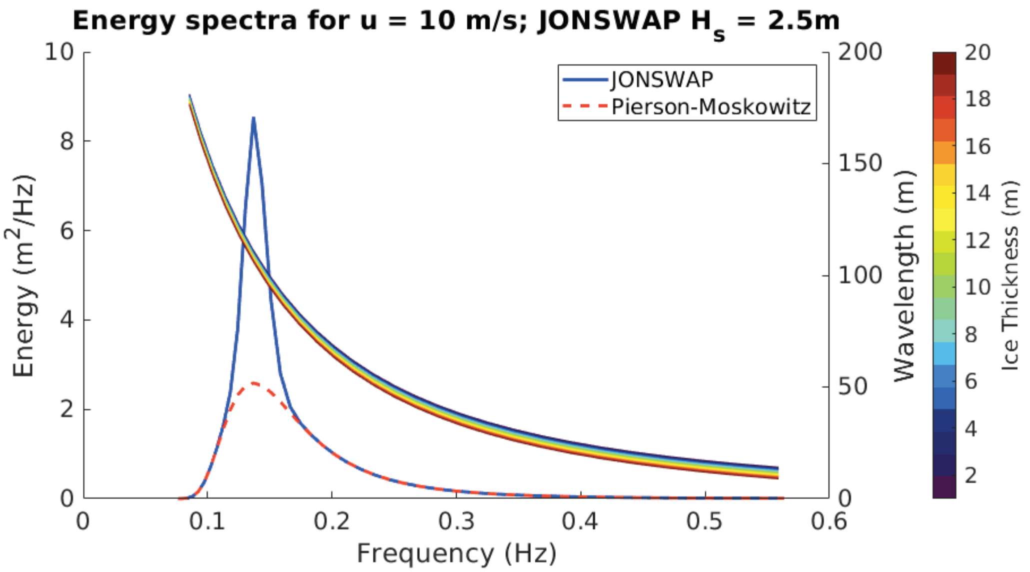

Figure 3.4: Pierson-Moskowitz (red, dashed) and JONSWAP (blue, solid) wave energy spectra for 10 $\mathrm{m/s}$ winds, along with the wavelength associated with each frequency for a range of ice thicknesses (colors).

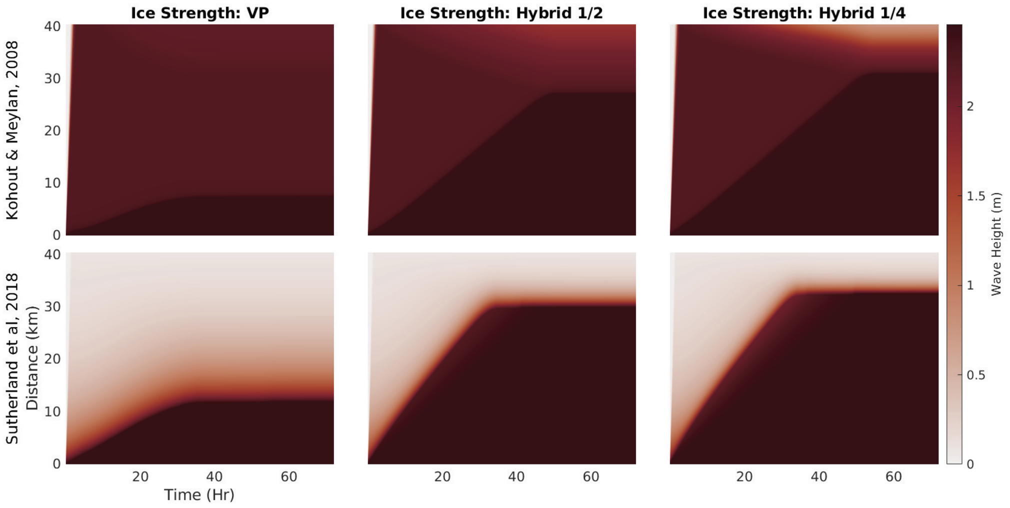

Figure 3.5: Significant wave height (H_s) modeled using the original VP ice strength (left), the hybrid ice strength with $\gamma = 1/2$ (middle), or $\gamma = 1/4$ (right), using the attenuation formulations suggested by *Kohout and Meylan* (2008) (top) or *Sutherland et al.* (2019) (bottom).

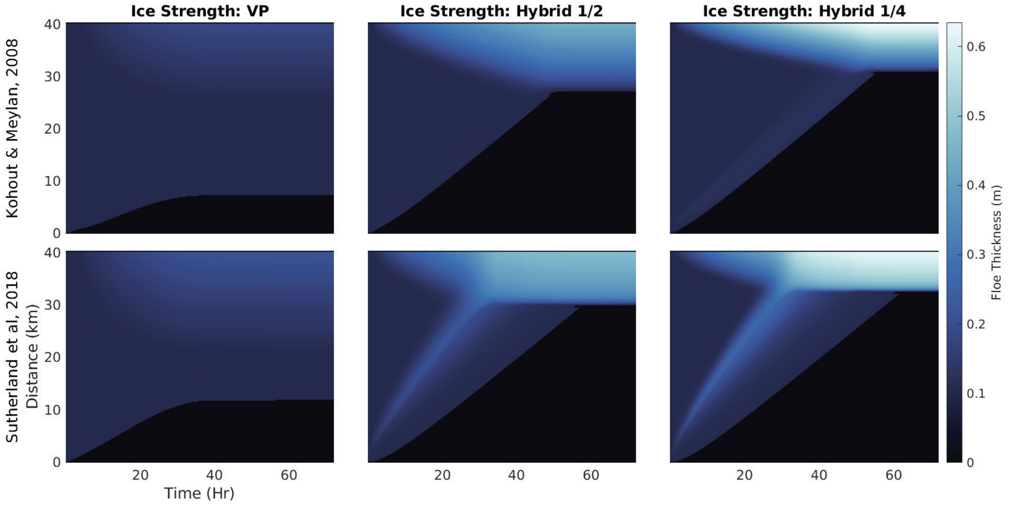

Figure 3.6: Ice thickness using the original VP ice strength (left), the hybrid ice strength with $\gamma = 1/2$ (middle), or $\gamma = 1/4$ (right), using the attenuation formulations suggested by *Kohout and Meylan* (2008) (top) or *Sutherland et al.* (2019) (bottom).

when dealing with thin ice. Ice edge movement and final thickness obtained using both of the γ factors are noticeably different from the results from the VP simulations using P_{Hibler} (Fig. 3.6), regardless of the attenuation function used.

Between the two wave attenuation parameterizations used, two differences also emerge. First, the creation of an area of thicker ice close to the ice edge where the wave stress is strongest when using the *Sutherland et al.* (2019) attenuation in the weakened ice. Secondly, once the ice has reached an equilibrium with the forcing after 60 hours, as shown in Fig. 3.7, the thickness profile is much sharper for the *Sutherland et al.* (2019) attenuation due to its stronger attenuation for small thicknesses. However, the final equilibrium thicknesses at the closed boundary are similar between the two formulations.

The difference in attenuation coefficient changes the sea ice dynamics significantly near the ice edge. In order to assess the impact of waves in the ice dynamics, the total force exerted by both waves and winds was calculated by integrating the stress terms from Eq. 3.1 starting at the ice edge. This method allows us to consider not only the local stress exerted, but also the stress transmitted by internal ice stresses. The difference between these two terms, as shown in Fig. 3.8, can be used to determine where waves dominate

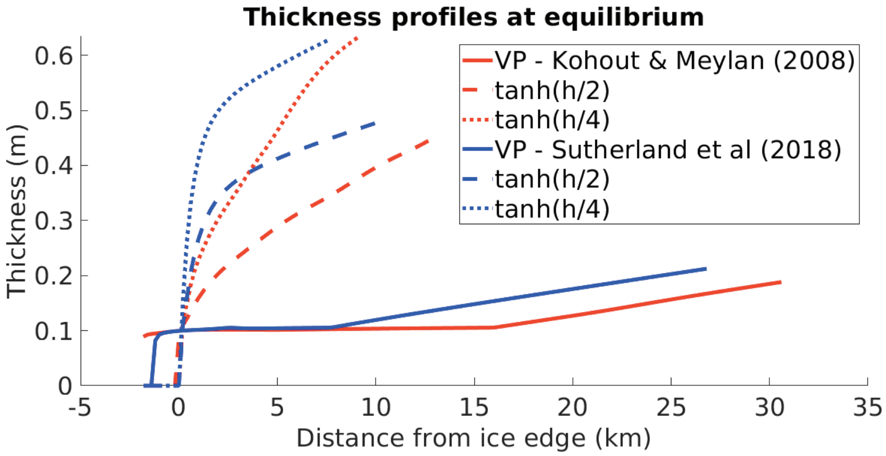

Figure 3.7: Sea ice equilibrium thickness profiles after 72 hours, showing curves for the attenuation formulations suggested by *Kohout and Meylan* (2008) (red) and *Sutherland et al.* (2019), using the regular VP ice strength (solid), or hybrid ice strength with a factor γ of $1/2$ (dashed) or $1/4$ (dotted).

over the wind in the ice dynamics, which could be used to define a dynamical marginal ice zone. Because the model does not include the dispersion which would maintain a gradient in concentration but instead focuses on applying the wind and wave stresses to compress the ice, a direct comparison with the typical floe size or concentration oriented definition is not possible. However, it is clear that in the situation presented here, or in the calmer conditions with winds and currents supporting dispersion, the MIZ extents would be very different.

The stronger attenuation predicted by the fitted *Sutherland et al.* (2019) parameterization (Fig. 3.8, bottom) creates much larger stresses, the influence of which is felt much further in the ice, creating a dynamical MIZ around three times as wide. Interestingly, for the weakest ice modeled (Fig. 3.8, right), the thickening of ice at the closed boundary allows attenuation of longer wave periods than what has been attenuated at the ice edge. This additional inshore wave stress causes further thickening and a dynamical MIZ width that is similar between the two attenuation methods, unlike the other two ice strength parameterizations.

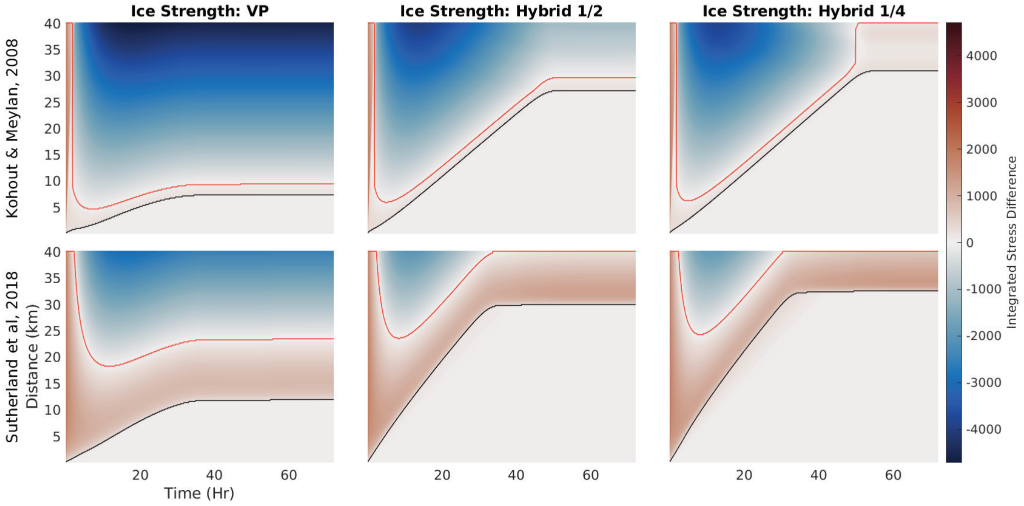

Figure 3.8: Integrated wave and winds stress difference using the original VP ice strength (left), the hybrid ice strength with $\gamma = 1/2$ (middle), or $\gamma = 1/4$ (right), using the attenuation formulations suggested by *Kohout and Meylan* (2008) (top) or *Sutherland et al.* (2019) (bottom).

3.3 Modeled wave impact on ice

To asses the possible effect of including wave forcing in sea ice models, multiple model runs were performed for a range of wind speeds and initial ice thicknesses using both the P_{Hibler} and P_{Hybrid} ice strength as well as the attenuation formulations by *Kohout and Meylan* (2008) and *Sutherland et al.* (2019). Initial conditions and wind forcing were uniform over the 80km domain, with wave forcing coming from a constant spectrum propagating from one boundary of the domain. Reference simulations were also run without waves. All simulations were performed for four days. This time was sufficient for the sea ice to reach a thickness where it can sustain the forcing from winds and waves combined, entering a steady state solution. Three parameters were chosen as the most descriptive of the impact of having waves in the simulation: the displacement of the ice edge, the width of the MIZ and the sea ice thickness at the shore-ward end of the MIZ.

The location of the boundary between open and ice infested waters is a critical forecast variable. Presence or absence of ice is key to navigation planning and waves can apply a large force right at the edge, moving it rapidly in their direction of propagation. In this case we consider the ice edge to be the location where ice concentration in the model goes

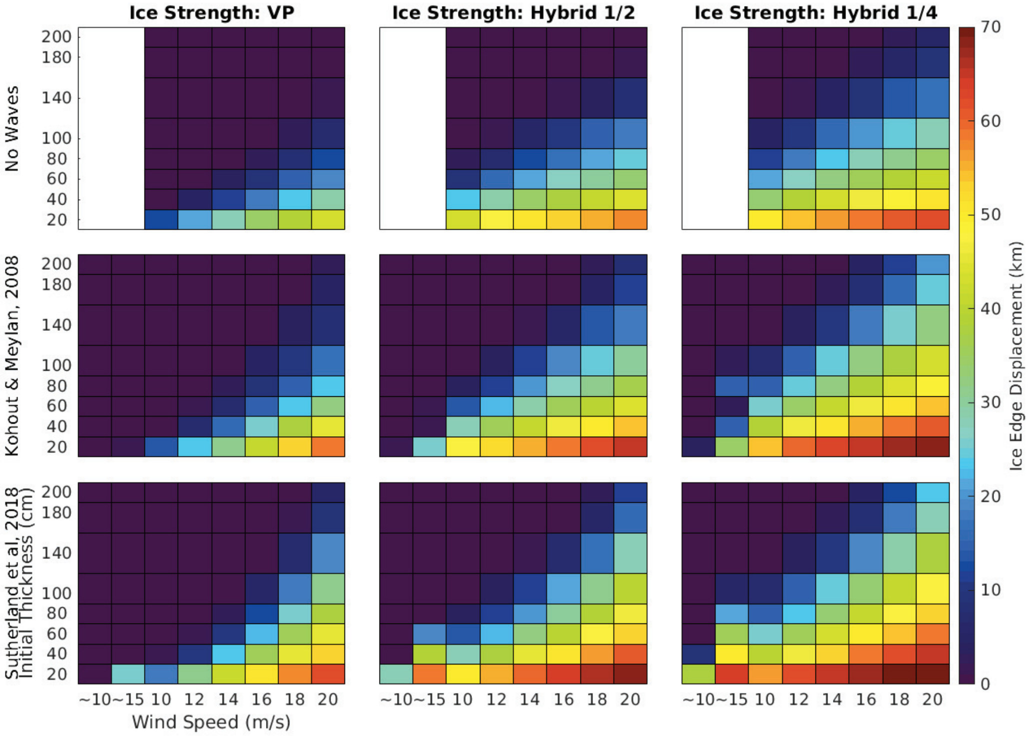

Figure 3.9: Ice edge displacement in kilometers, due to the combined effects of waves and winds, for wind speeds of 10 to 20 $\mathrm{m/s}$ and initial uniform ice thickness of 20 to 200 cm. Wind speeds preceded by a $\sim$ represent wave only forcing that would correspond to the given wind speed.

above 30%. Results shown in Fig. 3.9 present the effect of winds alone (top row) as well and the combined effect of winds and waves. In all cases, ice edge displacement increases with wind speeds and decreases with initial ice thickness. Even though the waves are essentially completely attenuated by the ice using both models, the *Sutherland et al.* (2019) attenuation formulation increases the displacement by creating a stronger energy gradient which is more effective at converting wave energy into a force on the ice. Weakening the ice through the hybrid formulation also increases displacement, but has more of an impact at low starting thicknesses.

Subtracting the displacement obtained in the reference, wind only, model runs from the runs with waves, the impact of adding waves can be seen to reach up to 20-25 km in Fig. 3.10. The impact of the choice of attenuation model also becomes much more

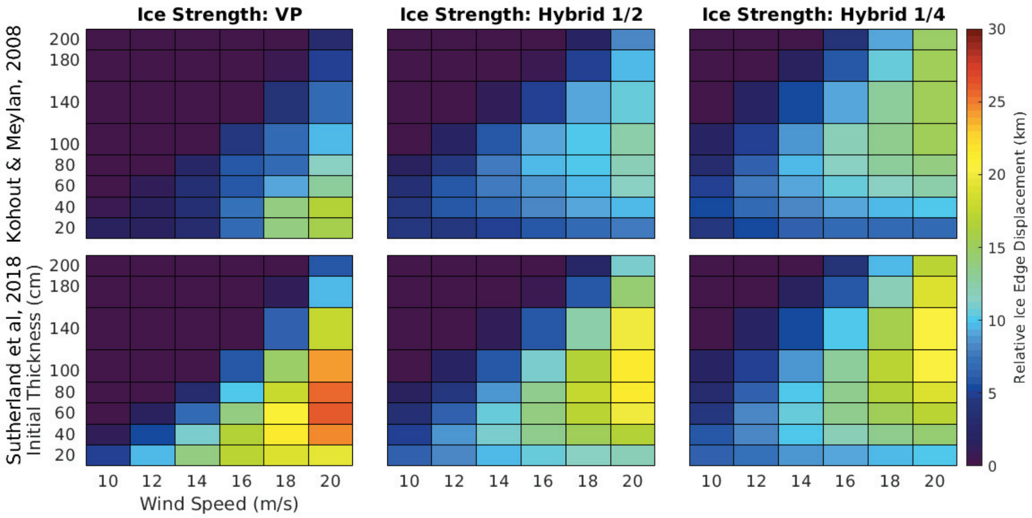

Figure 3.10: Ice edge displacement in kilometers, relative to the location in equivalent wave-free simulations, for wind speeds of 10 to 20 $\mathrm{m/s}$ and initial uniform ice thickness of 20 to 200 cm.

apparent. On average, the *Sutherland et al.* (2019) attenuation model displaces the edge by 5km more in weaker ice. In the case of the VP ice, a difference in displacement of up to 15km can be seen, due to the ice remaining thin, a range where the two formulations differ significantly.

The dynamical MIZ, defined as the region where the local applied force on the ice, or the integral of stresses from the ice edge, is dominated by waves, provides information on the scale of modeling where considering waves will be important. As seen in Fig. 3.11, the width of the MIZ tends to increase with wind speed. Wave energy and thus wave stress has a 4^{th} order dependence on wind speed while wind stress depends on wind speed quadratically. Longer fetches on ice are necessary for the wind stress to catch up to the stronger wave stress in terms of applied force, leading to the wider dynamical MIZ. The two attenuation formulations differ significantly in the shape of this dependence on initial thickness. With the formulation by *Kohout and Meylan* (2008), there are two different regimes depending on initial ice thickness. At low initial thickness, waves are attenuated only when the wind is strong enough to first compact the ice to a thickness where it can attenuate waves, leading to a local maximum at high winds and low thickness. In this case, wave attenuation occurs near the shore. At higher initial thickness, the ice is able

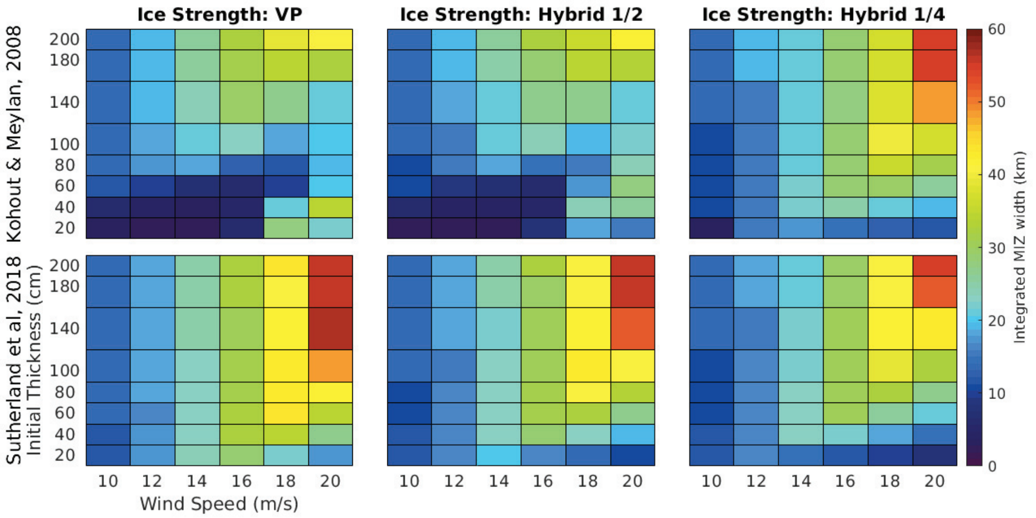

Figure 3.11: MIZ width in kilometers, measured by comparing integrated wind and wave stresses, for wind speeds of 10 to 20 $\mathrm{m/s}$ and initial uniform ice thickness of 20 to 200 cm.

to attenuate waves closer to the ice edge. In between the two regimes, a local minimum in MIZ width as a function of thickness is attained when the ice can resist the winds but is not thick enough to attenuate waves. The attenuation formulation by *Sutherland et al.* (2019), having stronger attenuation for low thickness, does not show the two regimes and attenuation is always greatest near the ice edge. In both attenuation formulations, the first increase of MIZ width with initial ice thickness is due to the dynamical MIZ extending to the boundary of the domain. The decrease in ice edge displacement as initial thickness increases leaves more of the model domain available to the MIZ. With a larger domain, the dynamic MIZ width would not show this dependence.

For a given wind speed and ice concentration, the local wind stress on ice is the same at every location. This value is much smaller than the peak wave stress. This allows thin ice to resist the local force near the ice edge if waves are not considered. Waves, by exerting stress at or near the ice edge, create a much sharper increase in thickness in that area. The ice thickness at the point where wind and wave force are equal, or equilibrium thickness shown in Fig. 3.12, gives a measure of the effect of waves depending on conditions. For the typical VP ice strength, waves are insufficient to compact even 20 cm ice up to wind speeds of 16 to 18 $\mathrm{m/s}$. Weakening the ice through the hybrid formulation allows waves associated with weaker winds to compact it. For a given wind speed, there is a specific

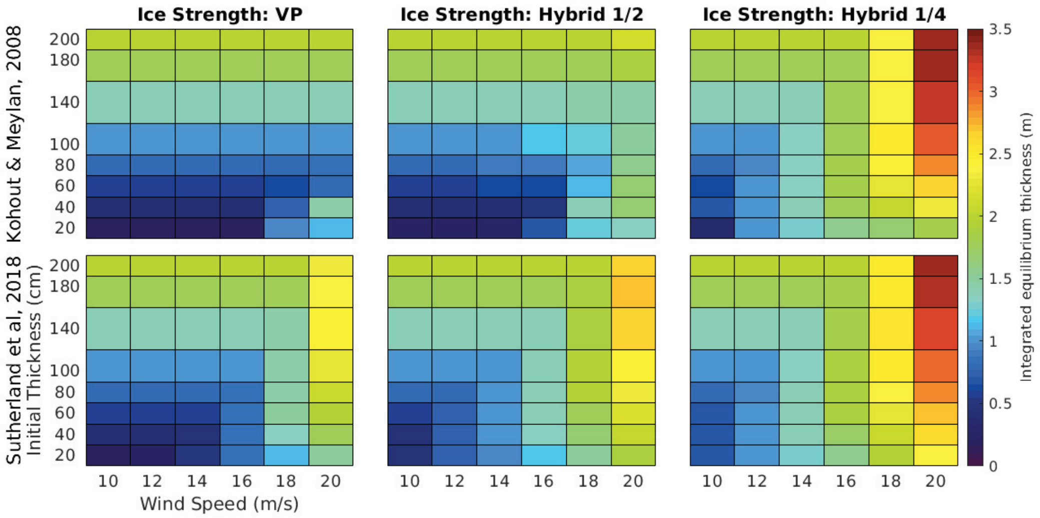

Figure 3.12: Ice thickness at the point where integrated wind and wave stresses are equal to each other, for wind speeds of 10 to 20 $\mathrm{m/s}$ and initial uniform ice thickness of 20 to 200 cm.

minimum ice thickness that will be able to balance it. Any initial ice thickness below that value will be compacted to that thickness, leading to the equilibrium thickness being independent of the initial value or vertical bands in the figure. Past that value, the ice is already strong enough to sustain the forces and will not be thickened, seen as horizontal bands in the figure. Both attenuation models reach similar values for the weakest ice where compaction enables thickening and stronger attenuation by the formulation by *Kohout and Meylan* (2008). Results differ for stronger ice where the thickness-attenuation-compaction feedback is more dependent on wave attenuation at low thicknesses. Similarly to the MIZ width, the decrease in thickness associated with low initial thickness is due to the model domain truncating the MIZ.

3.4 Discussion and Conclusion

Using a one-dimensional wave-ice model, it was possible to reproduce key mechanisms of wave-ice interactions in the marginal ice zone. Simulations showcased how dependent those features are on a complex balance of forces, most of which are still not well understood. By looking into which combinations of formulations reach an appropriate balance, insight into what might actually be happening in the marginal ice zone can be gained. The main contributions of this chapter are: (1) - a description of the evolution of sea ice when the wave radiation stress is considered, (2) - the production of thickness and equilibrium energy profiles considering the radiation stress, to be tested against observations and (3) - a presentation of the possible impact of the waves and ice strength on MIZ width, ice edge displacement and equilibrium ice thickness profiles.

The numerical experiments presented above showcased how the typical ice strength used when modeling sea ice at large scales fails when looking into the MIZ. This is of little surprise as, in the ice pack, ridging is necessary in order to compress ice. In the marginal ice zone, floes are much smaller and waves can facilitate mobility and rafting. This is represented in our study as a lower ice strength of thin ice that is expected to be more mobile. In the MIZ, ice strength parameterizations should ideally account directly for the effect of waves. Incorporating the ratio of ice thickness to wave height as a parameter in ice strength formulations could make it possible to account for the mobilization and easier rafting of sea ice caused by wave motions. This would likely provide a more physically grounded and versatile formulation, although it would be particularly challenging to measure wave height, ice thickness and deformation simultaneously. A combination of upward looking sonars to detect the sea ice draft and, from there, approximate ice thickness could be combined with pressure-based measurements of wave height in ice and remote sensing measurements of ice movement could be possible.

Models for wave attenuation currently abound, all for a specific set of circumstances but applied widely to all cases. As was the case in this study, changing formulations can have a wide range of effects. Combining multiple formulations, each dominant for different wave and ice characteristics, could be a way to ensure more realistic simulations. Until then, simpler average models may provide better results as was the case above.

Since waves and ice evolve in tandem, proper integration of both model components is necessary when testing models against realistic observations. As shown above, over the course of a few days necessary for the waves to achieve steady state, ice conditions can change significantly. Beyond improved models, further observation of waves in the MIZ, especially as the MIZ is adjusting to changing conditions, can play a pivotal role in informing the development of proper wave-ice interactions models. Specifically, open water and in-ice wave forcing along with ice thickness profiles from the ice edge can be particularly useful in validating models.

CHAPTER 4

MODELING THE ICE EDGE JET: INTERPLAY BETWEEN RADIATION STRESS AND ICE STRENGTH

The wave radiation stress component acting perpendicularly to the ice edge can be the main factor determining the ice edge location and the ice thickness nearby, as shown in *Leppäranta and Hibler III* (1985), *Dai et al.* (2004) and chapter 3. In the other direction, high ice velocities parallel to the ice edge have been observed by *Johannessen et al.* (1983) during the NORSEX experiment north of Svalbard using buoys deployed near the ice edge with winds either blowing along or slightly off the ice edge. They also observed meanders of the ice edge that they attributed to variations in the Ekman transport associated with wind stress differences between ice covered and open ocean conditions. Velocities up to $1\mathrm{m/s}$ were also observed using ship-borne and buoys measurements in the MIZ by *Lund et al.* (2018). Of particular interest were the observations of eddies in the MIZ and the small correlation with wind speeds ($R^2 < 0.4$) for low ice concentrations ($A < 50\%$). Using a coupled ice-ocean model, *Häkkinen* (1986) confirmed that under along-ice winds, slight variations in the ice edge shape or ice concentration near the edge can trigger barotropic and baroclinic instabilities. These instabilities can in turn cause ice edge meanders along with vertical movements and eddy shedding in open waters and under the sea ice. This turbulence in the MIZ can support mixing of sea ice and the underlying ocean. Studying the ice-ocean interactions in a numerical model, *Smith and Bird* (1991) linked observed sea ice structures near the ice edge to jet-eddy interactions. *Manucharyan and Thompson*

(2017) also showed that melt water fronts at the ice edge can lead to mixed-layer instabilities. Using an idealized coupled wave-ice-ocean model, *Liu et al.* (1993) demonstrated that the radiation stress produced by incoming waves can accelerate the formation of eddies. *Dai et al.* (2019), using a wave-ocean-ice model, confirmed that waves can drive unstable currents in the MIZ and *Zhang et al.* (2020) investigated the effects of the angle of incidence and water depth on the ice edge jet.

These studies place waves as one of the primary drivers for mesoscale dynamics in the MIZ. As shown in chapter 3, the wave radiation stress is dependent on ice mechanical properties. Determining the role played by sea ice rheology as a modulator of the relationship between ice thickness, wave attenuation and ice velocities thus complements the work described above on MIZ dynamics and turbulence. In this chapter, we examine how wave radiation stress can create the ice edge jet and how the interplay of wave attenuation, radiation stress, ice compression and shear will modify the maximum velocity and width of the ice edge jet. In order to do so, the possibility of winds and waves coming at an angle to the domain is added to the model described in chapter 3 and the sea ice component is expanded to enable the consideration velocities perpendicular to the domain. The perpendicular forcing, particularly the wave radiation stress which can be particularly large near the ice edge as shown in chapter 3, will be resisted by water drag and the shear resistance of the sea ice. This enables the investigation of shear, an aspect of ice rheology untouched so far in this thesis and to study the effect of weakening thin sea ice with the hybrid ice strength (Eq. 3.7) on shear stresses in the sea ice and jet velocity. In section 4.1, the numerical model used is described. In section 4.2, the cases studied are presented while section 4.3 contains a discussion of the energy balance in the jet and conclusions.

4.1 Model description

The combination of a 1D viscous-plastic (VP) sea ice model and a basic spectral wave model, as described in chapter 3, is used in this study. Since this study focuses on sea ice velocities parallel to the shore and ice edge, the model is modified to use vector velocities. Ice velocity components are determined by the momentum balance in the two directions while both the waves and wind are defined at an angle θ to the model domain (see Fig. 1.6). The model domain remains the same as in chapter 3, with one open boundary where waves propagate into the domain and one closed boundary to represent the shore, as first described in Fig. 2.1. A no-slip condition was added also added to the shore in the parallel-to-shore direction. A value of $\theta = 45^o$ is used in this study unless otherwise specified.

In the wave model, attenuation is the only source term active for waves, enabled only in the ice. Otherwise wave energy is generated at the open water boundary, advected using the Lax-Wendroff advection scheme with Superbee flux limiter and completely absorbed at the model closed boundary.

The only modification to the wave component of the model in chapter 3 is the consideration of the angle θ in the wave energy advection-attenuation equation ($c_{gx} = \mathbf{c_g} \cos\theta$):

$$\frac{\partial E_{wv}}{\partial t} + c_{gx}\frac{\partial E_{wv}}{\partial x} = S_{\text{ice}} \tag{4.1}$$

Propagation at an angle can substantially slow down the penetration of waves into the model domain. In any given grid cell, the attenuation per unit time, $\beta = c_g\alpha$, remains the same. This results in a much larger apparent attenuation per unit distance perpendicular to the ice edge, or attenuation per grid cell, for a given attenuation per distance traveled (α), in accordance with Eq. 1.3. In order to test the impact of attenuation models on the dynamics of the ice edge jet, two different ones were considered, the scattering based formulation by *Kohout and Meylan* (2008) and the two-layer dissipation formulation by *Sutherland et al.* (2019).

The ice model uses a simple mass balance without thermodynamics and with an upwind advection scheme as in chapter 3. The momentum balance parallel and perpendicular to shore are solved for the two velocity components. The full two-dimensional momentum equation (Eq. 1.4) are however simplified by assuming that there are no gradients in the direction parallel to shore, or perpendicular to the model domain ($\frac{\partial}{\partial y} = 0$).

In the x-direction, defined to be perpendicular to shore and parallel to the domain, Eq. 1.4 equation simplifies to:

$$\rho h\frac{\partial u}{\partial t} = \tau_{ax} + \tau_{wvx} - \tau_{wx} + \frac{\partial \sigma_{xx}}{\partial x}, \tag{4.2}$$

where u is the sea ice velocity component along the x-axis (perpendicular to the ice edge or shoreline) and σ_{xx} is the first element of the σ 2×2 internal stress tensor (*Hibler III*, 1979). Because of the uniformity assumed in the y-direction, other terms vanish, leaving this component of the momentum equation similar to that of a 1D model such as used in chapter 3.

Under the uniformity assumption, the y-component of the momentum equation becomes:

$$\rho h \frac{\partial v}{\partial t} = \tau_{ay} + \tau_{wvy} - \tau_{wy} + \frac{\partial \sigma_{yx}}{\partial x}, \tag{4.3}$$

where v is the sea ice velocity component along the y-axis (parallel to the ice edge or shoreline) and σ_{xy} is the off-diagonal element of the internal stress matrix.

By construction, the wave-ice model requires the assumption that the underlying water is at rest. With winds and waves forcing the motion, it is expected that currents would develop in the same direction as the ice movement and reduce drag on the ice. The current setup can then be considered to produce a low-end estimate of the jet velocities. The ice speed is also neglected compared to the wind speed, as there is at at least an order of magnitude difference between them. The air and water stresses on the ice are vectors defined as:

$$\boldsymbol{\tau}_a = A\rho_a C_{da} |\boldsymbol{u}_a| \boldsymbol{u}_a \tag{4.4}$$

$$\boldsymbol{\tau}_w = A\rho_w C_{dw} |\boldsymbol{u}| \boldsymbol{u} \tag{4.5}$$

where A is the sea ice concentration, ρ_a, ρ_w, C_{da} and C_{dw} are the densities and drag coefficients of air and water, respectively, and $\boldsymbol{u}_a$ is the surface wind vector and $\boldsymbol{u}$ is the ice velocity vector.

The general, two-dimensional, internal stress matrix for a VP ice model is defined as in *Hibler III* (1979):

$$\sigma_{ij} = 2\eta\dot{\epsilon}_{ij} + (\zeta - \eta)\,\dot{\epsilon}_{kk} - P\delta_{ij}/2 \tag{4.6}$$

where i and j denote directions (1 for $\hat{x}$ and 2 for $\hat{y}$), σ_{ij} represent the stress in the i^{th}

direction on borders normal to the j^{th} direction, $\epsilon_{11} = \frac{\partial u}{\partial x}$, $\epsilon_{22} = \frac{\partial v}{\partial y}$ and $\epsilon_{12} = \epsilon_{21} = \frac{1}{2}\left(\frac{\partial u}{\partial y} + \frac{\partial v}{\partial x}\right)$ are the strain rates. The bulk and shear viscosities, ζ and η, are given by

$$\zeta = \frac{P_p}{2\Delta} \tag{4.7}$$

and

$$\eta = \zeta \mathrm{e}^{-2} \tag{4.8}$$

where $\mathrm{e} = 2$ is the aspect ratio of the elliptical yield curve (*Hibler III*, 1979), P_p is the ice strength and Δ is a non-linear function of the deformation rates. While ice strength, P_p, impacts the resistance of ice in both compression and shear, it is important to note that the ellipticity (e) could be varied to change the relationship between the shear viscosity (η) and the bulk viscosity (ζ). This could be used to modify the ice edge jet without changing the behavior of ice in compression. In the interest of studying how weakening of the ice in general impacts the ice edge jet, ellipticity is kept at its usual value of 2 here. Because of the uniformity alongshore (y-direction), Δ simplifies to:

$$\Delta = \left[(1 + \mathrm{e}^{-2})\left(\frac{\partial u}{\partial x}\right)^2 + \mathrm{e}^{-2}\left(\frac{\partial v}{\partial x}\right)^2 + \epsilon_2\right]^{1/2} \tag{4.9}$$

where ϵ_2 is a small parameter to remove the potential singularity from ζ. Finally, $P = 2\zeta\Delta$ is a pressure-like term dependent on strain-rates such that ice resists compression. As in chapter 3, the ice strength (P_p) be defined as either P_{Hibler} (P_p in Eq. 2.8) or P_{Hybrid} (Eq. 3.7).

Lastly, $\boldsymbol{\tau}_{wv}$, the stress exerted by waves on the ice, is the two-dimensional extension of the one defined in Eq. 3.4, obtained by considering the radiation stress defined by *Sutherland and Dumont* (2018). In two dimensions, the wave stress is defined as:

$$\boldsymbol{\tau}_{wv} = -\nabla \cdot \mathbf{R} = -\frac{\partial}{\partial x_i} R_{ij} \hat{j} \tag{4.10}$$

where $\mathbf{R}$ is the wave stress tensor. In our case, because of the assumptions of uniformity in the y-direction and a single direction of propagation for waves, the only two elements of $\mathbf{R}$ that are relevant are:

$$R_{11} = \rho_w g \int_0^\infty E_{wv}(f) \left[\frac{c_g(f)}{c_p(f)} \left(\cos^2\theta + 1 \right) - \frac{1}{2} \right] df \tag{4.11}$$

and

$$R_{12} = \rho_w g \int_0^\infty E_{wv}(f) \frac{c_g(f)}{c_p(f)} \cos\theta \sin\theta \, df \tag{4.12}$$

given a wave energy spectrum $E_{wv}(f)$ and wave frequencies (f).

4.2 Modeling the ice edge jet

Simulations were performed using the model, starting with sea ice 10 cm thick everywhere on the model domain. The ice is at rest and covers 70% of every grid cell's area. For numerical stability reasons, there is no wind initially. Over a period of six hours, the wind speed increases to 10 $\mathrm{m/s}$, blowing at an angle $\theta = 45^o$ relative to the model domain as defined in Eq. 4.1 and shown in Fig. 1.6. Waves are also generated at the open boundary (bottom of panels) and propagate in the domain at the same angle as the winds. Wave energy increases over the same period as the winds and the final energy spectrum is at equilibrium with the 10 $\mathrm{m/s}$ winds.

In the first 10 hours of the simulations, ice is pushed towards the shoreline (top of panels, see Fig. 2.1) without resistance or thickening as the available open waters get covered first (Fig. 4.1). Note that thickness values are not displayed for open waters. The ice edge can be seen retreating rapidly from the open boundary of the domain towards the shoreline. Once the ice concentration approaches 100%, thickening of the ice from the initial 10 cm, up to 55 cm occurs at the shoreline as a response to the stresses exerted on the ice (Fig. 4.1). Weakening the ice strength by changing from the VP formulation (Eq. 2.8, shown in the left column) to the hybrid formulations (Eq. 3.7, shown in the center and right columns) enables larger thicknesses to be reached and greater thickness gradients. Noticeably, in simulations with waves (Fig. 4.1 top and middle row), weaker ice thickens near the ice edge as well, where wave stress is balanced by ice inertia and water drag instead of internal stress and the shoreline.

Wave energy attenuation increases over time as the ice thickens, with the scattering

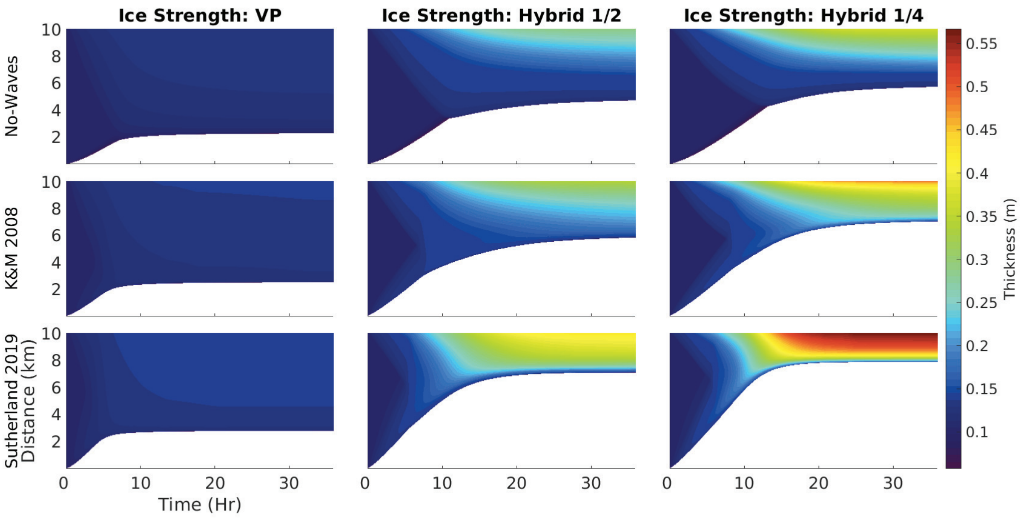

Figure 4.1: Ice thickness using the original VP ice strength (left), the hybrid with $\gamma = 1/2$ (middle), or $\gamma = 1/4$ (right), without waves (upper panels) or using the attenuation formulations suggested by *Kohout and Meylan* (2008) (middle panels) or *Sutherland et al.* (2019) (lower panels).

formulation attenuating much less than the dissipation formulation (Fig. 4.2). Most of the wave attenuation happens near the ice edge as soon as waves of a given frequency encounter ice thick enough for significant attenuation. Lower frequency waves may not be significantly affected by the ice over the distances considered in the model.

The wave attenuation creates the energy gradient necessary to establish the wave radiation stress (Fig. 4.3 as per Eq. 4.11 and Eq. 4.12). The stress component perpendicular to the ice edge is either balanced by inertia in the initial hours of the simulations or by internal ice stress once the ice compacts, thickens and slows sufficiently as described in chapter 3. In all cases, the wave stress is well constrained near the ice edge, acting on a distance of up to one kilometer at most. In that area, the wave stress is at least an order of magnitude stronger than the wind stress (Fig. 4.4) but wave stress is lower further into the ice pack.

In the direction parallel to the ice edge, the wave stress accelerates the ice and establishes the ice edge jet (Fig. 4.5). The jet can be observed in all simulations at the ice edge, with the maximum speed being larger for the dissipation attenuation and for weaker ice

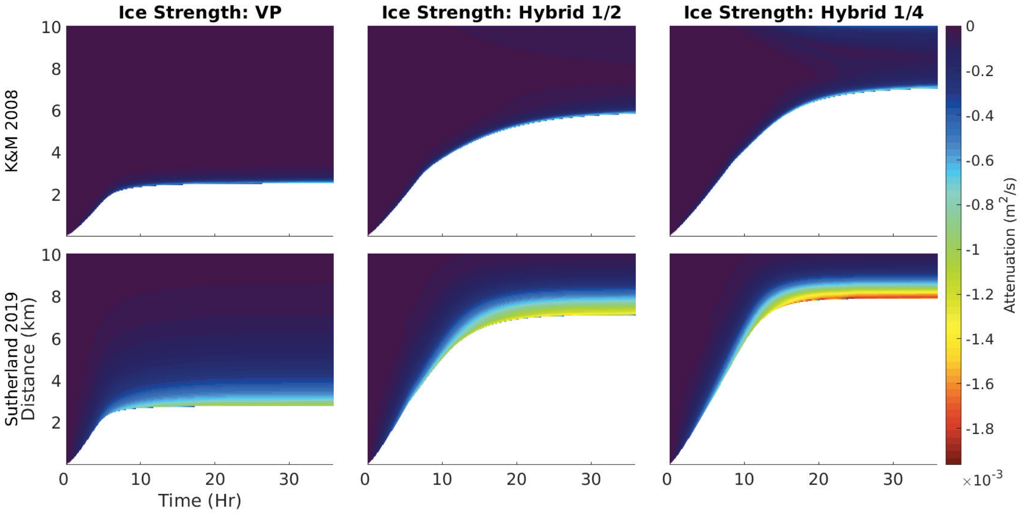

Figure 4.2: Wave energy attenuation using the original VP ice strength (left), the hybrid with $\gamma = 1/2$ (middle), or $\gamma = 1/4$ (right), without waves (upper panels) or using the attenuation formulations suggested by *Kohout and Meylan* (2008) (middle panels) or *Sutherland et al.* (2019) (lower panels).

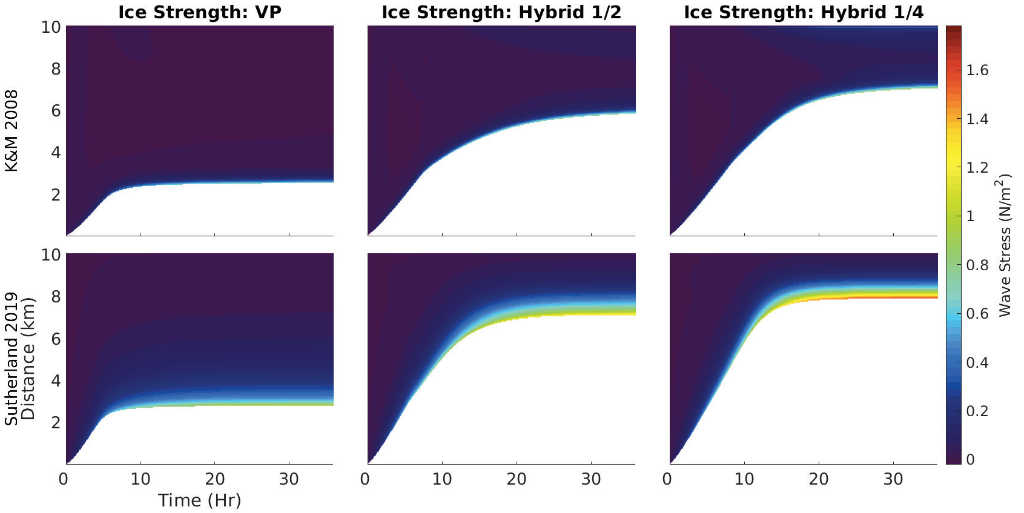

Figure 4.3: Wave stress using the original VP ice strength (left), the hybrid with $\gamma = 1/2$ (middle), or $\gamma = 1/4$ (right), using the attenuation formulations suggested by *Kohout and Meylan* (2008) (middle panels) or *Sutherland et al.* (2019) (lower panels).

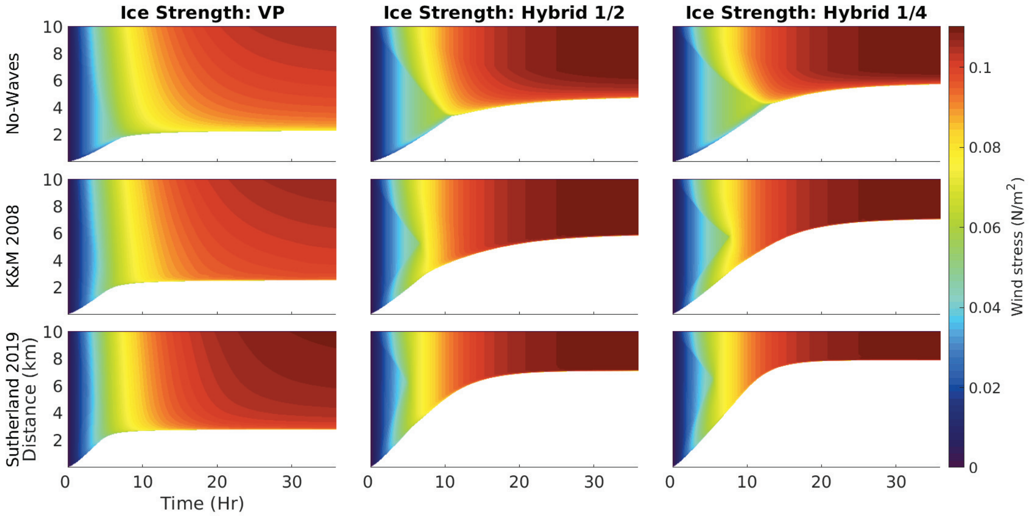

Figure 4.4: Wind stress using the original VP ice strength (left), the hybrid with $\gamma = 1/2$ (middle), or $\gamma = 1/4$ (right), without waves (upper panels) or using the attenuation formulations suggested by *Kohout and Meylan* (2008) (middle panels) or *Sutherland et al.* (2019) (lower panels).

strength. The intensity and width of the jets are well correlated with energy loss (Fig. 4.2). The inner ice pack away from the edge also has non-zero velocities from the balance between the wind (Fig. 4.4) and water drag (Fig. 4.6). This velocity is however much lower than the velocity attained within the ice edge jet with the additional wave forcing, making the water drag within the ice pack much weaker than near the edge as well.

Using constant forcing, the simulations all reach a steady state after 72 to 96 hours where the wind and wave stress on the ice are balanced by the ice internal strength. The final thickness profile (Fig. 4.7, left) is both the result and the outcome of this balance in the direction perpendicular to the ice edge, acting as the fulcrum by modulating both the ice strength and wave attenuation. Here, five different simulations using the VP ice strength and factors γ of 1/4, 3/8, 1/2, 3/4 in the hybrid formulation are used to better map the dependency. Increasing values of the γ factor for the hybrid formulation (Eq. 3.7) weakens the ice, in turn forcing an increase in ice thickness to balance the applied stresses, as shown in chapter 3. Changing the wave attenuation instead changes the shape of the thickness profile near the ice edge rather than the final thickness. The extreme case of having no waves shows the most different shape of thickness profiles, with initially no

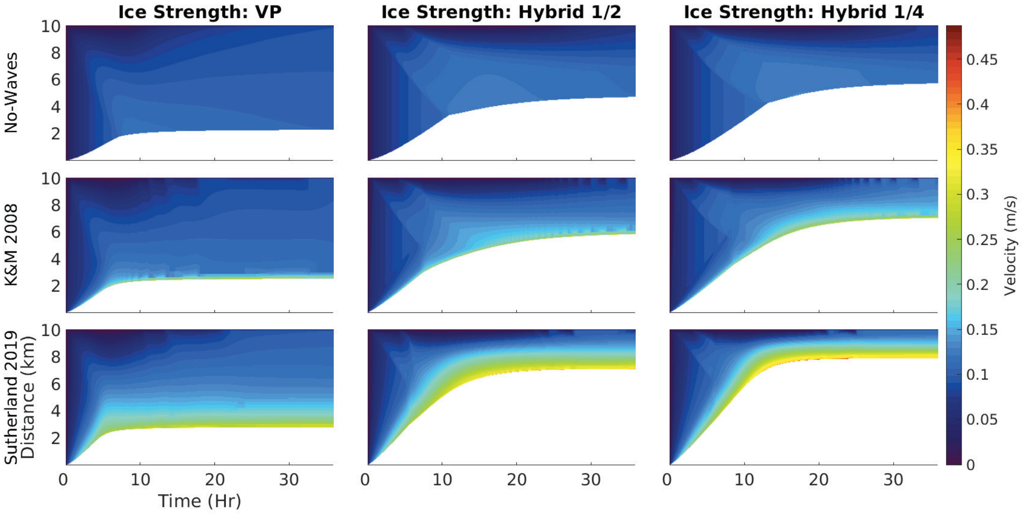

Figure 4.5: Velocity parallel to shore using the original VP ice strength (left), the hybrid with $\gamma = 1/2$ (middle), or $\gamma = 1/4$ (right), using the attenuation formulations suggested by *Kohout and Meylan* (2008) (middle panels) or *Sutherland et al.* (2019) (lower panels).

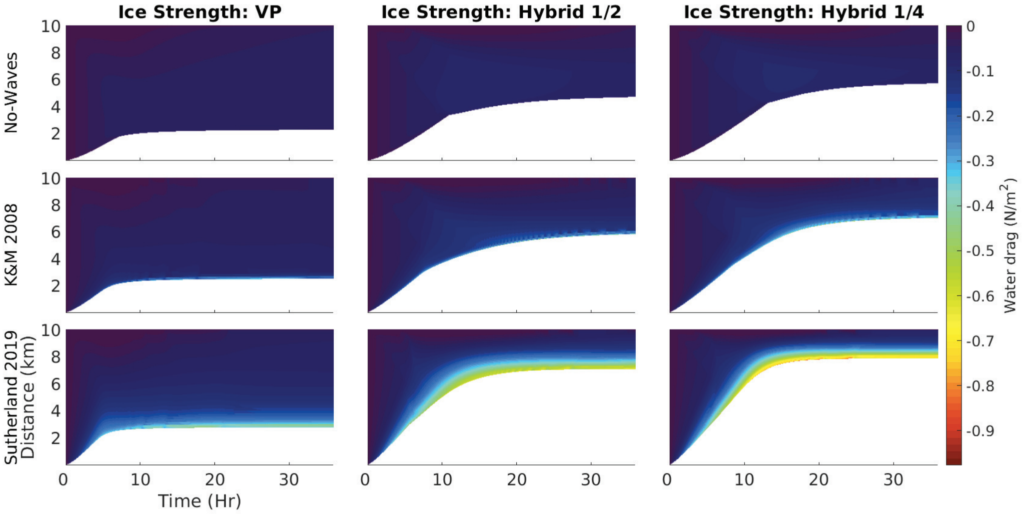

Figure 4.6: Water drag using the original VP ice strength (left), the hybrid with $\gamma = 1/2$ (middle), or $\gamma = 1/4$ (right), without waves (upper panels) or using the attenuation formulations suggested by *Kohout and Meylan* (2008) (middle panels) or *Sutherland et al.* (2019) (lower panels).

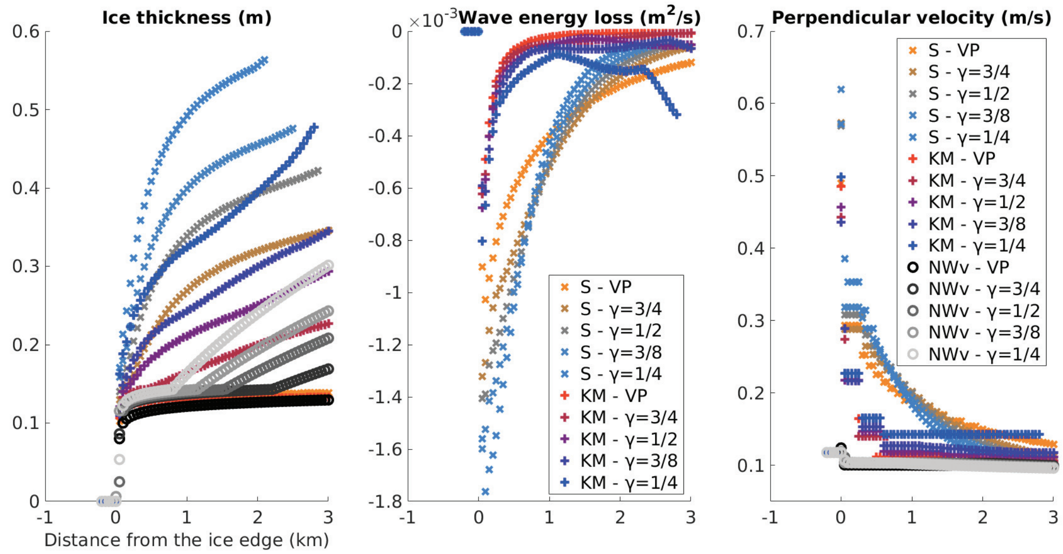

Figure 4.7: Ice thickness (left), wave energy attenuation (center) and velocity perpendicular to the ice edge (right) at model equilibrium using the attenuation formulations suggested by *Sutherland et al.* (2019) and *Kohout and Meylan* (2008) for a range of factors γ.

thickening since there is no wave forcing. There, the only increase in thickness occurs further from the edge where the integrated wind stress can overcome the ice strength. Beyond the present interest in the ice edge jet created along with these velocity profiles, the noticeable difference in thickness would also change local heat-fluxes which are inversely proportional to ice thickness. The largest thicknesses predicted here also approach the lower accepted thickness for ice rated ships. Combined with the incident waves, the ice conditions simulated here would create an environment hostile to most vessels.

Thicker sea ice increases wave attenuation (Fig. 4.7, center). Weaker ice creates steeper attenuation curves in the wave dissipation attenuation by thickening the ice near the ice edge. Since thicker ice attenuates more, there is less energy to be attenuated further into the MIZ (ex.: Fig. 4.7 center, light blue curve). Stronger ice remains thinner under similar stresses, and thus attenuates energy less at a given distance from the ice edge, allowing more energy to be attenuated further (ex.: Fig. 4.7 center, orange curve).

The ice edge jet depends most strongly on the choice of wave attenuation formulation (Fig. 4.7, right), as can be seen by profiles with waves forming two clusters. Without waves, the wind forcing is uniform, no jet is present and the ice velocity is almost uniform,

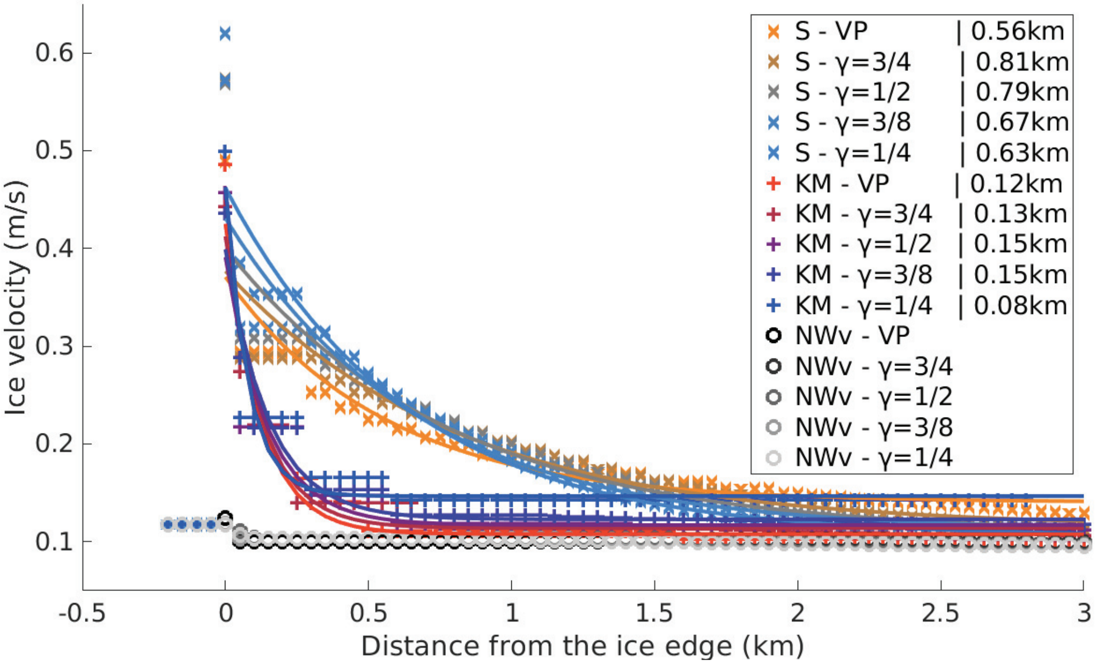

Figure 4.8: Velocity parallel to shore using the attenuation formulations suggested by *Sutherland et al.* (2019) (orange to cyan) and *Kohout and Meylan* (2008) (red to blue) or without waves (black to grey) for a range of factors γ, with exponential fits. Exponential scale lengths for the fits are displayed in the legend.

close to the values with waves further in the ice pack. Through the effect of ice strength on ice thickness and in turn on attenuation, the ice edge jets become wider, if initially weaker, with stronger ice, as can be seen by the characteristic length scales presented in Fig. 4.8.

While there is no apparent relationship between ice strength and jet width, weaker ice attains higher maximum velocities and larger shear values in the jet. This is a two-fold effect. Weaker ice strength causes thicker ice near the ice edge and thus a more localized attenuation and wave stress (Fig. 4.9, left). It also lowers shear resistance in the ice, as shown in Eq. 4.8. Shear resistance could influence the width of the jet by increasing the momentum transfer shore-ward from the fast moving ice edge. However, the larger velocity gradient of the weaker ice simulations outweighs the weaker shear resistance, leading to stronger internal shear stresses overall (Fig. 4.9, Right).

The angle at which the wind is blowing (θ, defined relative to the x-direction) determines how much of both the wind and the wave forcings result in compression and

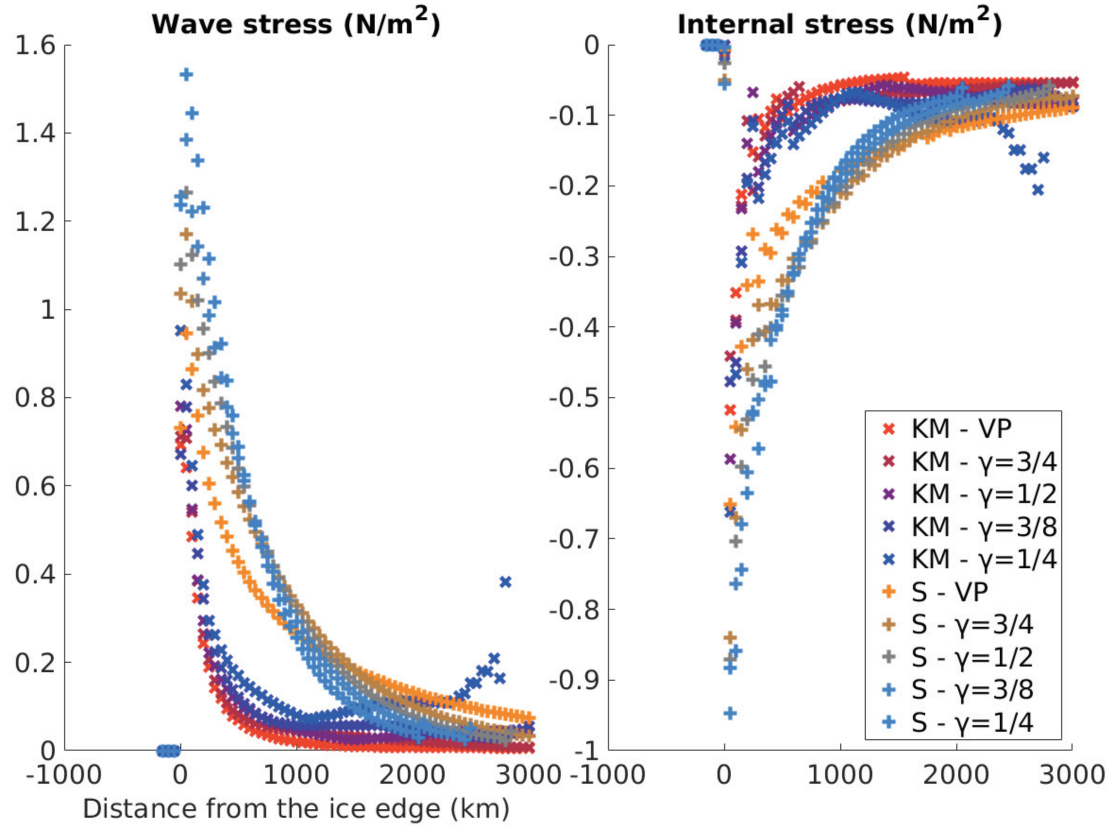

Figure 4.9: Wave stress (left) and ice internal stress (right) at model equilibrium using the attenuation formulations suggested by *Sutherland et al.* (2019) and *Kohout and Meylan* (2008) for a range of factors γ.

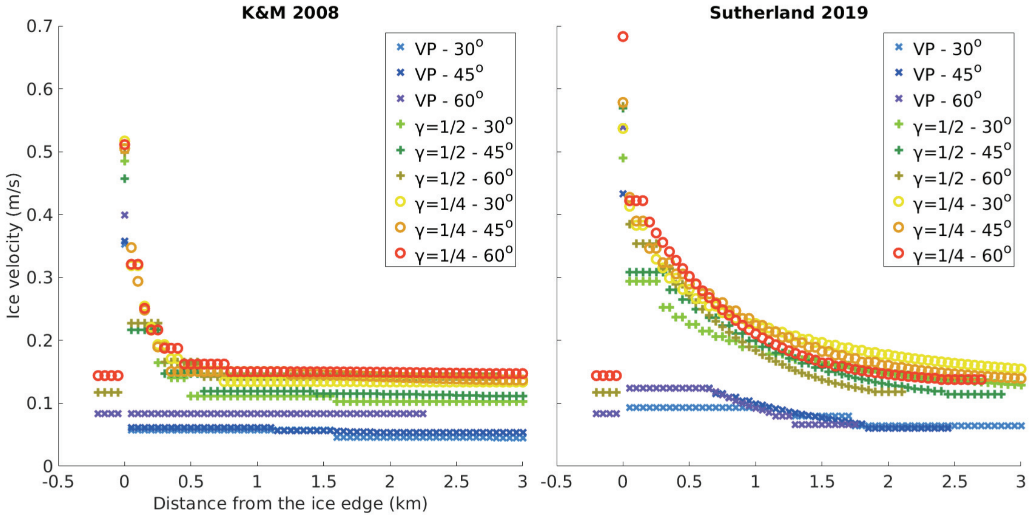

Figure 4.10: Velocity parallel to shore using the attenuation formulations suggested by *Kohout and Meylan* (2008) (left) and *Sutherland et al.* (2019) (right) for a range of factors γ, and angles θ.

thickening of the sea ice versus acceleration of the sea ice parallel to the shore. As shown in Fig. 4.10, in the range of angles considered, the main driver of jet characteristics remains the choice of attenuation scheme. A stronger attenuation leads to larger velocities over a wider distance. When using the hybrid ice strength, the forcing angle can have a similar effect on the ice edge jet as the variations in weakening factor used. In this case, a larger angle means more forcing leading to acceleration of the ice and thus larger maximum velocities. Meanwhile, less penetration of the waves and less thickening of the ice, leading to less attenuation overall and lower shear resistance in the ice, cause a narrower jet overall.

4.3 Discussion and Conclusion

The one-dimensional wave-ice model of chapter 3 was expanded to include the possibility of velocity and forcing in the direction perpendicular to its domain. Using the model, a region of high sea ice velocities, or jet, was simulated near the ice edge, as described in *Johannessen et al.* (1983). Predictions of the ice edge jet width vary from 100 m to near 1 km, with maximum velocities of 40 to 50 $\mathrm{cm/s}$. The main contributions of this chapter are: 1 - the full description of the physical system through which this jet is caused by the component of the wave radiation stress on ice parallel to the ice edge, 2 - the evaluation of the jet dependence on wave attenuation and ice strength, and 3 - the presentation of the momentum balance underlying this type of jet.

The velocity values obtained through the experiments presented here are similar to those reported in previous studies of the ice edge, ranging from 20 $\mathrm{cm/s}$ (*Liu et al.*, 1993) to 40 $\mathrm{cm/s}$ (*Dai et al.*, 2019) for weaker waves in thicker ice. However, the width of the jet was significantly larger in these studies, approaching 10 km. As shown here, the jet width is highly variable. This disagreement could be due to a number of factors, such as model resolution by reducing gradients or differences in ice properties, rheology or wave attenuation changing the local forcing or momentum transfer in the ice, or even domain size by changing the proximity of the coastline where velocity is forced to be zero. The main conclusions, however, are the same: Waves can force significant ice movements parallel to the ice edge, with velocities approaching 1 $\mathrm{m/s}$, highlighting the importance of considering waves in high resolution ice modeling. When modeled in two-dimensions, a fast enough ice edge jet can become unstable through Kelvin-Helmholtz instability for example, as shown by *Dai et al.* (2019). This creates mesoscale structures able to influence ice transport and air-sea fluxes of heat, moisture as well as tracers relevant to biogeochemistry.

The wide range of possible jet characteristics reflects the complexity of the MIZ, where multiple unknown processes, such as wave attenuation, wave forcing on ice and ice rheology all influence the predicted jet. In this study, the strength of the wave attenuation is the major driver of the jet variations. Changes in internal ice strength as a proxy for ice processes that were not modeled, such rafting or the impact of floe size on the dynamics for example, had noticeable but secondary effects. This points towards the choice of wave attenuation formulation being especially important in the creation of coupled wave-ice models, a choice made particularly complex by the number of available parameterizations based on different considerations. To discriminate between or combine the available options, it will be necessary for ice models to include more details, most importantly floe size, in addition to thickness or thickness categories and concentration, in a manner similar to what is suggested by *Boutin et al.* (2018). This would be doubly beneficial by making these ice variables available to modify the ice rheology, such as decreasing shear resistance in fragmented ice by changing the ellipticity factor in the shear viscosity.

Despite being idealized and simplified, the chosen model is well suited to the work presented here. Beyond satellite images which lack the information and details required, current observations and theories of the MIZ are mostly limited to one-dimensional studies. The model was chosen to allow rapid simulation of many experiments. Its simplicity also enables the evaluation of the impact and interplay of the included processes to be clearly identified without being obfuscated by the complexity of a full model or realistic conditions. This gives a clear vision of what should be prioritized in the development of complete two-dimensional models and in the future design and analysis of field studies. More elaborate models would, however, be able to perform simulations of complex situations such as the development of instabilities or realistic conditions with irregular topography, forcing and features in the sea ice. A comparison between an averaged two-dimensional simulation and the one-dimensional simulations presented here would be valuable to evaluate the potential of maintaining rapid simple modeling capabilities in a perspective similar to that presented by *Bowyer and MacAfee* (2005) for trapped-fetch waves. As our observational capabilities improve, the MIZ will more readily be observed over whole areas instead of along transects. This development will further increase the relevance of two-dimensional models as a means to test our theories of MIZ processes.

Waves and ice are intertwined in the MIZ, allowing comparatively few measurements to have a wide range of applications. To build on the work presented here, observations of sea ice drift and floe size would be highly desirable. Both of these can be deduced from image or video analysis and neither requires human presence in the MIZ, making them much easier to obtain than ice thickness generally is. A comparison between model simulations and observations of the ice edge jet would be more practical than comparisons of ice thickness while granting similar insight in MIZ dynamics. Moreover, such observations would help to constrain shear viscosity values through their impact on the ice edge jet, providing a new avenue to study the rheology of sea ice. Building on this, floe size would directly impact the rheology by changing ice strength both in shear and compression through increased mobility and rafting. Time series of floe sizes could also help design fracture models. Finally, waves have also been observed to modify ice strength, causing floes to move past or stack atop one another more readily, but waves have never been considered in definitions of sea ice rheology. Together, this relatively small set of variables could improve our understanding of the MIZ substantially.

CHAPTER 5

WAVE IMPACTS ON THE ICE ADVECTION-FORMATION BALANCE NEAR THE ICE EDGE

Sea ice drift is strongly governed by wind forcing. Up to this point, the main focus of chapters 2-4 has been on the opposition of wind and the associated wave forcing by internal ice stresses. For winds blowing in the offshore direction, nothing opposes the ice drift. A new type of balance can be established between ice formation and ice drift over greater time scales. The model developed previously can be used to predict ice drift velocities and study other situations, such as the opening of polynyas and the equilibrium that defines ice edge locations offshore. Polynyas are open water areas in the ice cover, most often driven by winds or currents and topography. Mass and heat exchanges between the atmosphere and the ocean within polynyas can be orders of magnitude larger than in the surrounding ice pack. More generally, waves can develop in open waters and both accelerate and add structure to the sea ice, such as the bands described by *Wadhams* (1983) or frazil streaks due to Langmuir circulation as described by *Drucker et al.* (2003). In this chapter, the wind direction of the 1D model described previously is changed in the off-shore direction to reexamine the ice mass and heat balance when wave-dependent drift and ice compression are considered.

5.1 Background

5.1.1 Pease's (1987) polynya model

Pease (1987) presented a foundational description of wind-driven coastal polynya dynamics that we hereby revisit in the light of the greater understanding we have acquired about wave-ice interactions near the ice edge. This model is based on the idea first proposed by *Lebedev* (1968) that wind-driven polynyas attain a maximum size if the air and water are cold enough to allow enough sea ice formation to compensate for the ice drift. Frazil ice is formed at the ocean's surface, is collected in windrows and drifts at a speed controlled by Stokes drift and Langmuir circulation towards the ice margin where it accumulates and eventually consolidates into young first year ice. In a field study of the Saint Lawrence polynya, the initial inspiration for *Pease* (1987), *Drucker et al.* (2003) combined observations from moorings and satellites to test the model. Polynya extents of 15 to 30 km, sustained under winds of 8 to 20 $\mathrm{m\,s^{-1}}$, were reported, which generally agreed with model predictions, although varying the frazil collection depth to match the observed ice production lead to an under-prediction of polynya extents. It was also suggested that frazil could be present as deep as 20m in the water column within the Langmuir cells. The depth over which frazil accumulates, and thus the thickness of newly formed ice, was also found to vary with wind speed, between 10 and 20 cm initially under the aforementioned wind range, leading to ice of 25 to 50 cm. In general, the larger the polynya, the greater is the total ice formation rate. For a given ice drift offshore, there is a size at which it is balanced by the ice accumulation rate. Mathematically, this can be formulated as

$$\frac{dx_p}{dt} = u_i - x_p \frac{F_i}{h_c} \tag{5.1}$$

where x_p is the extent of the polynya from the coast or the landfast ice edge, u_i is the ice advection speed positive in the offshore direction, taken to be 3% of the wind speed as an order of magnitude estimate, F_i is the frazil ice volume formation rate per unit open water area $(\mathrm{m/s})$ and h_c is the frazil collection depth (m). The quantity x_pF_i corresponds to the total volume of frazil ice formed per unit distance in the y direction per unit time. If this quantity is divided by the thickness over which it accumulates, h_c, it then corresponds to the speed at the which the consolidated ice edge progresses inward due to ice formation, as illustrated in Fig. 5.1.

In her paper, Pease (1987) makes some important assumptions that we summarize here:

1. The frazil collection depth h_c is constant, although it is considered largely unknown and an important parameter to which the polynya behaviour is sensitive.
2. The speed of the consolidated first year ice is directly proportional to the wind speed.

Using these assumptions, it is possible to equate the drift of sea ice offshore with the progression of the ice edge towards the shore through ice formation to obtain a stable open water extent:

$$x_{p_{max}} = u_i h_i / F_i. \tag{5.2}$$

At wind speeds above about $10\,\mathrm{m\,s^{-1}}$, the ice formation term becomes dominated by sensible and evaporative heat fluxes which are themselves linearly dependent on wind speed, much like the ice drifting velocity. The open water extent thus tends to a constant value determined by air temperature as wind speed increase.

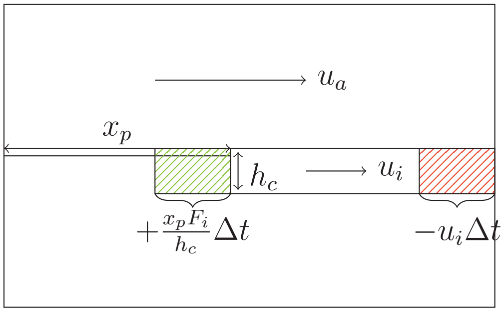

Figure 5.1: Schematic of the ice formation-advection balance established in *Pease* (1987). Frazil ice is compacted at the ice edge, forming new ice cover (green) which compensates for the ice advection (red).

5.1.2 Reexamining Pease's polynya model

In this chapter, we explore if and how the solution to the Pease model (Eq. 5.1) is influenced by surface gravity waves in wind-driven polynyas. The addition of wave radiation stress introduces a dependence of the ice velocity on fetch as well as wind speed through the influence of wave growth. Over small polynyas, predicted ice speeds could slow as wave forcing is small, whereas large polynyas would expand under strong wave forcing.

Additionally, the local wave forcing can thicken the ice cover by compression, as shown in the previous chapters on wave-ice interactions and by *Sutherland and Dumont* (2018). When frazil reaches the edge, it compresses and thickens due to the wave radiative stress up to a value such that the ice can resist compression. This thickening should make polynyas require larger ice volume productions before being stable, leading to larger polynyas. Together, these two considerations introduce further dependence on polynya extent in both terms in Eq. 5.1 as well as an extra wind speed dependence in the ice formation term. Taking these processes into consideration, the Pease model can be modified to include waves more explicitly, schematized in Fig. 5.2. Through both considered effects, the inclusion of waves should lead to a widening of the polynyas, allowing for greater local air-sea heat fluxes and ice formation, which would reduce the fluxes downstream because of the greater ice thickness.

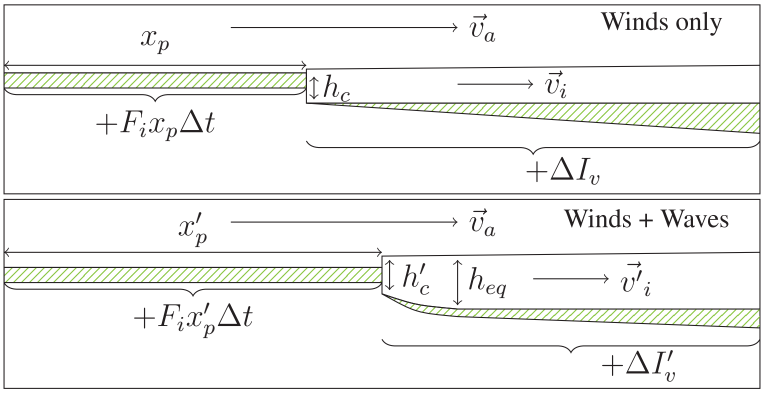

Figure 5.2: Comparison of conceptual models for polynya growth by winds (top) and winds and waves (bottom). Polynya extent (x_p) is determined by the balance between ice drifting ($\vec{v}_i$) and frazil volume formation ($F_i x_p \Delta t$). Consolidation at the ice edge turns the frazil into ice of thickness h_c, which can then grow thermodynamically as represented by ΔI_v. Waves cause the ice to drift faster (v'_i) and compress the frazil into thicker ice (h'_c) proportionally to the ice equilibrium thickness (h_{eq}). The combined wave effects lead to a greater open water extent (x'_p) and smaller thermodynamic growth ($\Delta I'_v$) due to the greater initial thickness.

5.2 Sea Ice Relationships

In order to incorporate wave effects in the model presented in *Pease* (1987), new relationships need to be considered, both in the 1D model presented in previous chapters and in the revisited theoretical model.

5.2.1 Fetch limited wave growth

The evolution of waves for given wind speed and fetch (x) values has long been studied. Their relationship can be approximated using three non-dimensional parameters for energy ($\epsilon = g^2 E_{wv}/u_a^4$), where E_{wv} is the wave energy, frequency ($\nu = f_p u_a/g$), where f_p is the wave peak frequency, and distance ($\chi = gx/u_a^2$). *Young and Verhagen* (1996), when looking at the early stages of growing waves that could be considered in deep water, found wave energy to be approximated well using the relationship of *Hasselmann et al.* (1973), obtained after the extensive JONSWAP measurement campaign in the North Sea:

$$\epsilon = 1.6 \times 10^{-7} \chi \tag{5.3}$$

and peak frequency to follow the formula derived by *Kahma and Calkoen* (1992) after reanalysis of the JONSWAP results along with several other field studies:

$$\nu = 2.18 \chi^{-0.27}. \tag{5.4}$$

For small fetch values and relevant wind speeds, these are well below the caps used to initialize waves in the previous chapters, which were given in *Bouws et al.* (1998). These caps can be non-dimensionalized and converted to:

$$\epsilon = 3.6 \times 10^{-3} \tag{5.5}$$

and

$$\nu = 0.0143. \tag{5.6}$$

A comparison of the fetch limited values and caps is shown in Fig. 5.3.

By equating Eq. 5.3 and Eq. 5.5, the distance at which wave height will become capped, χ_{max} is found to be

$$\chi_{\text{max}} = 2.25 \times 10^4 \tag{5.7}$$

leading to a dimensional fetch at which the energy reaches its maximum value, x_{max}:

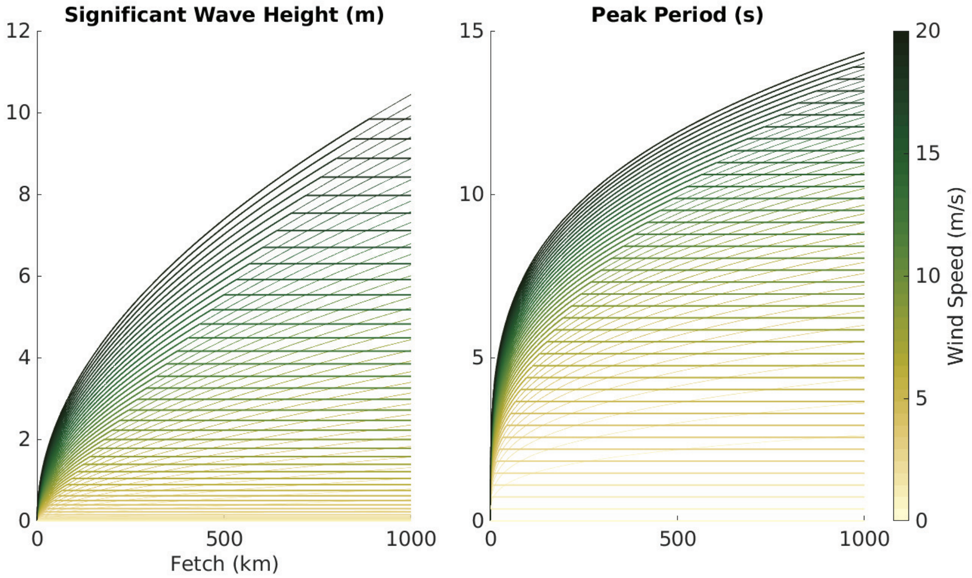

Figure 5.3: Comparison of fetch limited significant wave height (left) and peak period (right) to wind dependant caps. Bold lines show the combination of fetch dependent and capped equations. Thin lines show the continuation of fetch dependent variables for reference.

$$x_{\text{max}} = 2.25 \times 10^4 \frac{u_a^2}{g}. \tag{5.8}$$

Fig. 5.3 shows how increasing wind speed both increases the maximum attainable value, but also the energy and period at a given fetch. The transition point between the curved and straight segments of the wave height and peak period presented occurs at this fetch of maximal growth, x_{max}.

5.2.2 Wind and wave-dependent ice drift velocities

5.2.2.1 Numerical experiments

A series of numerical simulations were used to quantify the relationship between fetch, ice velocity and ice thickness. In each simulation, ice bands initially on the southern border of the domain were pushed northward by a constant wind forcing, as shown in Fig. 5.4. The initial thickness and extent of the initial band were varied, from 5 cm to 1 m thick and 1 km to 80 km wide and the ice itself was modeled using the VP and hybrid formulations first introduced in subsection 3.1.1. The waters offshore of the initial ice band were left either ice free, or covered in ice of the same thickness as the initial band but at a concentration of 70%. Wind speeds were varied from 5 to 20 $\mathrm{m\,s^{-1}}$. These simulation were performed using the model described in chapters 3 and 4, modified to allow for fetch limited wave growth as described in section 5.2.1. Implementing wave growth in this manner enabled the simulation of the positive feedback between fetch and wave forcing without having to fully model wave evolution.

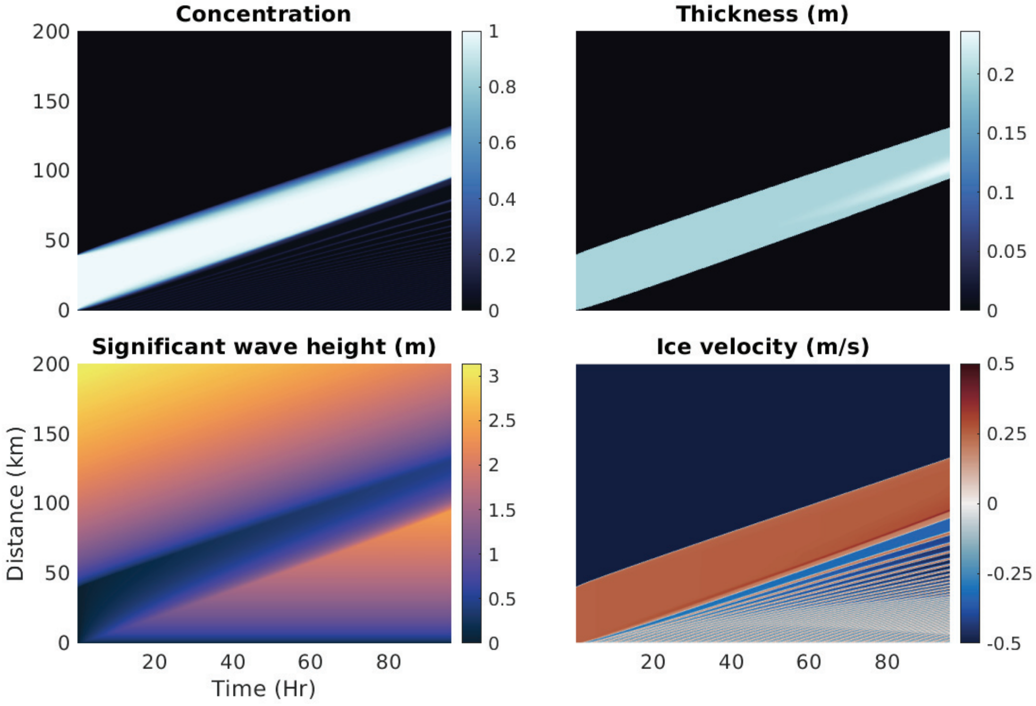

Figure 5.4: Example sea ice drift simulation for a 20 cm thick, 40 km wide ice band subjected to $15\mathrm{m/s}$ winds. The sea ice concentration (top left panel) and thickness (top right panel) are advected from the bottom boundary towards the other side of the domain. Waves grow with distance traveled starting from the bottom boundary but are attenuated when propagating in ice, with significant wave height (H_s) being shown. (bottom left panel). Ice velocity (bottom right panel) is maximized where concentration and thickness allow wind and wave stresses to be the greatest, with smaller velocity bands forming behind the main ice band.

Once the sea ice band moves away from the coast, it leaves behind open waters where waves can develop. Given the much lower speed of ice movement (O ~1-10 $\mathrm{cm\,s^{-1}}$) compared to wave propagation (O ~1-10 $\mathrm{m\,s^{-1}}$), fetch limited values for wave energy are used, computed by applying a JONSWAP spectrum shape to Eq. 5.3 and waves develop as soon as the ice retreats (Fig. 5.4). Eventually, as the fetch increases, waves grow big enough to push significantly on sea ice, accelerating the movement of the ice edge (Fig. 5.4). In the example case, as waves approach a 2 m height, with a fetch of about 60 km or after 60 hours, the local stress on the sea ice becomes sufficient to start thickening the sea ice (Fig. 5.4).

The simulations conducted can be divided in two main groups depending on whether or not the waters were ice-free offshore of the coastal ice band. For open waters, the ice band is in free drift and does not encounter any resistance beyond that of the water underneath as it moves away from the shore. With ice present offshore, more resistance is encountered and compression is more frequent within the ice band. For both experiments, simulations were clustered together to create a data set of ice edge velocity and their associated wind speeds, fetch distances and other variables such as ice thickness beyond the MIZ, shown in Fig. 5.5 along with grey surfaces showing the 3% value used in *Pease* (1987).

Most importantly, model simulations approach the 3% rule at longer fetch, especially for lower wind speeds. It is expected that the 3% rule becomes less applicable at high winds, much like ocean wind stress approaches an asymptote (*Wilson*, 1960). This shows that wind forcing alone, as defined in the model, does not allow modeled ice drifting velocities to reach observed magnitudes on which the 3% rule is based. However, once the ice has drifted offshore and the fetch allowed for wave growth, ice velocity increases and approaches 3% of the wind speed. Furthermore, thicker ice also coincides with larger ice velocities as wave attenuation increases and leads to higher wave radiative stress.

5.2.2.2 Ice drift velocity linear model

To enable the integration of waves in the polynya equilibrium model, results from the simulations were used. The aim was to obtain a simple expression, much like the 3% rule of *Pease* (1987). Wave energy depends on wind speed and fetch and the force applied by waves on ice depends on energy. As such, the simplest possible model is a regression of ice velocity as a function of wind velocity and open water fetch, of the form:

$$u_i = Au_a + Bx \tag{5.9}$$

with A and B constants to be determined through least square fitting.

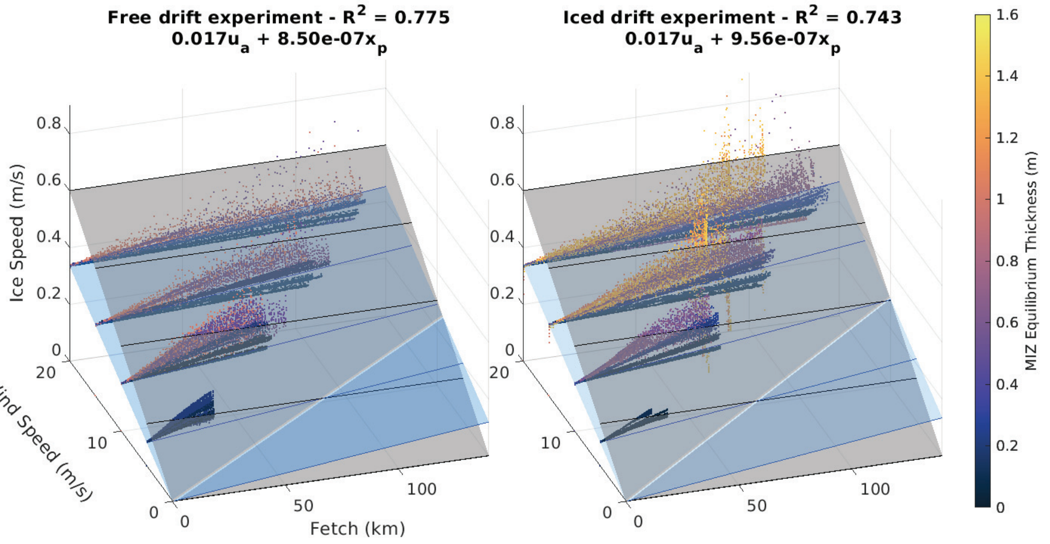

Figure 5.5: Ice drift velocity for two experiments, in free drift with ice free waters offshore (left) and with ice on the offshore waters (right). The grey surface represents 3% of the wind speed, as used in *Pease* (1987). The blue surface is a multi-linear fit using both wind speed and fetch to predict drift speed. Parameters for these fits are presented in Table 5.1. Noticeably, although drift velocities are mainly driven by wind speed, the majority of velocities simulated in the model are lower than 3% of the wind speed.

	Free drift experiment	Compact ice experiment
A	0.017	0.017
B	8.5×10^{-7}	9.56×10^{-7}
R^2	0.775	0.743

Table 5.1: Fitting parameters A and B and correlation coefficient R^2 for ice velocity as a function of wind velocity and open water fetch (Eq. 5.9).

These fits are shown as the blue surface in Fig. 5.5. While it is not a physics based model, no simple relationship could really capture the interplay among wind, waves and ice. This formulation provides us with a simple relationship that can easily be integrated in Eq. 5.1. Predicted ice velocities are lower for shorter fetches, but increase and can become greater at longer fetches. It should be noted that simulated velocities from the wave-ice model are almost all slower than 3% of the wind speed. As can be seen in Fig. 5.6, showing simulated velocities compared to the predictions of the fit, sea ice thickness varies with ice velocity residuals. However, thickness should also be predictable from wind speed and fetch and, indeed, the addition of thickness as a predictor did not improve the quality of the fit. The simple two variable model was thus preferred.

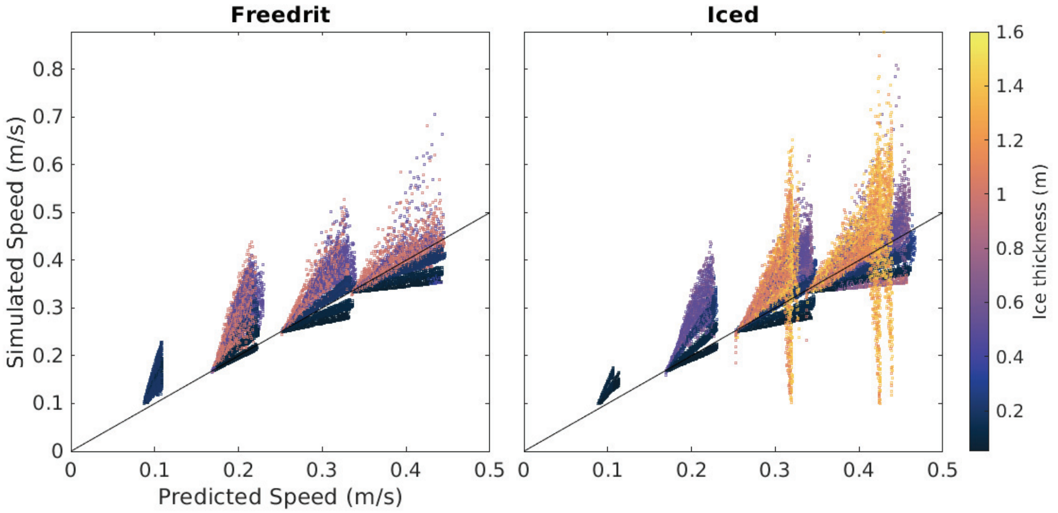

Figure 5.6: Comparison of the ice drift velocities simulated in numerical experiments and predicted using the multi-linear fit from Eq. 5.9. In both the free drift and iced experiments, higher drift speeds coincide with thicker ice shown by warmer colors.

5.2.3 Sea ice equilibrium thickness

To predict the equilibrium sea ice thickness, we go back to the relationship determined by *Sutherland and Dumont* (2018) in the marginal ice zone, given by

$$h_{eq}^2 = \frac{\rho_w g H_s^2}{8K_r} \tag{5.10}$$

where

$$K_r = \frac{1}{2}\left(1 - \frac{\rho_i}{\rho_w}\right)(1-n)\rho_i g \left(\frac{1+\sin\phi}{1-\sin\phi}\right), \tag{5.11}$$

is the horizontal compressive strength of the ice per unit volume, which depends on n the ice porosity and ϕ the internal friction angle. Combining this with the fetch limited growth equation (Eq. 5.3), we obtain an expression for the equilibrium thickness as a function of fetch distance and wind speed

$$h_{eq} = 5.66 \times 10^{-4}\sqrt{\frac{\rho_w x}{K_r}}u_a \tag{5.12}$$

subject to the cap of wind limited waves as per Eq. 5.5 and with a minimum of 10 cm. Since the compression of sea ice occurs over a certain distance, the frazil collection thickness, h_c, is considered to be a fraction of this value, chosen here to be 20%, leading to a wind and fetch dependent frazil collection depth:

$$h_{cw} = 0.2 \times 5.66 \times 10^{-4}\sqrt{\frac{\rho_w x}{K_r}}u_a = D\sqrt{x}u_a. \tag{5.13}$$

Taking $K_r = 939\,\mathrm{Pa\,m^{-1}}$, obtained with ice parameter values discussed in *Sutherland and Dumont* (2018), $D \simeq 1.2 \times 10^{-4}$.

5.2.4 Thermodynamic ice growth

The formation of sea ice is a complicated process. In its simplest form, it can be obtained by balancing the amount of heat lost by the ocean to the atmosphere with the latent heat released by the freezing of sea water. Following *Maykut* (1986), this can be expressed in differential form as:

$$\rho_i L \frac{\partial h}{\partial t} = F_T \tag{5.14}$$

where L is the latent heat of fusion, F_T is the heat flux, dependent on the temperature difference between the water ($T_w = T_f$, the freezing temperature) and atmosphere (T_a) and a transfer constant (C_T). Once a layer of ice has formed, two interfaces should be considered, between the atmosphere and ice and between the ice and water. Assuming the flux to be constant through the ice, and thus a linear temperature profile with surface temperature $T_i(0)$ and bottom temperature T_f, the flux through the ice is given by:

$$F_i = \frac{k_i}{h}(T_i(0) - T_f) \tag{5.15}$$

where k_i is the thermal conductivity of the ice. The heat flux in ice can be equated to the atmospheric flux, $F_a = C_T(T_a - T_i(0))$, to find the surface temperature of the ice and then the heat flux through the ice as a function of known variables:

$$F_i = \left(\frac{C_t k_i}{k_i + C_t H}\right)(T_a - T_f). \tag{5.16}$$

However, the relationship obtained from substituting this flux in Eq. 5.14 diverges from observation as ice grows too fast. This can be alleviated by adding consideration for an extra layer of snow insulating the ice from the atmosphere, as illustrated in Fig. 5.7, yielding the following ice growth relationship:

$$\rho_i L \frac{\partial h}{\partial t} = k_i \left(h + \frac{k_i h_s}{k_s} + \frac{k_i}{C_t}\right)^{-1} (T_a - T_f) \tag{5.17}$$

where h_s is the snow depth and k_s is the thermal conductivity of snow (*Maykut*, 1986).

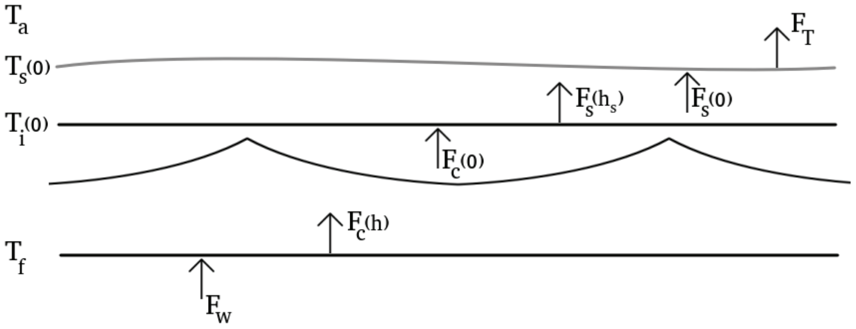

Figure 5.7: Schematic of the different heat fluxes considered to obtain reproduce ice growth as a function of ice thickness when considering snow. The temperature at the bottom of the ice is set to the water freezing point T_f and the air temperature T_a is set. The temperature at the ice surface $T_i(0)$ and snow surface $T_s(0)$ are determined by balancing the fluxes across the boundaries. $F_w = F_c(h)$, $F_c(0) = F_s(h_s)$ and $F_s(0) = F_T$ at the water-ice, ice-snow and snow-air boundaries respectively.

In open waters, ice growth is driven by the direct heat exchange between the atmosphere and ocean. In this case, the ice creation term, as presented in *Pease* (1987), is given by

$$F = -\frac{1}{\rho_i L}\left[\sigma_{SB} e_a T_a^4 - Q_{iu} + \rho_a C_h C_p u_a (T_a - T_w)\right] \tag{5.18}$$

where σ_{SB} is the Stefan-Boltzmann constant, e_a is the emissivity of the air, Q_{iu} the longwave radiation emitted upward by the water, C_h is the sensible heat coefficient and C_p is the specific heat of air.

5.2.5 Revisiting the polynya equilibrium

By combining equations 5.1, 5.9 and 5.13, we can obtain a new form of the polynya balance

$$\frac{dx_p}{dt} = Au_a + Bx_p - x_p \frac{F(u_a, T_a)}{h_{cw}(u_a, x_p)} \tag{5.19}$$

which is dependent on ice drift velocity, frazil collection depth and ice formation, which themselves vary with wind speed, fetch and temperature as shown in Fig. 5.8.

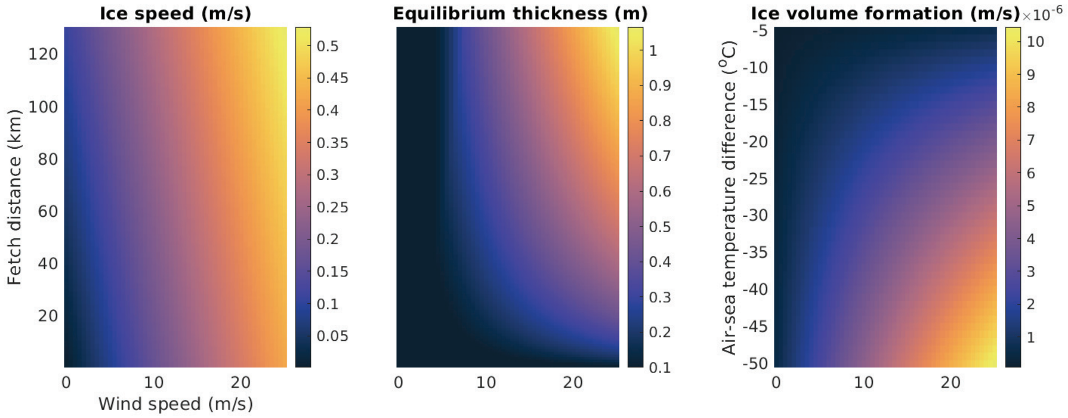

Figure 5.8: Variation of key polynya parameters with wind speed, fetch and air temperature.

This equation can have different forms, depending on the functional form used for the frazil collection depth. At very small fetch values, the ice thickness at the edge is set to a minimum value and, being constant, makes Eq. 5.19 very similar to Eq. 5.1, with solutions exhibiting the same dependence on wind speed and temperature, but smaller values due to the slower drift velocity. For growing waves, the polynya extent equation becomes:

$$\frac{dx_p}{dt} = Au_a + Bx_p - \sqrt{x_p}\frac{F(u_a, Ta)}{Du_a} \tag{5.20}$$

In order to obtain the equilibrium size of the polynya in this case, the equation can be solved for a vanishing derivative, yielding:

$$x_p = \frac{1}{4B^2}\left[\frac{F(u_a, T_a)}{Du_a} \pm \sqrt{\frac{F(u_a, T_a)}{Du_a} - 4BAu_a}\right]^2 \tag{5.21}$$

This solution gives two potential values for the polynya extent, a stable polynya at relatively small fetch, and an unstable one at longer fetch. This can be seen in the central panel of Fig. 5.9, with markedly different equilibrium contours when considering waves.

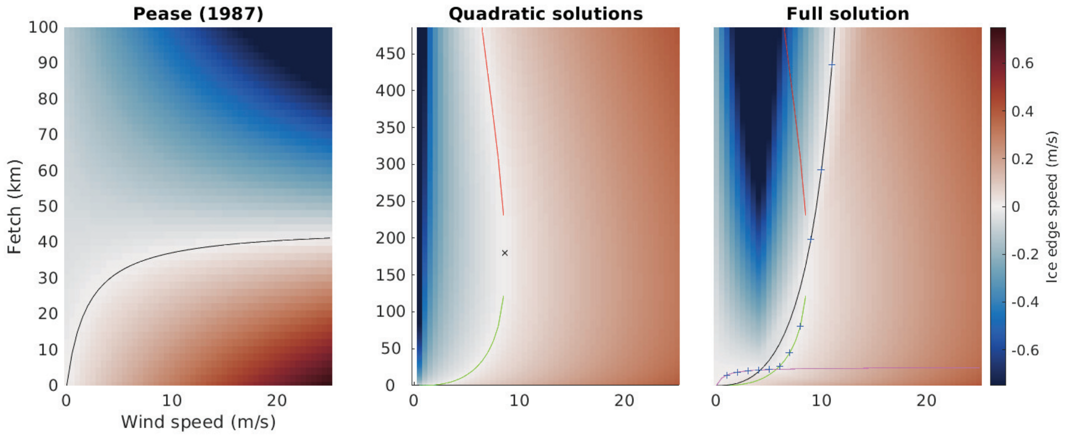

Figure 5.9: Polynya tendency as a function of wind speed and fetch at -10^{o}C. Lines indicate the equilibrium polynya extent, where ice advection and formation are balanced. In the central panel, the green and red lines indicates stable and unstable equilibrium extents, respectively. The black ”x” marks the transition point between the possibility of equilibrium and entirely unstable roots of the quadratic solution. In the right panel, the minimum frazil collection depth solution is added in magenta, the fetch limited solution in black and the blue ”+” identify the composite solution.

If the polynya extends past the necessary distance for waves to grow to their full potential given by Eq. 5.8, the ice equilibrium thickness becomes independent of fetch, as seen in Fig. 5.8. This yields a different form of the tendency equation, with the same dependence on x_p as the original equation in *Pease* (1987):

$$\frac{dx_p}{dt} = Au_a + Bx_p - x_p\frac{F(u_a, Ta)}{h_{cw}(u_a)}. \tag{5.22}$$

The solution can be written as

$$x_p = \frac{\alpha}{\beta}\left(1 - e^{-\beta t}\right) \tag{5.23}$$

where $\alpha = Au_a$ is the wind driven ice velocity component and $\beta = \frac{F(u_a,Ta)}{h_{cw}(u_a)} - B$ represents the opposing effects of the ice creation versus the fetch dependent sea ice drift. With waves attaining their fetch limit, the frazil collection depth also becomes fetch limited, allowing the ice edge to be stable at shorter distances than with the infinitely growing waves in the quadratic solution.

5.3 Results

5.3.1 Polynya extent

Using the different solutions where applicable, the predicted sea ice extent at a given temperature as a function of wind speeds can be obtained. An example is shown in Fig. 5.9 for -10°C. In this case, at wind speeds lower than 8 m s^{-1}, the minimum frazil collection depth solution is applicable, as the wind gets stronger and wave forcing becomes strong enough to compress the ice, the polynya extent rapidly increases following the quadratic solution until waves become fetch limited, leading to a stable solution up to 13 m s^{-1}. At greater wind speed, ice formation is too weak to compensate for the ice drift and the polynya would grow infinitely. For colder temperatures, ice formation increases and stable equilibrium can be achieved for higher winds.

Overall the open water extent with waves, shown in Fig. 5.10, differs in two main ways. The consideration of wave-driven compression of sea ice increases the predicted open water extent at larger wind values for low temperatures. However, for low winds, smaller extents are predicted due to the lower ice drift speed.

Since analytical calculations of the opening time-scale for the three possible forms of the open water extent balance equation (Eq. 5.19) are non-trivial to integrate and obtain a timescale from, a numerical integral of the form:

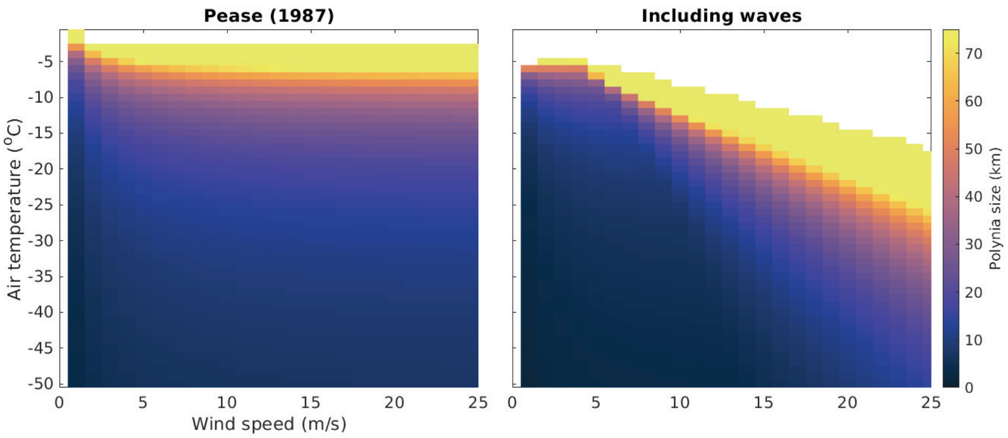

Figure 5.10: Polynya extent as a function of wind speed and air temperature. For the wind-only Pease model (left) the wind contribution to heat fluxes balances the icreased ice drift speed, leading to polynya extent being determined by air temperature past 5 $\mathrm{m/s}$. Including waves (right) causes both faster drift and the formation of thicker ice, more open is thus necessary to balance advection.

$$t_{\mathrm{eq}} = \int_0^{t_{\mathrm{eq}}} dt = \int_0^{x_{\mathrm{eq}}} \left(\frac{dx_p}{dt}\right)^{-1} dx_p \tag{5.24}$$

was performed instead. Because of the piece-wise nature of Eq. 5.13, noticeable jumps can be seen in the integrated time-scale when the frazil collection depth changes from its minimum value to its growing wave value to its fetch limited value. Opening time increases noticeably once ice compression comes into play and decreases when waves become fetch limited. In general, the predicted opening times match the predictions of *Pease* (1987) when the minimum frazil collection depth is used, but are significantly larger once ice compression comes into play.

5.3.2 Thermal implications

Besides the effects of wind and waves, air temperature has several impacts on the predicted ice edge location and on the thickness gradients. Transects of sea ice thickness and associated heat fluxes can be predicted by combining Eqs. 5.13, 5.16 and 5.18:

$$h(x) = h_{cw} + \int_0^{x} \frac{dh}{dt}\left(\frac{dx}{dt}\right)^{-1} dx \tag{5.25}$$

Colder temperatures, by allowing more ice formation per unit area, allow smaller open water extents to be stable. This also reduces the fetch available to the development of

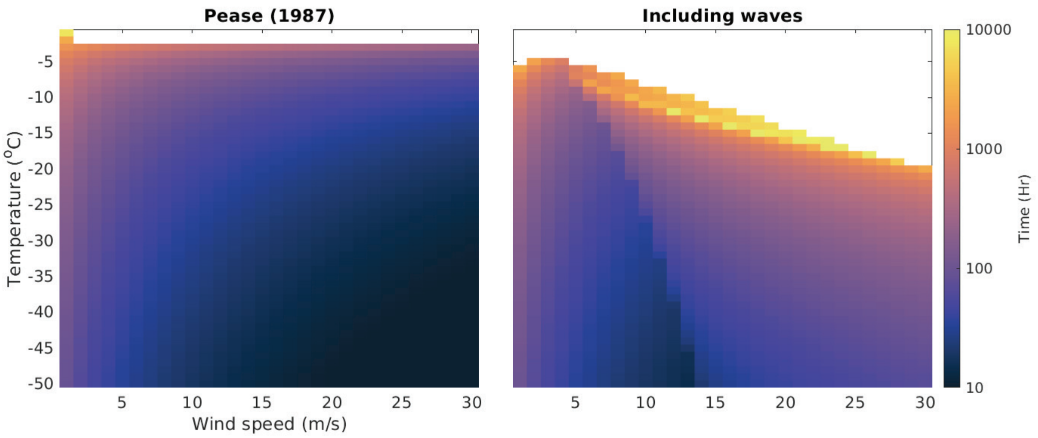

Figure 5.11: Polynya opening time-scale as a function of wind speed and air temperature. Wave effects increase the opening time since the drift is reduced for low fetch and the final extent is larger. Note: color scale is in log format due to the large range of values.

waves and in turn reduces the initial thickness of the ice. This reinforces the stronger heat fluxes already present at lower temperatures due to the temperature difference with the water, considered to be at the sea water freezing point (-1.8°C) and allow larger thickness gradients as shown in Fig. 5.12. In warmer temperatures, larger open water extents allow for larger waves and initially thicker ice, which will then grow slower.

Except for low winds, the equilibrium open water fetch predicted by the Pease model is significantly smaller than what was obtained through the explicit consideration of waves in this study. For a given wind, although the current model predicts slower ice, the inclusion of waves leads to much thicker ice at the edge, requiring a far greater production of frazil to compensate for ice drift.

Calculating thermal fluxes using the formulation described in section 5.2.4, coastal waters would lose heat over a much wider region. In the sea ice, although thicker ice can block heat fluxes more effectively and thus grows slower, the predicted wave-dependent ice drift is also slower. These two effects oppose each other, leading to similar ice thickness gradients between the two models and thicker ice overall.

Combining the open water extent, x_p, and open water heat fluxes, $\rho_i LF$, can give an overview of the total heat lost directly by the ocean to the atmosphere, shown in Fig. 5.13.

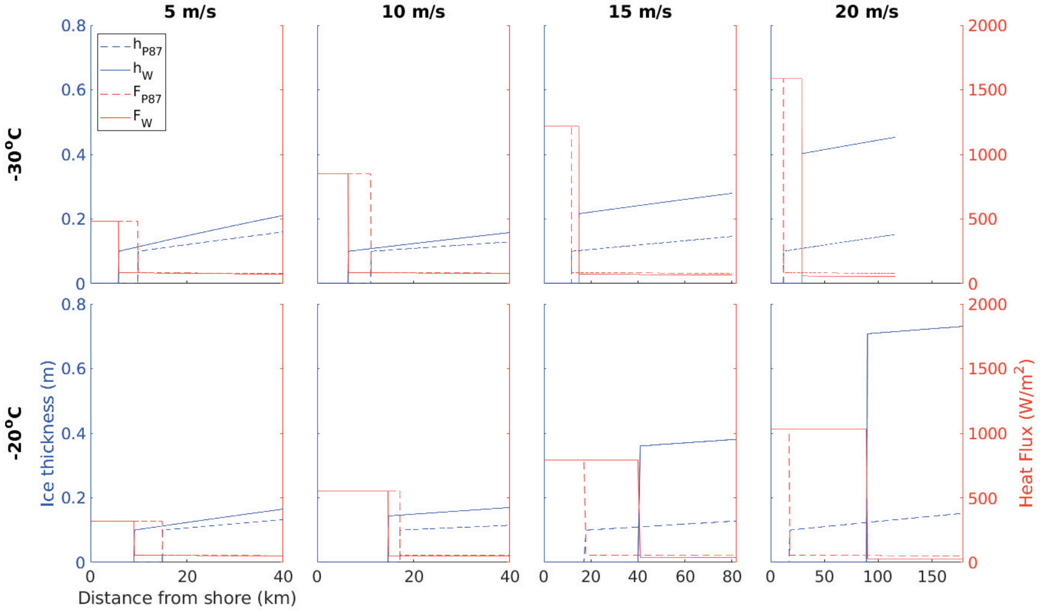

Figure 5.12: Transects of polynyas at $-20°$C for winds of 5 to 20 m s^{-1}. With waves, equilibrium thickness increases with wind speed. Although thick ice reduces heat fluxes and grows slower, predicted ice drift velocities are also slower, leading to ice thickness gradients that differ less than expected.

In this situation, the solution from the Pease model given by Eq. 5.2, yields a total heat flux which is strictly dependent on wind speed. For a given wind speed, a lower temperature causes larger heat fluxes which create more ice and a smaller open water extent in such a way that they exactly balance each other by construction. When considering waves and the ice compaction that they create, this balance does not exist. Larger fetch allows the growth of larger waves and requires the formation of thicker ice, overall increasing the amount of heat extracted from the ocean. This increase is particularly marked at low temperatures and wind speeds above 15 $\mathrm{m\,s^{-1}}$.

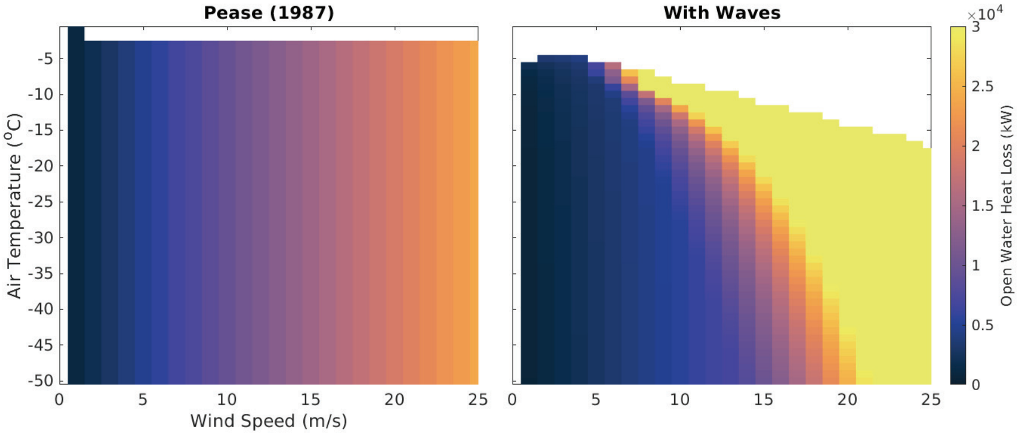

Figure 5.13: Open water heat loss as a function of wind speed and air temperature. By construction, the total heat flux is independent of temperature in the Pease model. The wave driven compaction of the ice causes a further increase of the extent, allowing larger fluxes at low temperature to act over a greater distance.

5.4 Conclusion

Previous chapters of this thesis concentrated on sea ice dynamics and the opposition of wind and wave forcing against ice internal stress. In this chapter, there is no force directly opposing sea ice drift and a new kind of balance is obtained through a simplified consideration of thermodynamics. Despite this important change of context, it is evident that sea ice mechanical properties still have an important role to play.

Of the two changes implemented here to represent the influence of waves, modifications to the ice drift velocity had the least impact. This is not unexpected since the additional wave-driven component of ice drift can be traced back to the wind, much like ocean models often apply wind stress directly on the water without explicitly considering waves. However, in real-world simulations, swell able to propagate from remote locations and impact the ice could have a more significant impact by adding otherwise ignored forcing.

Although their maximum local values might be smaller, wind and current stresses tend to dominate ice drift on larger scales as they apply over a far larger area. However, by applying large local forces, waves can significantly modify the ice thickness near the ice edge, compressing thin ice over large areas into thicker ice on a smaller area. This, in turn, can change the amount of ice formation by exposing more open water where thermodynamic fluxes are much greater. This impact is governed by the frazil collection depth, a variable often considered constant. In *Pease* (1987) it was defined at 10 cm and in the widely used CICE sea ice model (*Hunke et al.*, 2015) it has a default value of 5 cm, despite being shown to vary with wind speed by *Drucker et al.* (2003). The frazil collection depth should depend on surface waves and oceanic processes such as the Stokes drift, the wave radiative stress and Langmuir circulation cells that are all affected by the presence of frazil itself (*Drucker et al.*, 2003). Based on the previous work of *Biggs et al.* (2000) and *Biggs and Willmott* (2004), *Walkington et al.* (2007) presented a parameterization for the frazil collection depth as part of a two-dimensional model of coastal polynyas, but voluntarily neglected the impact of waves, wave-current and wave-ice interactions in an attempt to maintain simple relationships and numerical efficiency. Recently, *Sutherland and Dumont* (2018) proposed an equilibrium model linking the wave radiative stress with the ice thickness near the edge of a polynya, or a marginal ice zone impacted by fetch-limited waves. They showed that the ice thickness necessary to balance wave stresses increases with significant wave height and can reach much larger values than the few centimeters commonly used. Waves and surface currents can also force frazil under established ice of greater thickness *(Dumont, personal communications)*.

Given the large difference shown here for different regimes in the wave growth and the corresponding frazil collection depth, consideration of wave forcing in ice modeling near open waters seems warranted not only for the drift, but also for the possible impact of increased ice thickness on thermodynamics, with ramifications for both ocean and atmosphere models as well. The main focus of this chapter has not been on reproducing exact polynya extents or matching specific observations due to their scarcity and the variations of definitions. For example, two observations of polynyas using Advanced Very High Resolution Radiometer (AVHRR) were reported and compared to polynya extent predictions from the Pease model by *Drucker et al.* (2003). However, the extracted frazil collection thicknesses from remote sensing were 2-3cm at the ice edge. Observed extents were greater than those predicted, even accounting for the smaller frazil collection thickness, but much smaller than the sizes that would be predicted using the model presented here due to the very different definition of the ice edge. It was demonstrated in this chapter that including waves explicitly increased the predicted size of polynyas and the magnitude of the increase can be changed by changing the D parameter in Eq. 5.13. This offers a possible way to resolve the discrepancies reported by *Drucker et al.* (2003). However, much like other parts of this thesis, this chapter is written with the intent to guide the analysis of observations by suggesting relationships rather than directly tuning the model to observation, as the correct extraction of remote sensing variables in order to tune models is a challenge on its own.

CHAPTER 6

DISCUSSION AND CONCLUSIONS

The marginal ice zone (MIZ) is a dynamic, complex and dangerous environment. Historically, studying the MIZ has been done either directly from ships or using moorings and buoys deployed prior to a measurement campaign at locations where interesting conditions were expected in the coming winter. Advances in technologies have opened up numerous new approaches to gather observational data. Simplest amongst them, cheaper sensors have allowed greater spatial coverage by enabling the purchase of a larger number of them. More affordable single use digital instruments with satellite transmission capabilities have increased our capability to make riskier observations such as acceleration or drift from ice floes subjected to waves. Drones are enabling us to see the MIZ from a bird's eye view and image analysis can derive estimates of quantities such as concentration, floe size and ice drift or even ice thickness and wave height from a side-on perspective. Furthermore, the resurgence of ice canoeing as a sport dedicated to navigation in ice infested waters had the beneficial side effect of providing a greater access to in-situ measurements. Simultaneously with this progress on the observational front, numerical modeling for sea ice and waves has reached a point where both are ready to consider the MIZ. Finally, our changing climate, with increasing areas of open water able to support greater wave growth and thinning, more fragile ice, is making understanding the MIZ more relevant than ever.

The work presented here was conceived in this context of increasing capabilities and needs to address two of the main topics in the field of wave-ice interactions and MIZ dynamics. The first is developing our numerical modeling capacity further in order to better simulate sea ice at high resolution, something critical to the study of the relatively short scales typical in the MIZ. The second driver is evaluating the capability of our current theories for waves, ice and their interactions to create waves and sea ice dynamics able to reproduce observations of the MIZ, and where observations are lacking, make predictions to guide further field studies. Indeed, many processes have been put forward to explain parts of the MIZ as a physical system, particularly wave energy attenuation and ice breakup, but few frameworks exist in which to test these proposed theories. This can be achieved by assessing their ability to generate realistic scenarios for wave and sea ice together, rather than simply match steady-states expectations of one variable. Once a set of physics able to adequately describe the evolution of the MIZ is found, further situations can be considered to determine interesting avenues for new research directions. The model developed through this thesis has enabled rapid simulations of a range of wave, wind and ice conditions to highlight the importance of key parameters of wave-ice interactions in the MIZ, such as ice strength and frazil collection depth. While direct observation of these variables may be difficult, the relationships simulated here would also allow indirect measurements.

All of the research presented here has been performed using a one-dimensional model of sea ice and simplified wave dynamics. This was done for multiple reasons. From a practical point of view, it greatly simplifies the derivation and implementation of the AJNK method presented in chapter 2 while still offering a stringent test for the new numerical scheme. It also kept the necessary effort for the integration of a wave component in chapter 3 minimal without compromising the integrity of MIZ processes since they are typically studied in one dimension. The choice of a one-dimensional simple model allowed for modeling experiments to be conducted much more rapidly by running multiple simple, serial models at the same time, making whole experiments trivially parallelizable. Due to the exploratory nature of this work and the focus on sea ice, the wave component of the model was kept fairly minimal. However the impact of waves and attenuation strength are significant enough to have confidence in a generalization of the importance of waves in high resolution sea ice modeling. All of the findings presented here can be extrapolated to the full two-dimensional modeling problem. The results provide guidance for the development of such coupled 2D models as well as an agile alternative for more idealized focused studies.

To begin, developments on the use of Newton's method to solve the sea ice momentum equation as described in *Lemieux et al.* (2010) were investigated in response to the increasing computational cost stemming both normally from the greater resolution as well as the increased difficulty to attain convergence with sharp gradients. In chapter 2, the AJNK method was shown to allow faster convergence to the solution and required fewer iterations of its linear solver than the JFNK method. The reduction in number of iterations for both linear and non-linear solvers, by factors of up to 5 and about 30% respectively, is compounding and has the potential to reduce computational costs when implemented in operational models. Furthermore, the analytical Jacobian changes computations of the Jacobian-vector product required in the linear solver into a simple matrix-vector product compared to the previous finite difference approximation requiring recalculation of the momentum balance twice. Although this has no impact on iteration numbers, it does save operations. It should be noted that increased efficiency offers gains in accuracy when under time constraints, such as when issuing forecasts. The computing time saved can be highly valuable and in turn opens up the possibility of smaller time steps, improving both model stability and the quality of simulations. Creating a solver that combines reliability and efficiency remains a challenge for such a highly nonlinear problem as sea ice dynamics, however this represents a step in the right direction.

Beyond numerical challenges, improving the resolution of sea ice models has also brought into focus the need to develop a better representation of the MIZ. Waves can penetrate tens of kilometers into the ice pack and still impact it (*Wadhams et al.*, 1988). Global or polar models have resolutions of several kilometers (*Dupont et al.*, 2015), meaning that the MIZ can be contained inside a few model grid cells, smoothing all its structure. Even at these resolutions, ice edge localization can be of particular interest, be it for navigation, weather forecasts or other applications such as biogeochemical modeling (*Post et al.*, 2013; *Arrigo et al.*, 2008), and waves can apply strong localized stresses at the ice edge (*Stopa et al.*, 2018), keeping wave-ice interactions relevant. In order to test our ability to reproduce key features of the MIZ, waves were added to the one-dimensional model. Waves and ice were coupled using one of two formulations for wave attenuation by *Kohout and Meylan* (2008) and *Sutherland et al.* (2019) in combination with the wave radiation stress described by *Sutherland and Dumont* (2018). Modifications to the ice strength parameterization were also introduced. Although most forces in the MIZ are still not well understood in detail, the model was able to reproduce key characteristics of the MIZ. This was demonstrated by studying two different phenomena: ice compression near the edge (chap. 3) and the formation of an ice edge jet (chap. 4). Simulations of the ice evolution using the different attenuation and ice strength formulations were then evaluated for their capability to reproduce the final observed thickness profile shapes. These formulations were also used to predict ice edge jet characteristics. The evolution of ice thickness and velocities in the model provides insight into how waves and ice interacted to generate the final results. Key differences were identified between the MIZ characteristics obtained with these formulations, highlighting the kind of observations which could discriminate which formulation is better suited to modeling the MIZ.

The modeling of ice compression by waves and winds in chapter 3 showcased how the typical ice strength used when modeling sea ice at large scales fails in the MIZ. This ice strength is used to scale the resistance of the inner arctic ice pack to deformations. Generally, for shear or compression to occur in the inner ice pack composed of large floes, leads or ridges need to be formed, both energy intensive processes (*Hibler III*, 1977). In the MIZ, smaller floes subjected to waves facilitate ice mobility and rafting (*Sutherland and Dumont*, 2018). This behavior is better represented by rheologies and ice strengths developed for river ice (*Uzuner and Kennedy*, 1976; *Sutherland and Dumont*, 2018). A modification making the sea ice strength closer to that of river ice leads to more realistic ice thickness profiles. The magnitude and localization of the wave radiation stress applied on the ice was also observed to depend strongly on the strength of wave attenuation creating a feedback that could change ice thickness by a factor of two or more. Indeed, stronger attenuation not only extracts more energy from the waves, but also applies stronger stresses closer to the ice edge thus leading to a steeper increase in ice thickness at the ice edge creating thicker ice which attenuates waves more strongly. By opposition, weaker attenuation applies weaker stresses over a wider region and causes a more gradual increase in thickness. This could enhance the importance of other factors that influence wave attenuation such as floe size or the presence of frazil or grease ice under the visible ice floes in the MIZ.

Building upon the study of the effects of wave attenuation and wave radiation stress in the direction perpendicular to the ice edge, chapter 4 includes forcings and ice velocity in the direction parallel to the ice edge. Near the ice edge, a region of high sea ice velocities, a jet, has been observed (e.g. *Johannessen et al.* (1983); *Smith and Bird* (1991); *Dai et al.* (2019)). In the simulations, the strength of the wave attenuation was found to be the most determinant factor in jet characteristics. Stronger attenuation produced both faster and wider jets. Ice strength was a secondary factor. Stronger ice could better resist compression and lead to thinner ice less capable of attenuating waves and thus supplying energy over a wider area which in turn caused weaker but wider jets. Perhaps counter-intuitively, stronger ice also caused lower internal shear stresses near the ice edge due to weaker velocity gradients more than compensating for the stronger shear strength. Finally, the incident angle of the winds and waves had less impact than the attenuation or ice strength. When an effect was observed, wind angle variations made jets either narrow and fast or wide and slow, for angles more parallel or perpendicular to the ice edge, respectively. Depending on conditions, predictions of the ice edge jet width vary from 100m to near 1km, with maximum velocities of 40 to 50 cm/s, relatively large velocities for sea ice. Given that wave attenuation and ice strength are the two primary drivers of the variations in jet velocity and width, comparisons with observations of the ice edge jet velocities transects would be a great opportunity to test our current dynamical model of the MIZ using image analysis of drone footage rather than hazardous and effort intensive measurements of thickness.

Since waves and ice evolve in tandem, proper integration of both model components is necessary when testing models against realistic observations. Over the course of the few days necessary for waves and ice to achieve a steady state over the modeled domain, ice conditions changed significantly and the conditions in the MIZ would likely do so as well. Considering how ice impacts waves or vice-versa without their full interactions would lead to very different results. As such, building further on the coupled model presented here and testing the ability of MIZ descriptions to reproduce time-varying observations of the MIZ would be beneficial.

As demonstrated here, the components necessary to numerically model the MIZ are available. An implementation of this coupled system using operational, two-dimensional numerical models of waves and ice would be highly desirable. This would enable the consideration of realistic cases, including topography, realistic forcings and wave evolution with a full two-dimensional spectrum and multiple wave source terms. Such a system could be used to study rapid ice movement in areas such as the east coasts of Greenland, Labrador or Newfoundland or within the Estuary and Gulf of St. Lawrence and offer tangible improvements in ice forecasting and case study capabilities. Using the sea ice drift velocities predicted from the model developed here and integrating a dependence of ice thickness on waves as derived by *Sutherland and Dumont* (2018), it was possible to demonstrate how considering waves can change both open water areas and ice thickness. This, in turn, affects air-sea fluxes and ice production, two critical but elusive variables for both weather and ocean modeling (*Pellerin et al.*, 2004; *Urrego-Blanco and Sheng*, 2014). Linking the frazil collection depth to the equilibrium MIZ ice thickness changed the extent of open waters from being essentially constant with wind speeds at higher wind speeds to increasing quadratically. The lack of variation at higher wind speeds stemmed from compensating increases in heat fluxes and drift velocities in previous models such as the one described by *Pease* (1987). The new quadratic dependence at higher wind speed is akin to the one found by *Biggs et al.* (2000), although it stems from wave effects on the frazil collection depth instead of winds and currents stresses. This departure from previous models could allow them to be discriminated by observations under a range of conditions.

Implementation of the AJNK method or the wave-ice interactions described here in 2D models each would come with their own challenge. The main one is the technical complexity of implementing new numerical methods in a parallel model. Forming the Jacobian of the momentum equation requires global knowledge of the variables. With the typical method of parallelization for models being to break the domain into sub-domains, this can increase the amount of communication required and diminish the gains provided by the method. However, a Jacobian-free version of Newton's method has been used for a parallel sea ice model previously by *Losch et al.* (2014) and it is expected that using the analytical Jacobian would improve its local convergence. In the context of wave-ice interactions, using a 2D model would require coupling in a different manner, as running the sea ice model at the same time step as the wave model would increase the computational cost unreasonably. However, since ice tends to move and change much slower than waves, this should not be a problem unless a very high temporal accuracy is desired for waves. Shear in a 2D model would become significantly more important with leads becoming possible and other features such as instabilities in the ice edge jet could be studied. The results presented here can be considered averages since 2D structures such as eddies cannot be modeled. With eddies, variables such as ice thickness would no longer be restricted to increasing monotonically as thinner ice could be carried towards the inner ice pack and thicker ice towards the edge. This, in turn, would change wave attenuation and thus the forcing applied. While the 1D model used here simplified the situation and made it easier to study specific interactions, a 2D model would allow more direct comparisons with observations and also be fit for use in a forecasting system.

From a theoretical point of view, a potential follow-up would be to gather further observations in the MIZ, especially as the ice is adjusting to changing conditions. Such observations would open up possibilities to further challenge our current understanding of the MIZ. Given the abundance of competing theories, particularly for wave attenuation and ice rheology, attempting to reproduce key observed features of the MIZ in models could play a pivotal role in discriminating which formulation to use and in identifying possible compensating errors. Wave energy measurements both in open water and within the ice have been a staple of MIZ field studies and remain highly desirable. However, much more is needed in order to properly quantify all of the variables on which wave attenuation depends. Certain variables such as floe size and ice concentration should become much more widely accessible thanks to drone studies and image processing and the increasing resolution of satellite imagery. Field studies can also provide many more useful variables such as thickness of frazil under the ice, under ice turbulence and even brine content and ice temperature. Additionally, ice thickness profiles starting from the ice edge can be distinctly useful in validating models. Unfortunately, they are particularly difficult to obtain, especially in the very conditions for which they would be desirable: under the influence of sizeable waves. Finally, satellite remote sensing has the potential to provide many, if not all, of the sought-after variables on a scale that is very appropriate for model development. Defining the rheology of ice requires knowledge of deformations, which can be extracted by feature tracking, and forcing, which can be obtained from wind and open water wave data. Although it is more complex, wave energy in ice and ice thickness can also be derived. Both in-situ and remote observations can be leveraged to improve our understanding of the MIZ. Even though thickness measurements can be difficult to acquire either way, both kinds of data sets are well suited to building upon the ice edge jet simulations presented within and use ice drift as a new, much more accessible variable.

Validation of wave attenuation theories typically uses ice characteristics and open water waves observations to predict attenuation and energy to be compared with wave energy profiles. Another way, as used by *Sutherland and Dumont* (2018), is to go from wave energy profiles to opposing the wave radiation stress and ice strength and then obtaining ice thickness profiles to be compared with observations. Both of these methods not only require these precious thickness profiles, but also that waves be propagating perpendicularly to the ice edge to avoid complications. The ice edge jet, by its very nature, requires anything but this special alignment between the wave propagation direction and the ice edge. Ice drift in the ice edge jet can also be deduced from image or video analysis and does not require presence in the MIZ, making it much easier to obtain. Jet characteristics can, however, be calculated from wave forcing as described here. As such, observations and model predictions of movement at the ice edge, either in compression or as a jet parallel to the edge, or both, could be an easier means to evaluate our understanding of wave-ice interactions and ability to simulate the MIZ by keeping ice thickness as an intermediate variable instead.

The development of a complete coupled wave-ice model and of a greater observational capability work in tandem by providing us with a better way to describe and simulate the MIZ as a physical system as well as widening the range of possible comparisons. Therefore, gathering ice movement observations close to the ice edge, particularly in the accessible seasonal laboratories that are the Estuary and Gulf of St. Lawrence, and continuing model development to be applied there and in similar environments are the logical steps following this project in our quest for a greater understanding of MIZ dynamics and wave-ice interactions.

BIBLIOGRAPHY

Arakawa, A., and V. R. Lamb, Computational design of the basic dynamical processes of the UCLA general circulation model, *Methods in Computational Physics*, *17*, 173–265, 1977.

Ardhuin, F., G. Boutin, J. Stopa, F. Girard-Ardhuin, C. Melsheimer, J. Thomson, A. Kohout, M. Doble, and P. Wadhams, Wave attenuation through an arctic marginal ice zone on October 12, 2015: 2. Numerical modeling of waves and associated ice break-up, *Journal of Geophysical Research: Oceans*, *123*, 5652–5668, 2018.

Arrigo, K. R., G. van Dijken, and S. Pabi, Impact of a shrinking Arctic ice cover on marine primary production, *Geophysical Research Letters*, *35*, 2008.

Auclair, J.-P., J.-F. Lemieux, L. B. Tremblay, and H. Ritchie, Implementation of Newton's method with an analytical Jacobian to solve the 1D sea ice momentum equation, *Journal of Computational Physics*, *340*, 69–84, 2017.

Baudry, J., D. Dumont, U. Neumeier, and P. Sutherland, Propagation and attenuation of short waves in the marginal ice zone, *InPrep*, 2021.

Bennetts, L., and V. Squire, Model sensitivity analysis of scattering-induced attenuation of ice-coupled waves, *Ocean Modelling*, *45*, 1–13, 2012a.

Bennetts, L. G., and V. A. Squire, On the calculation of an attenuation coefficient for transects of ice-covered ocean, *Proceedings of the Royal Society A: Mathematical, Physical and Engineering Sciences*, *468*, 136–162, 2012b.

Bernier, N. B., J.-H. G. Alves, H. Tolman, A. Chawla, S. Peel, B. Pouliot, J.-M. Bélanger, P. Pellerin, M. Lépine, and M. Roch, Operational wave prediction system at Environment Canada: Going global to improve regional forecast skill, *Weather and Forecasting*, *31*, 353–370, 2016.

Biggs, N. R., and A. J. Willmott, Unsteady polynya flux model solutions incorporating a parameterization for the collection thickness of consolidated new ice, *Ocean Modelling*, *7*, 343–361, 2004.

Biggs, N. R., M. A. M. MAQUEDA, and A. J. Willmott, Polynya flux model solutions incorporating a parameterization for the collection thickness of consolidated new ice, *Journal of Fluid Mechanics*, *408*, 179–204, 2000.

Bouchat, A., and L. B. Tremblay, Energy dissipation in viscous-plastic sea-ice models, *Journal of Geophysical Research: Oceans*, *119*, 976–994, 2014.

Bouillon, S., T. Fichefet, V. Legat, and G. Madec, The elastic- viscous–plastic method revisited, *Ocean Modelling*, *71*, 2–12, 2013.

Boutin, G., F. Ardhuin, D. Dumont, C. Sévigny, F. Girard-Ardhuin, and M. Accensi, Floe size effect on wave-ice interactions: Possible effects, implementation in wave model, and evaluation, *Journal of Geophysical Research: Oceans*, *123*, 4779–4805, 2018.

Bouws, E., L. Draper, E. Shearman, A. Laing, D. Feit, W. Mass, L. Eide, P. Francis, D. Carter, and J. Battjes, *Guide to Wave Analysis and Forecasting. WMO-No. 702*, World Meteorological Organization, 1998.

Bowyer, P., and A. MacAfee, The theory of trapped-fetch waves with tropical cyclones - an operational perspective, *Weather Forecasting*, *20*, 229–244, 2005.

Budgell, W., Numerical simulation of ice-ocean variability in the Barents Sea region, *Ocean Dynamics*, *55*, 370–387, 2005.

Chikhar, K., J.-F. Lemieux, F. Dupont, F. Roy, G. C. Smith, M. Brady, S. E. Howell, and R. Beaini, Sensitivity of ice drift to form drag and ice strength parameterization in a coupled ice–ocean model, *Atmosphere-Ocean*, pp. 1–21, 2019.

Coon, M., G. Maykut, and R. Pritchard, Modeling the pack ice as an elastic-plastic material, *AIDJEX Bulletin*, *24*, 1–105, 1974.

Dai, H.-J., J. C. McWilliams, and J.-H. Liang, Wave-driven mesoscale currents in a marginal ice zone, *Ocean Modelling*, 2019.

Dai, M., H. H. Shen, M. A. Hopkins, and S. F. Ackley, Wave rafting and the equilibrium pancake ice cover thickness, *Journal of Geophysical Research: Oceans*, *109*, 2004.

Drucker, R., S. Martin, and R. Moritz, Observations of ice thickness and frazil ice in the St. Lawrence Island polynya from satellite imagery, upward looking sonar, and salinity/temperature moorings, *Journal of Geophysical Research: Oceans*, *108*, 2003.

Dumont, D., Y. Gratton, and T. E. Arbetter, Modeling the dynamics of the north water polynya ice bridge, *Journal of Physical Oceanography*, *39*, 1448–1461, 2009.

Dumont, D., A. Kohout, and L. Bertino, A wave-based model for the marginal ice zone including a floe breaking parameterization, *Journal of Geophysical Research: Oceans*, *116*, 2011.

Dupont, F., S. Higginson, R. Bourdallé-Badie, Y. Lu, F. Roy, G. Smith, J.-F. Lemieux, G. Garric, and F. Davidson, A high-resolution ocean and sea-ice modelling system for the Arctic and North Atlantic Oceans, *Geoscientific Model Development*, *8*, 1577–1594, 2015.

Eisenstat, S. C., and H. F. Walker, Globally convergent inexact newton methods, *SIAM Journal on Optimization*, *4*, 393–422, 1994.

Eisenstat, S. C., and H. F. Walker, Choosing the forcing terms in an inexact Newton method, *SIAM Journal on Scientific Computing*, *17*, 16–32, 1996.

Flato, G. M., and W. D. Hibler III, Ridging and strength in modeling the thickness distribution of arctic sea ice, *Journal of Geophysical Research: Oceans*, *100*, 18611–18626, 1995.

Francis, J. A., and S. J. Vavrus, Evidence linking Arctic amplification to extreme weather in mid-latitudes, *Geophysical Research Letters*, *39*, 2012.

Girard, L., J. Weiss, J.-M. Molines, B. Barnier, and S. Bouillon, Evaluation of high-resolution sea ice models on the basis of statistical and scaling properties of Arctic sea ice drift and deformation, *Journal of Geophysical Research: Oceans*, *114*, 2009.

Girard, L., S. Bouillon, J. Weiss, D. Amitrano, T. Fichefet, and V. Legat, A new modeling framework for sea-ice mechanics based on elasto-brittle rheology, *Annals of Glaciology*, *52*, 123–132, 2011.

Godoy, W. F., and X. Liu, Parallel Jacobian-free Newton Krylov solution of the discrete ordinates method with flux limiters for 3D radiative transfer, *Journal of Computational Physics*, *231*, 4257–4278, 2012.

Häkkinen, S., Coupled ice-ocean dynamics in the marginal ice zones: Upwelling/downwelling and eddy generation, *Journal of Geophysical Research: Oceans*, *91*, 819–832, 1986.

Hasselmann, K. F., T. P. Barnett, E. Bouws, H. Carlson, D. E. Cartwright, K. Eake, J. Euring, A. Gicnapp, D. Hasselmann, P. Kruseman, et al., Measurements of wind-wave growth and swell decay during the joint north sea wave project (jonswap)., *Ergaenzungsheft zur Deutschen Hydrographischen Zeitschrift, Reihe A*, 1973.

Herman, A., Wave-induced surge motion and collisions of sea ice floes: Finite-floe-size effects, *Journal of Geophysical Research: Oceans*, *123*, 7472–7494, 2018.

Hibler III, W. D., A viscous sea ice law as a stochastic average of plasticity, *Journal of Geophysical Research*, *82*, 3932–3938, 1977.

Hibler III, W. D., A dynamic thermodynamic sea ice model, *Journal of Physical Oceanography*, *9*, 815–846, 1979.

Hibler III, W. D., Modeling a variable thickness sea ice cover, *Monthly weather review*, *108*, 1943–1973, 1980.

Hibler III, W. D., and K. Bryan, A diagnostic ice-ocean model, *Journal of Physical Oceanography*, *17*, 987–1015, 1987.

Hunke, E., and J. Dukowicz, An elastic-viscous-plastic model for sea ice dynamics, *Journal of Physical Oceanography*, *27*, 1849–1867, 1997.

Hunke, E., D. Notz, A. Turner, and M. Vancoppenolle, The multiphase physics of sea ice: a review for model developers, *The Cryosphere*, *5*, 989, 2011.

Hunke, E. C., Viscous–plastic sea ice dynamics with the EVP model: linearization issues, *Journal of Computational Physics*, *170*, 18–38, 2001.

Hunke, E. C., W. H. Lipscomb, A. K. Turner, N. Jeffery, and S. Elliott, *CICE: the Los Alamos Sea Ice Model Documentation and Software User's Manual*, Los Alamos National Laboratory, Los Alamos NM 87545, 5.1 ed., 2015.

Hutchings, J., and I. Rigor, Role of ice dynamics in anomalous ice conditions in the Beaufort Sea during 2006 and 2007, *Journal of Geophysical Research: Oceans*, *117*, 2012.

Hutchings, J. K., H. Jasak, and S. W. Laxon, A strength implicit correction scheme for the viscous-plastic sea ice model, *Ocean Modelling*, *7*, 111–133, 2004.

Ip, C. F., W. D. Hibler III, and G. M. Flato, On the effect of rheology on seasonal sea-ice simulations, *Annals of Glaciology*, *15*, 17–25, 1991.

Jaiser, R., K. Dethloff, and D. Handorf, Stratospheric response to arctic sea ice retreat and associated planetary wave propagation changes, *Tellus A: Dynamic Meteorology and Oceanography*, *65*, 19375, 2013.

Johannessen, O. M., J. A. Johannessen, J. Morison, B. A. Farrelly, and E. A. S. Svendsen, Oceanographic conditions in the marginal ice zone north of Svalbard in early fall 1979 with an emphasis on mesoscale processes, *Journal of Geophysical Research: Oceans*, *88*, 2755–2769, 1983.

Kahma, K. K., and C. J. Calkoen, Reconciling discrepancies in the observed growth of wind-generated waves, *Journal of Physical Oceanography*, *22*, 1389–1405, 1992.

Kim, B.-M., S.-W. Son, S.-K. Min, J.-H. Jeong, S.-J. Kim, X. Zhang, T. Shim, and J.-H. Yoon, Weakening of the stratospheric polar vortex by arctic sea-ice loss, *Nature communications*, *5*, 1–8, 2014.

Kimmritz, M., S. Danilov, and M. Losch, On the convergence of the modified elastic-viscous–plastic method for solving the sea ice momentum equation, *Journal of Computational Physics*, *296*, 90–100, 2015.

Kimmritz, M., S. Danilov, and M. Losch, The adaptive EVP method for solving the sea ice momentum equation, *Ocean Modelling*, *101*, 59–67, 2016.

Knoll, D. A., and D. E. Keyes, Jacobian-free Newton–Krylov methods: a survey of approaches and applications, *Journal of Computational Physics*, *193*, 357–397, 2004.

Kohout, A., and M. Meylan, An elastic plate model for wave attenuation and ice floe breaking in the marginal ice zone, *Journal of Geophysical Research: Oceans*, *113*, 2008.

König Beatty, C., and D. M. Holland, Modeling landfast sea ice by adding tensile strength, *Journal of Physical Oceanography*, *40*, 185–198, 2010.

Kreyscher, M., M. Harder, P. Lemke, and G. M. Flato, Results of the sea ice model intercomparison project: Evaluation of sea ice rheology schemes for use in climate simulations, *Journal of Geophysical Research: Oceans*, *105*, 11299–11320, 2000.

Kushner, P. J., L. R. Mudryk, W. Merryfield, J. T. Ambadan, A. Berg, A. Bichet, R. Brown, C. Derksen, S. J. Déry, A. Dirkson, G. Flato, C. G. Fletcher, J. C. Fyfe, N. Gillett, C. Haas, S. Howell, F. Laliberté, K. McCusker, M. Sigmond, R. Sospedra-Alfonso, N. F. Tandon, C. Thackeray, L. B. Tremblay, and F. W. Zwiers, Canadian snow and sea ice: assessment of snow, sea ice, and related climate processes in Canada's earth system model and climate-prediction system, *The Cryosphere*, *12*, 1137–1156, 2018.

Kwok, R., E. Hunke, W. Maslowski, D. Menemenlis, and J. Zhang, Variability of sea ice simulations assessed with RGPS kinematics, *Journal of Geophysical Research: Oceans*, *113*, 2008.

Langhorne, P. J., V. A. Squire, C. Fox, and T. G. Haskell, Break-up of sea ice by ocean waves, *Annals of Glaciology*, *27*, 438–442, 1998.

Lax, P., and B. Wendroff, Systems of conservation laws., *Communications on Pure and Applied Mathematics*, *13*, 1960.

Lebedev, V., Maximum size of a wind-generated lead during sea freezing, *Oceanology*, *8*, 313–318, 1968.

Lemieux, J.-F., and L. B. Tremblay, Numerical convergence of viscous-plastic sea ice models, *Journal of Geophysical Research: Oceans (1978–2012)*, *114*, 14, 2009.

Lemieux, J.-F., L. B. Tremblay, S. Thomas, J. Sedláček, and L. A. Mysak, Using the preconditioned Generalized Minimum RESidual (GMRES) method to solve the sea-ice momentum equation, *Journal of Geophysical Research: Oceans (1978–2012)*, *113*, 12, 2008.

Lemieux, J.-F., L. B. Tremblay, J. Sedláček, P. Tupper, S. Thomas, D. Huard, and J.-P. Auclair, Improving the numerical convergence of viscous-plastic sea ice models with the Jacobian-free Newton–Krylov method, *Journal of Computational Physics*, *229*, 2840–2852, 2010.

Lemieux, J.-F., D. A. Knoll, L. B. Tremblay, D. M. Holland, and M. Losch, A comparison of the Jacobian-free Newton–Krylov method and the EVP model for solving the sea ice momentum equation with a viscous-plastic formulation: A serial algorithm study, *Journal of Computational Physics*, *231*, 5926–5944, 2012.

Lemieux, J.-F., D. Knoll, M. Losch, and C. Girard, A second-order accurate in time IMplicit-EXplicit (IMEX) integration scheme for sea ice dynamics, *Journal of Computational Physics*, *263*, 375–392, 2014.

Lemieux, J.-F., L. B. Tremblay, F. Dupont, M. Plante, G. C. Smith, and D. Dumont, A basal stress parameterization for modeling landfast ice, *Journal of Geophysical Research: Oceans*, *120*, 3157–3173, 2015.

Leppäranta, M., and W. D. Hibler III, The role of plastic ice interaction in marginal ice zone dynamics, *Journal of Geophysical Research: Oceans*, *90*, 11899–11909, 1985.

Lindsay, R., J. Zhang, and D. Rothrock, Sea-ice deformation rates from satellite measurements and in a model, *Atmosphere-ocean*, *41*, 35–47, 2003.

Lipscomb, W. H., E. C. Hunke, W. Maslowski, and J. Jakacki, Ridging, strength, and stability in high-resolution sea ice models, *Journal of Geophysical Research*, *112*, 18, 2007.

Liu, A., and E. Mollo-Christensen, Wave propagation in a solid ice pack, *Journal of Physical Oceanograpy*, *18*, 1702–1712, 1988.

Liu, A. K., B. Holt, and P. W. Vachon, Wave propagation in the marginal ice zone: Model predictions and comparisons with buoy and synthetic aperture radar data, *Journal of Geophysical Research: Oceans*, *96*, 4605–4621, 1991.

Liu, A. K., S. Häkkinen, and C. Y. Peng, Wave effects on ocean-ice interaction in the marginal ice zone, *Journal of Geophysical Research: Oceans*, *98*, 10025–10036, 1993.

Liu, J., J. A. Curry, H. Wang, M. Song, and R. M. Horton, Impact of declining Arctic sea ice on winter snowfall, *Proceedings of the National Academy of Sciences*, *109*, 4074–4079, 2012.

Longuet-Higgins, M. S., The mean forces exerted by waves on floating or submerged bodies with applications to sand bars and wave power machines, *Proceedings of the Royal Society of London*, *352*, 463–480, 1977.

Longuet-Higgins, M. S., and R. Stewart, Radiation stresses in water waves; a physical discussion, with applications, *Deep Sea Research and Oceanographic Abstracts*, *11*, 529–562, 1964.

Losch, M., and S. Danilov, On solving the momentum equations of dynamic sea ice models with implicit solvers and the elastic–viscous–plastic technique, *Ocean Modelling*, *41*, 42–52, 2012.

Losch, M., D. Menemenlis, J.-M. Campin, P. Heimbach, and C. Hill, On the formulation of sea-ice models. Part 1: Effects of different solver implementations and parameterizations, *Ocean Modelling*, *33*, 129–144, 2010.

Losch, M., A. Fuchs, J.-F. Lemieux, and A. Vanselow, A parallel Jacobian-free Newton–Krylov solver for a coupled sea ice-ocean model, *Journal of Computational Physics*, *257*, 901–911, 2014.

Lu, Y., S. Higginson, S. Nudds, S. Prinsenberg, and G. Garric, Model simulated volume fluxes through the Canadian Arctic Archipelago and Davis Strait: Linking monthly variations to forcing in different seasons, *Journal of Geophysical Research: Oceans*, *119*, 1927–1942, 2014.

Lund, B., H. C. Graber, P. Persson, M. Smith, M. Doble, J. Thomson, and P. Wadhams, Arctic sea ice drift measured by shipboard marine radar, *Journal of Geophysical Research: Oceans*, *123*, 4298–4321, 2018.

Lüpkes, C., T. Vihma, G. Birnbaum, and U. Wacker, Influence of leads in sea ice on the temperature of the atmospheric boundary layer during polar night, *Geophysical Research Letters*, *35*, 2008.

Manucharyan, G. E., and A. F. Thompson, Submesoscale sea ice-ocean interactions in marginal ice zones, *Journal of Geophysical Research: Oceans*, *122*, 9455–9475, 2017.

Maykut, G. A., The surface heat and mass balance, in *The geophysics of sea ice*, pp. 395–463, Springer, 1986.

McPhee, M., Ice-ocean momentum transfer for the AIDJEX ice model, *Aidjex Bull*, *29*, 93–111, 1975.

McPhee, M., R. Kwok, R. Robins, and M. Coon, Upwelling of Arctic pycnocline associated with shear motion of sea ice, *Geophysical research letters*, *32*, 2005.

McPhee, M. G., G. A. Maykut, and J. H. Morison, Dynamics and thermodynamics of the ice/upper ocean system in the marginal ice zone of the Greenland Sea, *Journal of Geophysical Research: Oceans*, *92*, 7017–7031, 1987.

Mehlmann, C., and T. Richter, A modified global Newton solver for viscous-plastic sea ice models, *Ocean Modelling*, 2017.

Meier, W. N., J. Stroeve, and F. Fetterer, Whither arctic sea ice? A clear signal of decline regionally, seasonally and extending beyond the satellite record, *Annals of Glaciology*, *46*, 428–434, 2007.

Morales Maqueda, M., A. Willmott, and N. Biggs, Polynya dynamics: A review of observations and modeling, *Reviews of Geophysics*, *42*, 2004.

Notz, D., A. Jahn, M. Holland, E. Hunke, F. Massonnet, J. Stroeve, L. B. Tremblay, and M. Vancoppenolle, The CMIP6 Sea-Ice Model Intercomparison Project (SIMIP): Understanding sea ice through climate-model simulations, *Geoscientific Model Development*, *9*, 3427–3446, 2016.

Pease, C. H., The size of wind-driven coastal polynyas, *Journal of Geophysical Research: Oceans*, *92*, 7049–7059, 1987.

Pellerin, P., H. Ritchie, F. J. Saucier, F. Roy, S. Desjardins, M. Valin, and V. Lee, Impact of a two-way coupling between an atmospheric and an ocean-ice model over the Gulf of St. Lawrence, *Monthly Weather Review*, *132*, 1379–1398, 2004.

Perrie, W., and Y. Hu, Air–ice–ocean momentum exchange. Part i: Energy transfer between waves and ice floes, *Journal of physical oceanography*, *26*, 1705–1720, 1996.

Perrie, W., and Y. Hu, Air–ice–ocean momentum exchange. Part II: Ice drift, *Journal of physical oceanography*, *27*, 1976–1996, 1997.

Pierson, W. J., and L. Moskowitz, A proposed spectral form for fully developed wind seas based on the similarity theory of SA Kitaigorodskii, *Journal of geophysical research*, *69*, 5181–5190, 1964.

Post, E., U. S. Bhatt, C. M. Bitz, J. F. Brodie, T. L. Fulton, M. Hebblewhite, J. Kerby, S. J. Kutz, I. Stirling, and D. A. Walker, Ecological consequences of sea-ice decline, *Science*, *341*, 519–524, 2013.

Rampal, P., S. Bouillon, E. Ólason, and M. Morlighem, neXtSIM: A new lagrangian sea ice model, *The Cryosphere*, *10*, 1055–1073, 2016.

Robin, G. d. Q., Wave propagation through fields of pack ice, *Philosophical Transactions of the Royal Society of London. Series A, Mathematical and Physical Sciences*, *255*, 313–339, 1963.

Røed, L. P., and J. J. O'Brien, A coupled ice-ocean model of upwelling in the marginal ice zone, *Journal of Geophysical Research: Oceans*, *88*, 2863–2872, 1983.

Rothrock, D. A., The energetics of the plastic deformation of pack ice by ridging, *Journal of Geophysical Research*, *80*, 4514–4519, 1975a.

Rothrock, D. A., The mechanical behavior of pack ice, *Annual Review of Earth and Planetary Sciences*, *3*, 317–342, 1975b.

Saad, Y., A flexible inner-outer preconditioned GMRES algorithm, *SIAM Journal on Scientific Computing*, *14*, 461–469, 1993.

Saucier, F. J., F. Roy, D. Gilbert, P. Pellerin, and H. Ritchie, Modeling the formation and circulation processes of water masses and sea ice in the Gulf of St. Lawrence, Canada, *Journal of Geophysical Research: Oceans*, *108*, 2003.

Schreyer, H., D. Sulsky, L. Munday, M. Coon, and R. Kwok, Elastic-decohesive constitutive model for sea ice, *Journal of Geophysical Research: Oceans*, *111*, 2006.

Screen, J. A., and I. Simmonds, The central role of diminishing sea ice in recent Arctic temperature amplification, *Nature*, *464*, 1334–1337, 2010.

Sedlacek, J., J.-F. Lemieux, L. A. Mysak, L. B. Tremblay, and D. M. Holland, The granular sea ice model in spherical coordinates and its application to a global climate model, *Journal of Climate*, *20*, 5946–5961, 2007.

Seierstad, I. A., and J. Bader, Impact of a projected future Arctic sea ice reduction on extratropical storminess and the nao, *Climate dynamics*, *33*, 937–943, 2009.

Seinen, C., and B. Khouider, Improving the jacobian free newton-krylov method for the viscous-plastic sea ice momentum equation, *Physica D: Nonlinear Phenomena*, 2017.

Shen, H. H., S. F. Ackley, and M. A. Hopkins, A conceptual model for pancake-ice formation in a wave field, *Annals of Glaciology*, *33*, 361–367, 2001.

Smith, D. C., and A. A. Bird, The interaction of an ocean eddy with an ice edge ocean jet in a marginal ice zone, *Journal of Geophysical Research: Oceans*, *96*, 4675–4689, 1991.

Smith, G. C., F. Roy, and B. Brasnett, Evaluation of an operational ice–ocean analysis and forecasting system for the Gulf of St. Lawrence, *Quarterly Journal of the Royal Meteorological Society*, *139*, 419–433, 2013.

Squire, V. A., The breakup of shore fast sea ice, *Cold Regions Science and Technology*, *21*, 211–218, 1993.

Squire, V. A., Ocean wave interactions with sea ice: a reappraisal, *Annual Review of Fluid Mechanics*, *52*, 2020.

Stopa, J. E., P. Sutherland, and F. Ardhuin, Strong and highly variable push of ocean waves on southern ocean sea ice, *Proceedings of the National Academy of Sciences*, *115*, 5861–5865, 2018.

Sutherland, G., and J. Rabault, Observations of wave dispersion and attenuation in landfast ice, *Journal of Geophysical Research: Oceans*, *121*, 1984–1997, 2016.

Sutherland, G., J. Rabault, K. H. Christensen, and A. Jensen, A two layer model for wave dissipation in sea ice, *Applied Ocean Research*, *88*, 111–118, 2019.

Sutherland, P., and D. Dumont, Marginal ice zone thickness and extent due to wave radiation stress, *Journal of Physical Oceanography*, *48*, 1885–1901, 2018.

Sweby, P. K., High resolution schemes using flux limiters for hyperbolic conservation laws, *SIAM journal on numerical analysis*, *21*, 995–1011, 1984.

Thomson, J., J. Gemmrich, W. E. Rogers, C. O. Collins, and F. Ardhuin, Wave groups observed in pancake sea ice, *Journal of Geophysical Research: Oceans*, *n/a*, 2019.

Tolman, H. L., *User manual and system documentation of WAVEWATCH III, version 3.14*, Environmental Modeling Center Marine Modeling and Analysis Branch, 3.14 ed., 2009.

Tremblay, L. B., and L. A. Mysak, Modeling sea ice as a granular material, including the dilatancy effect, *Journal of Physical Oceanography*, *27*, 2342–2360, 1997.

Tsamados, M., D. L. Feltham, and A. V. Wilchinsky, Impact of a new anisotropic rheology on simulations of Arctic sea ice, *Journal of Geophysical Research: Oceans*, *118*, 91–107, 2013.

Urrego-Blanco, J., and J. Sheng, Formation and distribution of sea ice in the Gulf of St. Lawrence: A process-oriented study using a coupled ocean-ice model, *Journal of Geophysical Research: Oceans*, *119*, 7099–7122, 2014.

Uzuner, M. S., and J. F. Kennedy, Theoretical model of river ice jams, *Journal of the Hydraulics Division*, *102*, 1976.

Vancoppenolle, M., T. Fichefet, H. Goosse, S. Bouillon, G. Madec, and M. A. M. Maqueda, Simulating the mass balance and salinity of Arctic and Antarctic sea ice. 1. Model description and validation, *Ocean Modelling*, *27*, 33–53, 2009.

Voermans, J., A. Babanin, J. Thomson, M. Smith, and H. Shen, Wave attenuation by sea ice turbulence, *Geophysical Research Letters*, 2019.

Wadhams, P., Attenuation of swell by sea ice, *Journal of Geophysical Research*, *78*, 3552–3563, 1973.

Wadhams, P., A mechanism for the formation of ice edge bands, *Journal of Geophysical Research: Oceans*, *88*, 2813–2818, 1983.

Wadhams, P., V. A. Squire, D. J. Goodman, A. M. Cowan, and S. C. Moore, The attenuation rates of ocean waves in the marginal ice zone, *Journal of Geophysical Research: Oceans*, *93*, 6799–6818, 1988.

Walkington, I., M. M. Maqueda, and A. Willmott, A robust and computationally efficient model of a two-dimensional coastal polynya, *Ocean Modelling*, *17*, 140–152, 2007.

Williams, J., L. B. Tremblay, R. Newton, and R. Allard, Dynamic preconditioning of the minimum september sea-ice extent, *Journal of Climate*, *29*, 5879–5891, 2016.

Williams, J., L. B. Tremblay, and J.-F. Lemieux, The effects of plastic waves on the numerical convergence of the viscous–plastic and elastic–viscous–plastic sea-ice models, *Journal of Computational Physics*, *340*, 519–533, 2017a.

Williams, T. D., L. G. Bennetts, V. A. Squire, D. Dumont, and L. Bertino, Wave–ice interactions in the marginal ice zone. Part 1: Theoretical foundations, *Ocean Modelling*, *71*, 81–91, 2013a.

Williams, T. D., L. G. Bennetts, V. A. Squire, D. Dumont, and L. Bertino, Wave–ice interactions in the marginal ice zone. Part 2: Numerical implementation and sensitivity studies along 1D transects of the ocean surface, *Ocean Modelling*, *71*, 92–101, 2013b.

Williams, T. D., P. Rampal, and S. Bouillon, Wave-ice interactions in the neXtSIM sea ice model, *The Cryosphere Discussions*, 2017b.

Wilson, B. W., Note on surface wind stress over water at low and high wind speeds, *Journal of Geophysical Research*, *65*, 3377–3382, 1960.

Xie, T., W. Perrie, H. Fang, L. Zhao, W. Yu, and Y. He, Spatial and temporal variability of sea ice deformation rates in the Arctic Ocean observed by RADARSAT-1, *Science China Earth Sciences*, pp. 1–8, 2017.

Young, I. R., and L. Verhagen, The growth of fetch limited waves in water of finite depth. part 1. total energy and peak frequency, *Coastal Engineering*, *29*, 47–78, 1996.

Zhang, J., and W. D. Hibler III, On an efficient numerical method for modeling sea ice dynamics, *Journal of Geophysical Research: Oceans*, *102*, 8691–8702, 1997.

Zhang, S., J. Sheng, and R. J. Greatbatch, A coupled ice-ocean modeling study of the northwest Atlantic Ocean, *Journal of Geophysical Research*, *109*, C04009, 2004.

Zhang, X., H. Dai, J. Zhao, and H. Yin, Sensitivity study of the wave-driven current in an arctic frazil-pancake ice zone, *Acta Oceanologica Sinica*, *39*, 123–129, 2020.